

**Measurements of the mass of the W boson
in the $W^+W^- \rightarrow q\bar{q}q\bar{q}$ channel
with the ALEPH detector**

Matthew Donald Kennedy Chalmers

Department of Physics and Astronomy
University of Glasgow

A thesis submitted for the degree of
Doctor of Philosophy

December 1999

© M. D. K. Chalmers, 1999

ProQuest Number: 13834091

All rights reserved

INFORMATION TO ALL USERS

The quality of this reproduction is dependent upon the quality of the copy submitted.

In the unlikely event that the author did not send a complete manuscript and there are missing pages, these will be noted. Also, if material had to be removed, a note will indicate the deletion.



ProQuest 13834091

Published by ProQuest LLC (2019). Copyright of the Dissertation is held by the Author.

All rights reserved.

This work is protected against unauthorized copying under Title 17, United States Code
Microform Edition © ProQuest LLC.

ProQuest LLC.
789 East Eisenhower Parkway
P.O. Box 1346
Ann Arbor, MI 48106 – 1346

GLASGOW
UNIVERSITY
LIBRARY

11756 (copy 1)

Measurements of the mass of the W boson in the $W^+W^- \rightarrow q\bar{q}q\bar{q}$ channel with the ALEPH detector

Matthew Donald Kennedy Chalmers

Submitted for the degree of Doctor of Philosophy
at the University of Glasgow
December 1999

ABSTRACT

A measurement of the mass of the W boson from $e^+e^- \rightarrow W^+W^- \rightarrow q\bar{q}q\bar{q}$ events is presented, from LEP data collected at $\sqrt{s} = 189$ GeV during 1998 with the ALEPH detector. The procedure of direct reconstruction of the W^+W^- final state invariant mass distribution is adopted, with an optimisation of the event selection and jet clustering algorithms. A two dimensional Monte Carlo reweighting technique is used to extract the W mass and a full discussion of the systematic uncertainties is given. The W mass is measured to be:

$$M_W = 80.556 \pm 0.110(\text{stat.}) \pm 0.039(\text{syst.}) \pm 0.056(\text{F.S.I.}) \pm 0.017(\text{LEP}) \text{ GeV}/c^2 .$$

A new technique for extracting the W mass using a two dimensional Kolmogorov Smirnov test is introduced. The W mass using this method is measured to be:

$$M_W^{KS} = 80.423 \pm 0.160(\text{expected stat.}) \text{ GeV}/c^2 ,$$

which is compared with that from the method of maximum likelihood. Rigorous optimisation and stability checks on the W mass estimator and its error are presented, and the result put into the context of a LEP and subsequently world average value:

$$M_W^{\text{world}} = 80.394 \pm 0.042 \text{ GeV}/c^2 .$$

The implications of this result are interpreted by comparing it with the indirect W mass measurement from the Standard Model prediction:

$$M_W^{\text{indirect}} = 80.381 \pm 0.026 \text{ GeV}/c^2 .$$

A discussion and outlook for the W mass measurement at LEP is given.

Author's Declaration

This thesis presents measurements of the mass of the W boson in the hadronic decay channel using data taken in 1998 by the ALEPH detector at a LEP centre of mass energy $\sqrt{s} = 189$ GeV . Much of this work has been undertaken within in the ALEPH WW Group at CERN, and the results in this thesis reflect the efforts of the ALEPH collaboration over many years. The author's contributions to the ALEPH W mass measurement include optimisation studies of jet finding and hadronic event selection; the implementation and optimisation of a two-dimensional fitting technique; rigorous stability checks of the result and calculation of the systematic uncertainties due to finite Monte Carlo statistics and to fragmentation. A completely new technique for measuring the W mass using a two dimensional Kolmogorov Smirnov test has been investigated, which serves as an important cross-check of the ALEPH result. In addition, the author's contributions to the ALEPH experiment include responsibility for the TPC Laser Calibration System during 1997 and 1998, periods as the TPC coordinator and regular shifts as data manager to monitor data quality.

Acknowledgements

Over the past three years many people have contributed (perhaps unknowingly) to the support of my research and to the writing of this thesis. In particular I wish to thank Jason Ward for his invaluable advice, encouragement, chapter reading and lifts to nice places. Also my thanks to other members of the Glasgow group: Peter, Jim, Pedro, Catherine, Andy and Stan, and to the members of the ALEPH WW group. I wish to thank fellow laser expert Thomas Ziegler for making many hours deep underground enjoyable.

Of the many people I have spent time with, I wish to thank Malcolm, Jim, Suzy, A.G., Ali and Bobsleigh & Co. for providing sanity during my time in Geneva. This has been complimented by the people who visited, for which I owe thanks to Slate Buzzard, Mackay, Boris, Heather (and Ben for trying). I also want to thank the owner and friends of No. 274 for their help in my many flittings.

I would like to acknowledge my parents for their belief in me while I was a young delinquent, and in particular my father for inspiring my interest in science at an early age. I would also like to thank my sisters and grandfather for their support, and the girl who proved to me that contour integrals are an essential part of a great relationship; Barbara.

December 1999

Geneva

Contents

Abstract	ii
Acknowledgements	iv
Contents	v
List of Figures	vii
List of Tables	viii
Preface	ix
Chapter 1. Introduction	1
1.1 Motivation for M_W Measurement	1
1.2 W pair production at LEP2	3
1.3 M_W Measurement at LEP2	4
Chapter 2. Theoretical Framework	6
2.1 Introduction	6
2.1.1 Symmetries in Nature	6
2.1.2 Particles and Forces	7
2.1.3 Field Theory	9
2.2 The Standard Model	12
2.2.1 The $U(1)_Q$ Group	12
2.2.2 Electroweak Theory: $SU(2)_L \otimes U(1)_Y$	13
2.2.3 The Higgs Mechanism	16

2.3	W^+W^- Cross Section	19
2.3.1	The On-Shell Cross Section	20
2.3.2	The W Width	21
2.3.3	The Off-Shell Cross Section	22
2.4	Fragmentation	25
2.5	Final State Interactions	26
2.5.1	Colour Reconnection	27
2.5.2	Bose Einstein Correlations	28
Chapter 3. Experimental Apparatus		29
3.1	Introduction	29
3.2	The LEP Experiment	29
3.2.1	Energy Measurement at LEP1	32
3.2.2	Energy Measurement at LEP2	33
3.3	The ALEPH Detector	36
3.4	Tracking	37
3.4.1	Vertex Detector	37
3.4.2	Inner Tracking Chamber	38
3.4.3	Time Projection Chamber	38
3.4.4	Track Reconstruction	43
3.5	Calorimetry	45
3.5.1	Electromagnetic Calorimeter	45
3.5.2	Hadronic Calorimeter and Muon Chambers	46
3.5.3	Luminosity Monitors	48
3.6	Data Flow and Event Reconstruction	49
3.6.1	Trigger	49
3.6.2	Data Acquisition	50
3.6.3	Energy flow	51
3.7	Event Simulation	52
3.7.1	Monte Carlo Generators	52

Chapter 4. Event Selection and Mass Reconstruction	54
4.1 Hadronic Event Selection	55
4.1.1 Optimising the Event Selection	57
4.1.2 Neural Networks	57
4.1.3 Event selection at $\sqrt{s} = 189$ GeV	60
4.2 Jet Finding	70
4.2.1 Clustering Algorithms	70
4.2.2 Optimisation	72
4.3 Kinematical Fit	76
4.4 Jet Pairing	79
4.5 Events from which to extract the W mass	80
4.5.1 Monte Carlo Events	80
4.5.2 Data Events	83
Chapter 5. W Mass Measurement	85
5.1 Mass Extraction Methods	85
5.1.1 Breit Wigner Fit	85
5.1.2 Convolution	86
5.1.3 Monte Carlo Interpolation	86
5.1.4 Monte Carlo Reweighting	87
5.2 Monte Carlo Reweighting	87
5.2.1 Statistical Improvement in 2D	90
5.2.2 Building the <i>p.d.f.</i>	91
5.3 Statistical Limitations of MC reweighting	93
5.3.1 Binning of the <i>p.d.f.</i>	94
5.4 W Mass Parameter Estimation	97
5.4.1 Expected error	97
5.4.2 Linearity of method	98
5.4.3 Results at 189 GeV	100
5.5 Stability Checks	102
5.5.1 Binning	102
5.5.2 Neural Net cut	106

5.5.3	Mass Window	107
5.6	Systematic Considerations	108
5.6.1	Finite MC Statistics	108
5.6.2	Fragmentation	109
5.6.3	Summary of systematics	118
5.7	Chapter Summary	121
Chapter 6. Kolmogorov Smirnov Test		122
6.1	KS Test Principle	122
6.1.1	One Dimensional KS Test	123
6.1.2	KS Test in Two Dimensions	124
6.2	Applying the KS test to Measure M_W	126
6.2.1	The compatibility of data and Monte Carlo	126
6.2.2	Estimating M_W	128
6.2.3	Stability Checks	134
6.2.4	Comparison with Likelihood Method	134
6.3	Chapter Summary	137
Chapter 7. Combination of W Mass Results		138
7.1	ALEPH W Mass Measurement	138
7.2	LEP W Mass Combination	139
7.3	Tevatron Collider W mass Results	140
7.4	Standard Model Constraints	142
Chapter 8. Summary and Conclusions		145
Appendix A. Global event shape variables		148
Appendix B. 4C Fit + Rescaling		150
References		153

List of Figures

1.1	Radiative loop corrections to the W mass.	2
1.2	The LEP2 Programme.	3
1.3	The CC03 diagrams.	4
1.4	The three W^+W^- decay channels.	4
2.1	The force between two electrons.	9
2.2	Higher order diagrams.	10
2.3	The W^+W^- cross section.	24
3.1	Location and layout of the LEP collider.	30
3.2	Schematic of LEP injection system.	31
3.3	Extrapolation for LEP2 beam energy measurement.	34
3.4	Schematic of LEP Spectrometer principle.	34
3.5	The ALEPH Detector.	36
3.6	The ALEPH Vertex Detector.	38
3.7	The ALEPH Inner Tracking Chamber.	39
3.8	The ALEPH Time Projection Chamber.	40
3.9	Side view of a TPC sector.	40
3.10	TPC laser system.	42
3.11	The ALEPH central tracking region.	44
3.12	ECAL layer.	45
3.13	HCAL layout.	47
3.14	Data acquisition.	50
4.1	Schematic of 4-jet event.	55

4.2	ALEPH event display of 4-jet event.	56
4.3	Efficiency of hadronic event selection algorithms.	58
4.4	Efficiency mass dependence as a function of selection cut.	59
4.5	Neural Network variables 1-6.	62
4.6	Neural Network variables 7-12.	63
4.7	Neural Network variables 13-14.	64
4.8	Correlations between Neural Network variables 1-9.	65
4.9	Correlations between Neural Network variables 10-14.	66
4.10	Data/MC correlations in variables 1-9.	67
4.11	Data/MC correlations in variables 10-14.	68
4.12	Neural Network output.	68
4.13	Efficiency versus purity for NN14.	69
4.14	Mass shifts from using different jet finders.	74
4.15	Mass resolutions when using different jet finders.	75
4.16	Average corrections applied to measured jet momenta.	77
4.17	The improvement in mass resolution with kinematical fitting.	78
4.18	Correct and incorrect di-jet pairs.	80
4.19	Scatter plots of (m_1, m_2) in Monte Carlo.	82
4.20	Scatter plot of (m_1, m_2) in data.	83
4.21	Distributions from which to measure the W mass.	84
5.1	Check of the reweighting technique.	88
5.2	The effect of reweighting the invariant mass distribution.	89
5.3	W^+W^- Cross Section parameterisation.	92
5.4	Bias caused by reweighting too far from reference mass.	94
5.5	Effect of binning on the linearity.	95
5.6	Binning for $\sqrt{s} = 183$ GeV result.	95
5.7	Binning used for measurement at $\sqrt{s} = 189$ GeV.	96
5.8	The expected error on the W mass.	98
5.9	Linearity of W mass measurement.	99
5.10	Invariant mass distribution of fitted W mass.	100
5.11	Likelihood curve for data fit.	101

5.12	Confidence interval of mass measurement.	103
5.13	Stability of the expected error with binning.	104
5.14	Stability of the linearity with binning.	105
5.15	Stability of the measurement with NN cut.	106
5.16	Estimating the systematic from the finite MC reference.	109
5.17	Fragmentation studies (variables 1-6).	111
5.18	Fragmentation studies (variables 7-12).	112
5.19	Fragmentation studies (variables 13-14).	113
5.20	Fragmentation studies (variable 1-9 correlations).	115
5.21	Fragmentation studies (variable 10-14 correlations).	116
5.22	Estimating the systematic error from fragmentation.	117
6.1	The 1D Kolmogorov Smirnov Test.	123
6.2	The 2D Kolmogorov Smirnov Test.	125
6.3	Distribution of the KS test statistic D .	127
6.4	The convergence of the KS test statistic.	129
6.5	The sensitivity of the KS test statistic.	131
6.6	The expected error using the KS test.	132
6.7	Estimating the error from first principles.	133
6.8	The effect of using an accelerated KS test.	134
6.9	Dependence of D on the W mass parameter.	135
6.10	Linearity of the KS test method.	135
6.11	Comparison with maximum likelihood method.	136
7.1	The LEP $M_W^{4q} - M_W^{non-4q}$ difference.	141
7.2	World average W mass measurement.	143
7.3	Direct and indirect M_W and m_t measurements.	144

List of Tables

1.1	Summary of $p\bar{p}$ collider measurements.	2
2.1	The Standard Model.	8
2.2	Fermion quantum numbers.	14
2.3	Number of $4f$ diagrams.	22
3.1	Momentum resolution of the ALEPH tracking detectors.	45
3.2	The ALEPH trigger.	49
3.3	Monte Carlo generators.	53
4.1	Neural Net input variables.	61
4.2	Definitions of clustering algorithms.	71
4.3	Jet finding schemes.	71
4.4	Selected W^+W^- events.	81
4.5	Selected non W^+W^- events.	81
4.6	Expected number of events.	82
4.7	Selected data events.	83
5.1	Stability of results to the mass window.	107
5.2	JETSET fragmentation parameters.	110
5.3	Summary of the correlated and uncorrelated systematic errors on M_W .	120
6.1	Mass coordinates driving KS test convergence.	130
7.1	Summary of ALEPH hadronic W mass measurements.	138
7.2	Preliminary hadronic W mass measurements at LEP .	140

Preface

This thesis is structured in the following way: Motivation for the W mass measurement is given and the available methods at LEP are discussed in Chapter 1. Chapter 2 gives an overview of the Standard Model and an interpretation of the W boson mass using Electroweak theory. Chapter 3 is devoted to a description of the experimental apparatus used, namely the LEP collider and the ALEPH detector. Chapter 4 explains the analysis used to reconstruct the invariant mass distribution from which to extract the W mass. Studies of the W mass extraction technique are given in Chapter 5 and the results which were obtained at $\sqrt{s} = 189$ GeV. In Chapter 6 a completely new measurement technique, the 2D Kolmogorov Smirnov test, is introduced and compared with the previous one. In Chapter 7 the result is put into the context of a world average W mass measurement and a summary and conclusion are presented in Chapter 8.

Chapter 1

Introduction

One of the most important questions in particle physics concerns the origin of mass. At the subatomic level it appears that the fundamental constituents of the universe have distinctly different masses, which has dramatic consequences for the world we live in. The W and Z vector bosons, postulated to be responsible for the weak nuclear force, were first discovered at CERN in 1983 at the Super Proton Synchrotron (SPS) experiments, UA1 [1] and UA2 [2]. Since then it has been the goal of several experiments worldwide to measure their masses, M_W and M_Z , as accurately as possible, thus providing a deeper understanding of the basic laws of nature.

1.1 Motivation for M_W Measurement

Precision measurements of M_W and M_Z are of fundamental physical importance, since the relation between them is predicted by the theory describing the interactions of elementary particles, the Standard Model (SM). The W mass can be determined indirectly from the precisely known Z mass and fermi constant G_μ , using the SM prediction for muon decay [3]:

$$M_W^2 = \frac{\pi\alpha}{\sqrt{2}G_\mu \sin^2 \theta_W} \frac{1}{1 - \Delta r}, \quad (1.1)$$

where

$$\sin^2 \theta_W = 1 - \frac{M_W^2}{M_Z^2}. \quad (1.2)$$

At tree level (lowest order calculation) the factor $\Delta r = 0$. When loop corrections are included Δr depends on the masses of the top quark m_t and Higgs boson M_H .

Such corrections are illustrated in Figure 1.1, which for the W mass infer a quadratic and logarithmic dependence on m_t and M_H respectively.

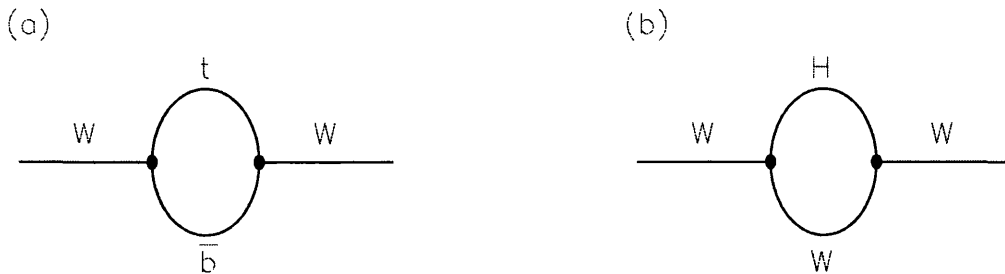


Figure 1.1: Radiative loop corrections to the W mass which lead to: (a) a quadratic dependence on m_t and (b) a logarithmic dependence on M_H .

Global electroweak fits to the data through Equation 1.1 can thus determine M_W , M_H and m_t simultaneously. With data from LEP1 and SLD the indirect W mass is [4]

$$M_W^{indirect} = 80.381 \pm 0.026 \text{ GeV}/c^2 .$$

The direct measurement of M_W thus becomes important if its error is comparable, or smaller than, the indirect measurement. Direct measurements from $p\bar{p}$ experiments at CDF [5], D0 [6] (Tevatron, Fermilab) and the UA2 experiment [7] are summarised in Table 1.1.

	M_W (GeV/c^2)
UA2	80.360 ± 0.370
CDF	80.433 ± 0.089
D0	80.474 ± 0.093
Average	80.448 ± 0.062

Table 1.1: Preliminary measurements of M_W at $p\bar{p}$ colliders [8].

In particular, a precise measurement of M_W can be used together with the direct determination of m_t at the Tevatron [9] to place mass constraints on the Higgs boson within the framework of the SM. Additionally, the measurement can be used to constrain the existence of physics beyond the SM, as a disagreement between M_W^{direct} and M_W^{indirect} could indicate that the W boson couples to other particles.

1.2 W pair production at LEP2

Since 1996 it has been possible to make a direct measurement of the W mass at the Large Electron Positron collider (LEP). LEP is a good environment to make a precise measurement as the centre of mass energy is well known and all decay modes of the W boson can be studied. A schematic illustrating the LEP2 programme is shown in Figure 1.2 in terms of the W^+W^- pair production cross section.

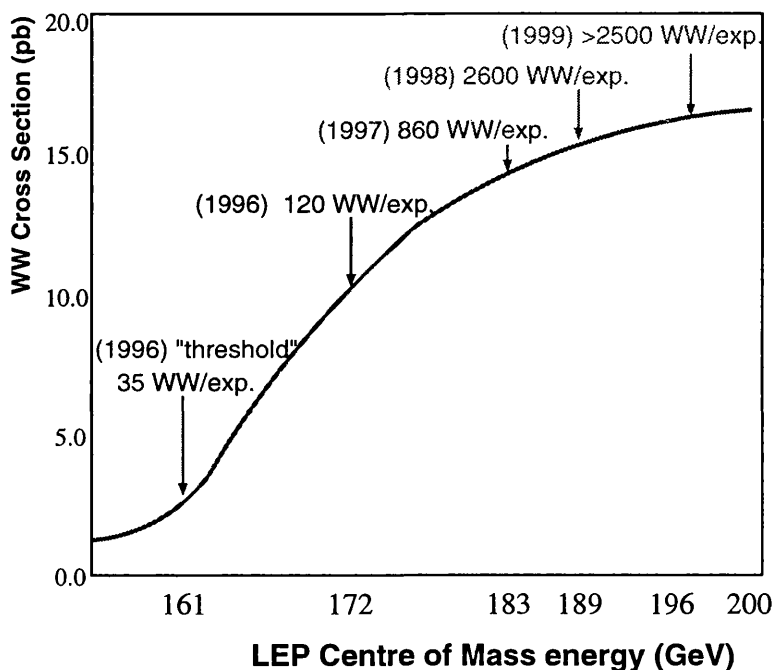


Figure 1.2: The LEP2 W^+W^- lineshape scan. Since 1996 the LEP centre of mass energy has gradually increased, producing more W^+W^- pairs. The approximate number of W^+W^- pairs collected by each of the four LEP experiments is indicated.

W^+W^- pairs are produced at LEP2 through the process $e^+e^- \rightarrow W^+W^-$ at energies above production threshold ($\sim 2M_W$) which is dominated by the CC03 ('3 charged current') diagrams shown in Figure 1.3. The cross sections for the *s-channel* (virtual Z, γ exchange) processes are proportional to β_W^3 , where β_W is the boost of the W , while the *t-channel* (ν -exchange) is proportional to β_W making it the dominant diagram at energies close to threshold.

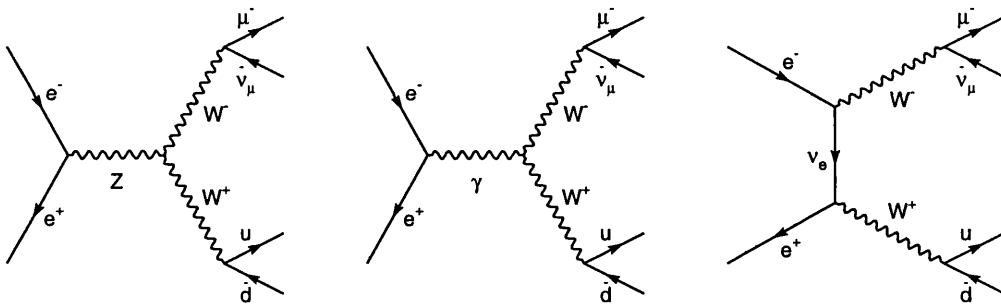


Figure 1.3: The CC03 diagrams; the main processes by which W^+W^- pairs are produced at LEP2. The example shown is for a W^+W^- ‘semi-leptonic’ decay, where one W has decayed into leptons and the other into quarks.

1.3 M_W Measurement at LEP2

The W^+W^- cross section is particularly sensitive to the W mass around the threshold region, which makes possible a measurement of the W mass from the cross-section within the framework of the SM. Using data collected by the four LEP experiments at $\sqrt{s} = 161$ GeV the W mass is measured to be [3],

$$M_W^{cross-section} = 80.400 \pm 0.220 \text{ GeV}/c^2.$$

At LEP energies above W^+W^- production threshold the most efficient method of measuring the mass of the W boson is by the direct reconstruction of its decay products in the final state. The W^+W^- decay final states of importance for the W mass measurement along with their branching ratios are summarised in Figure 1.4.

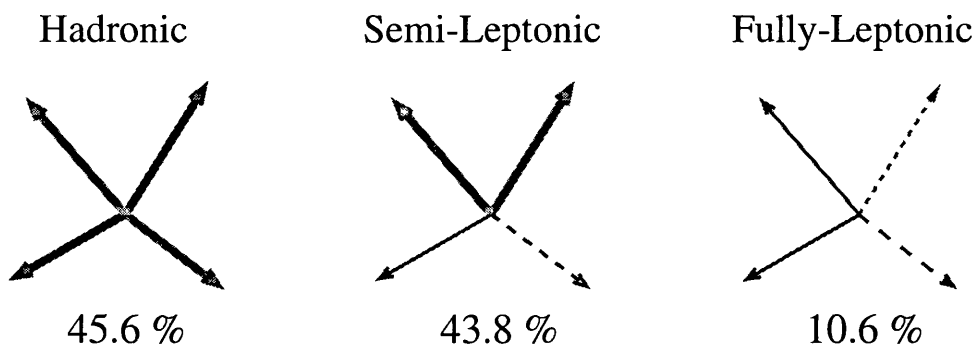


Figure 1.4: The three channels to which a W^+W^- pair can decay. Thick arrows represent hadronic jets, thin arrows represent leptons and broken arrows represent undetected neutrinos. Their branching ratios derive from the fact that $\text{B.R.}(W \rightarrow q\bar{q}) = 68.8\%$.

In terms of merit for extracting the W mass, the semi-leptonic channel is particularly valuable as there is a clear signature of two hadronic jets, an energetic lepton and missing energy from the neutrino. The non- W^+W^- background is therefore minimal for the case of the $e\nu q\bar{q}$ and $\mu\nu q\bar{q}$ sub-channels, although slightly higher for the $\tau\nu q\bar{q}$ final state. The fully leptonic channel suffers from a low branching ratio, but moreover from the fact that kinematic event reconstruction is difficult because two neutrinos escape detection. A measurement of M_W in this channel has however been made, which uses the end-point of the lepton energy distribution [10].

The measurement described in this thesis is made from hadronic W^+W^- events, where each W has decayed into a $q\bar{q}$ pair. The main disadvantage in the hadronic channel is the problem of associating the final four-jets to their correct parent W 's and the presence of a relatively high non- W^+W^- background. In addition, the final state of four quarks develops in a small space-time region, leading to interconnection phenomena which may affect the reconstructed W mass.

The statistical power of the direct reconstruction approach has been estimated as [11] (pp. 150):

$$\Delta M_W \approx \frac{\Gamma_W}{\sqrt{N}} \approx 50\text{MeV} \sqrt{\frac{100\text{pb}^{-1}}{\mathcal{L}}}, \quad (1.3)$$

where Γ_W is the width of the W boson and \mathcal{L} the data luminosity collected by the detector. By the end of LEP2 it was foreseen that the combined luminosity of all four LEP experiments would be more than 500 pb^{-1} which corresponds to a statistical precision on M_W of $\sim 30 \text{ MeV}/c^2$, comparable to the uncertainty on the indirect measurement. In fact LEP has performed better than expected over the period 1996-1999 and a total integrated luminosity of 700 pb^{-1} may be achievable with data taken in 2000 [12].

Chapter 2

Theoretical Framework

2.1 Introduction

Particle physics is the study of the fundamental constituents of matter and their interactions. This chapter gives an introduction to the current picture of particle physics, the Standard Model (SM), beginning with the subtle concept of symmetry on which it is based and going on to describe its structure in three sectors: fermionic, gauge and scalar, which are linked by a generalisation of quantum mechanics known as Quantum Field Theory. The theory of electroweak interactions will then be described in more detail and used along with the Higgs mechanism to give an interpretation of the W boson. Finally the theoretical aspects of particular relevance to the W mass measurement described in this thesis will be given. Unless otherwise stated, references for this section are in [13-18].

2.1.1 Symmetries in Nature

One of the most elegant features in physics is the existence of symmetries in nature, which provide insight and simplicity to a complex physical system. Symmetry is quite evident in classical physics, for example the motion of the planets in the solar system, but it is at the sub-microscopic level where there is greatest scope for symmetry to be exploited, owing to the fact that nature has a finite set of building blocks (take for example the structure of crystals). The existence of symmetries plays a crucial role in the understanding of the most fundamental physical system, elementary particle physics, as the complexities of quantum mechanics can be simplified greatly.

Symmetries in nature yield conservation laws and conversely, conservation laws reveal an underlying symmetry (Noether's theorem). For example, if a system is invariant under a translation in space then momentum is conserved. More formally, it is said that a symmetry S exists when the Hamiltonian¹ of the physical system under study is invariant under the transformation given by S , i.e. $SHS^\dagger = H$.

The properties of the set of these symmetry operations are precisely the defining properties of a mathematical *group*, which is the formalism used to build theories in particle physics. The group structure depends on the complexity of the symmetry, which in particle physics is based on the principle of gauge invariance. This is the property of a theory where its Lagrangian² is invariant under a gauge (or phase) transformation. Each generator of the gauge group introduces a conserved quantity and in particular a massless gauge boson field. The Lagrangian may possess 'hidden' symmetries also, and it is the breaking of such a symmetry that is responsible for the mass of the W boson.

2.1.2 Particles and Forces

It seems that the universe is composed of two types of particles, fermions and bosons, distinguished by their spin angular momentum (which is a direct consequence of symmetry in their wavefunctions). They interact via the four known forces in nature, electromagnetism, gravity and the strong and weak nuclear forces. Although gravity is the most apparent in the world around us, it is insignificant for elementary particles due to their small masses ($\sim 10^{-40}$ times weaker than the strong force) and is not included in the SM.

The fermion or matter content is further divided into quarks and leptons according to their interactions and each fall naturally into three generations. This 'modern day periodic table' is shown in Table 2.1. Each quark and lepton has an anti-particle partner with opposite electric charge and quantum numbers and each flavour of quark comes in three colour charges. Particles belonging to the 2nd and 3rd generations only exist at high energies. The particle masses increase from the

¹The Hamiltonian is a function expressing the energy of a system in terms of its momentum and position coordinates and is used extensively in the formalism of quantum mechanics.

²The Lagrangian approach is an alternative formalism which describes a physical system in terms of its kinetic T and potential V energy: $\mathcal{L} = T - V$.

	1st Generation	2nd Generation	3rd Generation	Electric Charge
Quarks	d (down)	s (strange)	b (bottom)	$-1/3$
	u (up)	c (charm)	t (top)	$+2/3$
Leptons	e (electron)	μ (muon)	τ (tau)	-1
	ν_e (e -neutrino)	ν_μ (μ -neutrino)	ν_τ (τ -neutrino)	0

Table 2.1: Fermionic sector of the Standard Model.

1st to the 3rd generation and ‘everyday’ matter is built from the lightest generation only. The generation structure is not explained by the SM, neither are the particle masses themselves.

The forces between these particles are mediated by integral spin gauge bosons: the photon for the electromagnetic force, the massive W^\pm and Z for the weak force and 8 massless gluons for the strong force. The range of these forces are inversely proportional to the mass of the corresponding boson³, which explains the infinite range of electromagnetism and the very short range of the weak interaction. The strong force, however, has a very short range but massless force carriers. This is because the gluons themselves carry colour and will be explained in more detail later.

The strength of the interactions are described by the magnitude of the corresponding coupling constant α , relative to the strong force. Only particles with colour experience the strong force, i.e. the quarks and gluons. The electromagnetic force is felt by all particles with electric charge (while the photon is neutral) and the weak force acts on all fermions and bosons with the exception of the gluon.

³More explicitly, their range is given by the Compton wavelength of the propagator, limited by the Uncertainty Principle.

2.1.3 Field Theory

The mathematical framework which marries the concepts of fundamental particles and forces and enables the calculation of physical observables is known as Quantum Field Theory (QFT). The original and best example is the $U(1)_{\text{EM}}$ gauge theory⁴ of quantum electrodynamics (QED) [19]. This is the result of incorporating Maxwell's electromagnetic picture into quantum mechanics and is a useful example with which to describe the main features of quantum field theory.

QFT replaces the problem of 'action at a distance' by describing all the forces in nature as the result of particle exchange. In QED, the repulsion between two electrons is described by the diagram in Figure 2.1, the exchange of a *virtual* photon. This process violates energy conservation, but in quantum mechanics this is permitted for a period consistent with the Uncertainty Principle ($\Delta t \leq \hbar/\Delta E$).

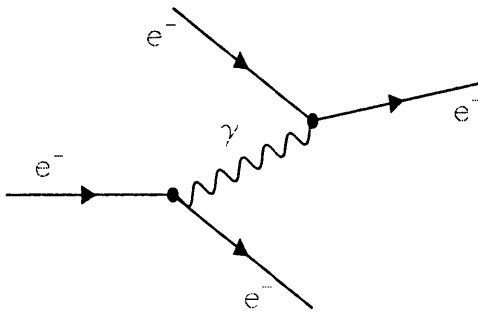


Figure 2.1: In QED electrons repel by the exchange of a virtual photon.

These 'Feynman diagrams', named after their inventor, are pictorial representations of mathematical expressions for the Lorentz invariant matrix element, or amplitude, \mathcal{M} for a particular process. Straight lines represent spin- $\frac{1}{2}$ fermions and the helices spin-1 boson propagators. They connect at vertices where a factor $\sqrt{\alpha}$ enters, describing the strength of the interaction, and at which energy and momentum are conserved. The matrix element for a diagram such as Figure 2.1 has the form

$$\mathcal{M} \sim \mathcal{M}_i G \mathcal{M}_f, \quad (2.1)$$

⁴The $U(1)$ symmetry group are global rotations of the field by the phase $e^{i\theta(x)}$, which through Noether's theorem implies the conservation of electric charge Q . For this reason, it will be referred to as $U(1)_Q$ throughout this chapter.

where \mathcal{M}_i and \mathcal{M}_f are the matrix elements at the initial and final state vertices and G represents the boson propagator. In QFT this has the form

$$G \propto \frac{1}{q^2 - m^2}, \quad (2.2)$$

where q and m are the four momenta and mass of the exchanged boson. The value of q^2 in such a process is negative, therefore implying a negative mass value. A particle which has $E^2 - p^2 \neq m^2$ is said to be ‘virtual’ or ‘off-shell’, in contrast to a free particle which has $E^2 - p^2 = m^2$ and is said to be ‘real’ or ‘on-shell’. The differential cross section for a given process (diagram) is

$$\frac{d\sigma}{dx} \propto |\mathcal{M}|^2 \rho(x), \quad (2.3)$$

where x is a kinematic variable and $\rho(x)$ is the phase space density. The Feynman diagram formalism is convenient because the total cross section for this process is obtained by considering all the diagrams in which vertices are connected in all possible ways and squaring the sum of these amplitudes. This results mathematically as a power series in terms of the coupling constant α . For the case of QED (Figure 2.1) each ascending term in this series should contribute a smaller correction to the e^-e^- Coulomb repulsion, since $\alpha_{EM} < 1$. Two such ‘radiative corrections’ are shown in Figure 2.2.

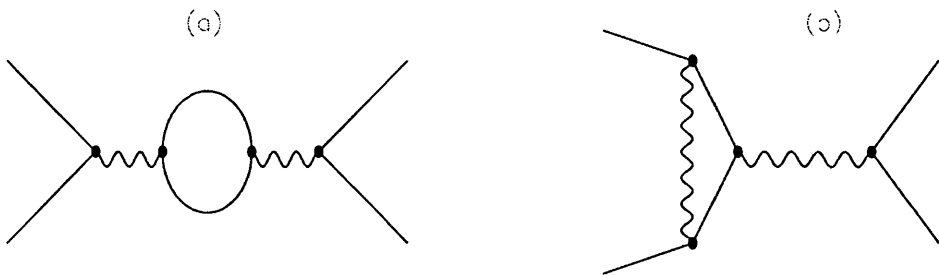


Figure 2.2: Some higher order contributions to the Coulomb interaction: (a) represents the polarisation of the vacuum and (b) the anomalous magnetic moment of the electron.

The problem with diagrams containing such radiative terms is that their corresponding integral is divergent, rendering perturbation theory unphysical. These infinities were overcome by the technique of renormalisation. Firstly the integrals are regularised with some factor which involves a *cutoff* mass M , assumed to be very

large and taken to infinity at the end of the calculation. The integral then separates into a finite part independent of M , and a term which diverges as $M \rightarrow \infty$. At the end of the calculation this latter term infers an additive term to the masses and coupling constant, which means that the troublesome infinities can be absorbed into redefinitions of the coupling constant and particle masses. The fact that these additive factors are infinite as $M \rightarrow \infty$ does not matter, since it is only the physical values that are experimentally measured (nature sums all diagrams automatically), thus these renormalised parameters are the correct ones to compare with experiments. The remaining finite part of the integral leads to an energy dependence in the particle masses and coupling constant.

The success of QED, along with the work of 't Hooft which showed that in fact *all* gauge theories are renormalisable [20], motivated similar theories for the strong and weak interactions. The larger symmetry group $SU(3)$ was proposed to describe the strong interaction. The corresponding gauge theory is known as Quantum Chromodynamics (QCD) based on the gauge symmetry of strong interactions, namely the colour transformations which leave its Hamiltonian invariant. The $SU(3)$ group has eight generators and thus QCD has eight *coloured* gauge bosons, called gluons. The diagrams of QCD are similar to QED with the electron lines replaced with quarks and the photon propagator by gluons. However, calculations in QCD are much more complicated due to the fact that gluons themselves carry colour and the expansion to higher orders diverges, since at this scale $\alpha_s > 1$. Perturbation theory can only be applied to the simplest bare quark-gluon processes not directly observed, and in practice phenomenological QCD models are heavily relied upon.

A description of the weak interaction was first proposed by Fermi [21], however despite its success in explaining radioactive β -decay it could not incorporate the observation that the weak force couples only to left-handed fermions (maximally parity violating) [22]. To fully incorporate the phenomenology of the weak interaction into a renormalisable gauge theory, the electroweak (EW) theory was built. This unifies the weak and electromagnetic interactions into a symmetry group which contains as a subset $U(1)_Q$ and is described in more detail in the next section.

2.2 The Standard Model

The Standard Model (SM) [23, 24, 25] is a quantum field theory based on the total gauge symmetry of the fundamental $SU(2)_L \otimes U(1)_Y$ electroweak and $SU(3)_C$ strong interactions in particle physics,

$$SU(3)_C \otimes SU(2)_L \otimes U(1)_Y.$$

By demanding local gauge invariance of the Standard Model Lagrangian, the spin-1 fields mediating the interactions are massless. This makes the theory unphysical as the bosons *and* fermions are then massless. The mechanism that generates masses in the SM is based on the spontaneous symmetry breaking (SSB) of the electroweak $SU(2)_L \otimes U(1)_Y$ symmetry, which causes the weak and electromagnetic force to decouple, while preserving local gauge invariance [26]. A consequence of SSB is the prediction of a massive scalar (spin-0) particle known as the Higgs boson which has not yet been discovered experimentally. The combination of the electroweak theory and the Higgs mechanism is referred to as the electroweak Standard Model, which to date along with QCD describes all observed phenomenon in particle physics. Attempts at unifying EW theory and QCD into a single gauge theory (Grand Unified Theory, or GUT) have so far proved to be unsuccessful.

To illustrate how the fundamental principle of gauge invariance leads to the prediction of physical fields, an example using the electromagnetic ($U(1)_Q$) interaction is given in the following section. This will be used as the basis for interpreting the W boson in Section 2.2.2.

2.2.1 The $U(1)_Q$ Group

Before writing down the EW Lagrangian, consider the case for the $U(1)_Q$ group. The Lagrangian for a free Dirac (spin- $\frac{1}{2}$) particle ψ ,

$$\mathcal{L} = \bar{\psi}(i\gamma^\mu\partial_\mu - m)\psi, \quad (2.4)$$

is not invariant under local phase transformation $\psi \rightarrow e^{i\theta(x)}\psi$. Therefore introduce the gauge-covariant derivative:

$$D_\mu = \partial_\mu - ieA_\mu, \quad (2.5)$$

and replace ∂_μ by D_μ in Equation 2.4 to give the gauge invariant Lagrangian

$$\mathcal{L} = \bar{\psi}(i\gamma^\mu\partial_\mu - m)\psi + e\bar{\psi}\gamma^\mu\psi A_\mu. \quad (2.6)$$

By demanding local gauge invariance the vector field A_μ has been introduced, which couples to the Dirac particle with strength e . Interpreting this as the photon field⁵ and therefore including in the Lagrangian its kinetic energy term,

$$-\frac{1}{4}F_{\mu\nu}F^{\mu\nu}, \quad (2.7)$$

where the field strength tensor $F_{\mu\nu} = \partial_\mu A_\nu - \partial_\nu A_\mu$, the Lagrangian of QED is arrived at:

$$\mathcal{L}_{QED} = \underbrace{\bar{\psi}(i\gamma^\mu\partial_\mu - m)\psi}_{E_k \text{ and mass of } \psi} + \underbrace{e\bar{\psi}\gamma^\mu\psi A_\mu}_{\text{Interaction}} - \underbrace{\frac{1}{4}F_{\mu\nu}F^{\mu\nu}}_{E_k \text{ of } A_\mu}. \quad (2.8)$$

The addition of a mass term $\frac{1}{2}m^2 A_\mu A^\mu$ would cause \mathcal{L}_{QED} to change under a local gauge transformation and is therefore not allowed. This ensures that the gauge particle, the photon, is massless.

In short, by imposing local gauge invariance of the free electron Lagrangian, the interacting field theory of QED is produced. In the Standard Model all of the fundamental interactions are produced in this way.

2.2.2 Electroweak Theory: $SU(2)_L \otimes U(1)_Y$

The SM electroweak symmetry $SU(2)_L \otimes U(1)_Y$ is required to be a local symmetry of the electroweak Lagrangian. $SU(2)_L$ is the weak *isospin* group which acts only on left-handed fermions and $U(1)_Y$ is the weak *hypercharge* group. Within the electroweak formalism there is an electromagnetic and weak unification since $U(1)_Q$ appears as a subset of the total electroweak group:

$$U(1)_Q \subset SU(2)_L \otimes U(1)_Y. \quad (2.9)$$

The quark *mass* eigenstates $\{d, s, b\}$ are not the same as the quark *weak* eigenstates $\{d', b', s'\}$ and they mix via the Cabibbo-Kobayashi-Maskawa (CKM) matrix.

⁵In classical electrodynamics the equation of motion for a charged particle moving through an electromagnetic field is obtained by the transformation, $p_\mu \rightarrow p_\mu - ieA_\mu$.

In this way the weak interaction is sometimes described as QFD, *Quantum Flavour Dynamics*, as it transforms quarks from different generations. For this reason it is clearer to illustrate electroweak theory for the case of the leptons than for the quarks.

The $SU(2)_L \otimes U(1)_Y$ group has four generators, three of which are the $SU(2)_L$ generators, $T_i = \frac{\sigma_i}{2}$ with $i = 1, 2, 3$, and the fourth the $U(1)_Y$ generator, $\frac{Y}{2}$, where σ are the Pauli spin matrices. Left handed fermions transform as doublets under $SU(2)_L$, which for the case of the leptons is

$$f_L \rightarrow e^{iT\theta} f_L; \quad f_L = \begin{pmatrix} \nu_L \\ e_L \end{pmatrix}, \begin{pmatrix} u_L \\ d_L \end{pmatrix}, \dots,$$

whereas the right-handed fermions transform as singlets,

$$f_R \rightarrow f_R; \quad f_R = e_R, u_R, d_R, \dots$$

The quark and lepton quantum numbers for the first generation are shown in Table 2.2. Notice the absence of the right-handed neutrino, which is not observed in nature. The relationship between them is incorporated into the SM via the electric charge matrix Q ,

$$Q = T_3 + \frac{Y}{2}. \quad (2.10)$$

	T	T_3	Q	Y
Leptons				
ν_L	$\frac{1}{2}$	$\frac{1}{2}$	0	-1
e_L	$\frac{1}{2}$	$-\frac{1}{2}$	-1	-1
e_R	0	0	1	-2
Quarks				
u_L	$\frac{1}{2}$	$\frac{1}{2}$	$\frac{2}{3}$	$\frac{1}{3}$
d_L	$\frac{1}{2}$	$-\frac{1}{2}$	$-\frac{1}{3}$	$\frac{1}{3}$
u_R	0	0	$\frac{2}{3}$	$\frac{4}{3}$
d_R	0	0	$-\frac{1}{3}$	$-\frac{2}{3}$

Table 2.2: Lepton and quark quantum numbers, shown for the first generation only.

The number of associated gauge bosons, being equal to the number of generators, is four: \mathbf{W}_μ^i , $i = 1, 2, 3$ (the weak bosons of $SU(2)_L$) and B_μ (the hypercharge boson of $U(1)_Y$). The discussion of $U(1)_Q$ (Section 2.2.1) becomes more general for

the EW case because \mathcal{L}_{QED} describes the electron field where the generator (the charge operator Q , Equation 2.10) is equal to 1. To incorporate weak processes, the interaction term in Equation 2.8 has to be replaced by the fundamental structure:

$$-i \left[g \mathbf{T} \cdot \mathbf{W}^\mu + g' \frac{Y}{2} B^\mu \right], \quad (2.11)$$

where g and g' represent the coupling strengths to $SU(2)_L$ and $U(1)_Y$, respectively.

The electroweak Lagrangian is built from three parts:

$$\mathcal{L}_{EW} = \mathcal{L}_f + \mathcal{L}_G + \mathcal{L}_{Higgs}. \quad (2.12)$$

The first term, \mathcal{L}_f , represents the lepton and quark kinetic energies and interactions with the \mathbf{W}^μ and B_μ fields. It arises by imposing $SU(2)_L \otimes U(1)_Y$ invariance which, for a generic fermion field f , requires the covariant derivative

$$D_\mu = \partial_\mu + ig \mathbf{T} \cdot \mathbf{W}_\mu + ig' \frac{Y}{2} B_\mu \quad (2.13)$$

(compare with Equation 2.5). The gauge invariant electroweak interactions are generated from the term

$$\mathcal{L}_f \equiv \bar{f} \gamma^\mu D_\mu f. \quad (2.14)$$

To be more specific: knowing that right-handed fermions do not couple to the \mathbf{W}^μ fields; summing over the weak isospin (lepton) doublets and inserting the actual hypercharge values from Table 2.2, this becomes

$$\mathcal{L}_f = i \sum_{f=e,\mu,\tau} f_L \left(\partial_\mu - ig \mathbf{T} \cdot \mathbf{W}_\mu + ig' \frac{1}{2} B_\mu \right) \gamma^\mu \bar{f}_L + i \sum_{f=e,\mu,\tau} f_R \left(\partial_\mu + ig' B_\mu \right) \gamma^\mu \bar{f}_R. \quad (2.15)$$

The second term of the EW Lagrangian (Equation 2.12) represents the kinetic energies and self-interactions of the \mathbf{W}^μ and B_μ ,

$$\mathcal{L}_G = -\frac{1}{4} \mathbf{W}_{\mu\nu} \cdot \mathbf{W}^{\mu\nu} - \frac{1}{4} B_{\mu\nu} B^{\mu\nu}. \quad (2.16)$$

Combined with \mathcal{L}_f , the $SU(2)_L \otimes U(1)_Y$ Lagrangian describes the interactions of fermions with the electroweak fields, but it contains no mass terms. Preservation of gauge invariance forbids the insertion of terms like $m^2 W_\mu^i W_\mu^i$ for the gauge fields and since the left and right handed fermions transform differently, their masses cannot be included either. This phenomenological ‘disaster’ is cured by the scalar sector of the SM (the Higgs Mechanism), which breaks the $SU(2)_L \otimes U(1)_Y$ symmetry and gives rise to the gauge boson masses, while retaining local gauge invariance of the electroweak Lagrangian.

2.2.3 The Higgs Mechanism

To accommodate massive gauge bosons by the Higgs mechanism [26], a complex weak isospin scalar ϕ is introduced, which must belong to $SU(2)_L \otimes U(1)_Y$ multiplets:

$$\phi = \begin{pmatrix} \phi^+ \\ \phi^0 \end{pmatrix} = \frac{1}{\sqrt{2}} \begin{pmatrix} \phi_1 + i\phi_2 \\ \phi_3 + i\phi_4 \end{pmatrix},$$

along with the scalar potential $V(\phi)$. The contribution to the electroweak Lagrangian is then

$$\mathcal{L}_{Higgs} = (D_\mu \phi)^\dagger (D^\mu \phi) - V(\phi), \quad (2.17)$$

where D_μ is given in Equation 2.13. Subject to the constraints of $U(1)_Q$ gauge invariance, the simplest possible form of the Higgs potential is

$$V(\phi) = \mu^2 \phi^\dagger \phi + \lambda (\phi^\dagger \phi)^2, \quad (2.18)$$

which has a 4-sphere⁶ of global minima at $|\phi|^2 = -\mu^2/2\lambda = v^2$, taking $\phi_3 = v$, $\phi_{1,2,4} = 0$. The arbitrary choice of a specific minimum gives ϕ a non-zero vacuum expectation value, $\phi_0 = v$ and the subsequent absence of apparent symmetry in the ground state means the $SU(2)_L \otimes U(1)_Y$ symmetry has been ‘spontaneously broken’. This gives rise to massless scalars (the Goldstone theorem).

Choosing the vacuum expectation value at: $\phi_3 = v$, $\phi_{1,2,4} = 0$ with $T = \frac{1}{2}$, $T^3 = -\frac{1}{2}$ and $Y = 1$ breaks both $SU(2)_L$ and $U(1)_Y$ gauge symmetries but leaves the $U(1)_Q$ symmetry unbroken since $Q = 0$. This ensures the photon is massless, while generating masses for the gauge bosons. The resulting particle spectrum becomes apparent upon expansion around ϕ_0 :

$$\phi = \frac{1}{\sqrt{2}} e^{i\xi \cdot \mathbf{T}/v} \begin{pmatrix} 0 \\ v + H \end{pmatrix}, \quad (2.19)$$

where ξ and H are a parameterisation of the vacuum fluctuations. The components of ξ are called Goldstone bosons, one for each generator of the spontaneously broken gauge group. These are not physical particles, but scalar degrees of freedom which are absorbed into longitudinal polarisation states of massive gauge bosons. H is a massive neutral scalar field (the Higgs boson). Due to gauge invariance, the

⁶A ‘4-sphere’ is a sphere in four dimensions which arises due to the four components of ϕ (if ϕ were a single complex scalar field, its minimum would be described by a circle).

$SU(2)_L \otimes U(1)_Y$ Lagrangian does not contain the ξ fields, thus it is sufficient to express ϕ in terms of the Higgs field H only and insert the translated field $v + H$ into the Higgs Lagrangian (Equation 2.17).

Expanding the covariant derivative D_μ in \mathcal{L}_{Higgs} gives

$$\begin{aligned}\mathcal{L}_{Higgs} &= \frac{1}{2}(\partial_\mu H)(\partial^\mu H) + \frac{1}{2}(2\lambda v^2)H^2 \\ &\quad + \frac{1}{8}(gv)^2[(W_\mu^1)^2 + (W_\mu^2)^2] \\ &\quad + \frac{1}{8}v^2(g' B_\mu - gW_\mu^3)(g' B^\mu - gW_{3\mu}) \\ &\quad + \mathcal{L}_{BH},\end{aligned}$$

where \mathcal{L}_{BH} represents the interaction between the H , \mathbf{W} and B fields. Writing $W_\mu^\pm = \frac{1}{\sqrt{2}}(W_\mu^1 \mp iW_\mu^2)$, the physical gauge bosons W_μ^\pm can be identified with the mass term expected for a charged boson, $M_W^2 W^+ W^-$, to give

$$M_W = \frac{1}{2}(gv). \quad (2.20)$$

In addition, writing the fourth term of \mathcal{L}_{Higgs} as

$$\frac{1}{8}v^2(gW_\mu^3 - g' B_\mu)^2 + 0(g' W_\mu^3 + g B_\mu)^2, \quad (2.21)$$

the physical fields Z_μ and A_μ can be associated with the mass terms expected for neutral gauge bosons, $\frac{1}{2}M_Z^2 Z_\mu^2$ and $\frac{1}{2}M_A^2 A_\mu^2$. The normalised fields are

$$A_\mu = \frac{g' W_\mu^3 + g B_\mu}{\sqrt{g^2 + g'^2}} \quad Z_\mu = \frac{g W_\mu^3 - g' B_\mu}{\sqrt{g^2 + g'^2}}, \quad (2.22)$$

so that $M_A = 0$ and $M_Z = \frac{v}{2}\sqrt{g^2 + g'^2}$.

By defining

$$\tan \theta_W = \frac{g'}{g}, \quad (2.23)$$

the physical fields can be expressed in a more informative way as

$$\begin{aligned}W_\mu^\pm &= \frac{1}{\sqrt{2}}(W_\mu^1 \mp iW_\mu^2) \\ Z_\mu &= \cos \theta_W W_\mu^3 - \sin \theta_W B_\mu \\ A_\mu &= \sin \theta_W W_\mu^3 + \cos \theta_W B_\mu.\end{aligned}$$

In particular, the relationship between the M_W and M_Z is predicted (see Equation 1.2),

$$M_W = M_Z \cos \theta_W. \quad (2.24)$$

The Z boson and the photon thus emerge as orthogonal combinations of the W_μ^3 and B_μ fields and the fact that $M_W \neq M_Z$ is due to the mixing of W_μ^3 and B_μ . The electroweak Lagrangian contains no terms of the form $A_\mu A^\mu$, which ensures that the photon remains massless as a direct consequence of the $U(1)_Q$ gauge invariance of the vacuum. This fact is a consistency check rather than a SM prediction, whereas the relationship between M_W and M_Z is a direct prediction of the SM which depends on the particular Higgs doublet chosen and thus allows a check that the minimal SM Higgs picture is correct.

2.3 W^+W^- Cross Section

Since the measurement of the W mass from direct reconstruction relies on the accurate modelling of the *shape* of the invariant mass distribution, it is necessary to correctly set the ratio of signal to background in the MC simulation. This requires knowing the W^+W^- cross-section as a function of \sqrt{s} very well. The cross section σ for the process

$$e^+e^- \rightarrow f_1\bar{f}_2f_3\bar{f}_4 \quad (2.25)$$

can be expressed as the sum of a signal σ_{WW} and background σ_{bkg} component,

$$\sigma = \sigma_o^{WW}(1 + \delta_{EW} + \delta_{QCD}) + \sigma_{bkg}, \quad (2.26)$$

where background is intended to mean physics from non- W^+W^- processes and the contributions to σ_{WW} are described below:

- σ_o^{WW} represents the lowest order cross-section (Born approximation) for the CC03 diagrams in Figure 1.3. This is described in more detail in the next section.
- δ_{EW} are higher order electroweak corrections to σ_o^{WW} . Close to threshold the dominant contribution is from the long range electromagnetic interaction between almost stationary charged particles, the Coulomb correction. This is an example of a QED interconnection phenomenon between the two W bosons. The exchange of a soft photon distorts the W^+W^- lineshape and thus is expected to affect the measurement of M_W from the method of direct reconstruction. The estimated effect is to produce a negative shift in the average reconstructed mass of the order $20 \text{ MeV}/c^2$ [27]. The largest electroweak correction to the cross section comes from initial state radiation (ISR) which is the emission of photons collinear with the e^+e^- state prior to the e^+e^- interaction. This smears the W^+W^- lineshape near threshold by adding logarithmic terms to the cross section and thus makes it less sensitive to M_W . More importantly for the method of measuring M_W by direct reconstruction, imposing the constraint of the precisely known *nominal* centre of mass energy ⁷ causes

⁷This is a central feature of the analysis described in this thesis and will be discussed at length in Chapter 4.

a positive shift in the invariant mass distribution, since energy is carried away by the ISR photon. Finally, certain important higher-order fermion and boson loop corrections are incorporated by a suitable choice of the electroweak coupling constant α .

- δ_{QCD} are higher order QCD corrections for W^+W^- final states containing $q\bar{q}$ pairs. In general these can lead to additional jets in the final state from hard gluon emission, which may cause a bias in the reconstructed mass distribution since events are currently assumed to contain only four jets.

The actual $e^+e^- \rightarrow 4f$ process proceeds (for signal processes) through a double-resonant W^+W^- stage, where the W bosons are off-shell due to their finite width. A first step in describing this process is to consider the on-shell case where the W bosons are treated as stable particles. Unless otherwise stated, references for this section are in [11] and [28].

2.3.1 The On-Shell Cross Section

By considering the W^+W^- pairs as stable particles (on-shell) it is possible to calculate the total lowest order cross section analytically. The on-shell (Born approximation) cross section determines the essential features of W^+W^- production and decay, which are the building blocks for handling the proper off-shell case. The total on-shell cross section calculated for the CC03 diagrams in Figure 1.3 is [29]

$$\sigma_{Born} \simeq \frac{\pi\alpha^2}{s} \frac{1}{\sin^4\theta_W} \beta + \mathcal{O}(\beta^3), \quad (2.27)$$

where θ_W is the weak mixing angle and $\beta = \sqrt{1 - (\frac{2M_W}{\sqrt{s}})^2}$. s is the centre of mass energy squared and the sharp dependence of σ_{Born} on \sqrt{s} can be seen in Figure 2.3. The term proportional to β arises from the t -channel neutrino exchange diagram only, while the s -channel and the $s-t$ channel interference are proportional to β^3 . At $\sqrt{s} = 189$ GeV $\beta \sim 0.5$, making the t -channel process the dominant contribution to the W^+W^- cross section. In addition to the CC03 diagrams there is a tree level Higgs contribution to the cross section. However, this is suppressed by a factor m_e/M_W , where m_e is the mass of the electron, and is therefore completely negligible. For the full calculation however, it is necessary to include it to avoid unitarity problems at high energies.

2.3.2 The W Width

The production and decay of each W boson is described by a Breit Wigner (BW) resonance. The total width, Γ_W , of the BW is the result of summing the partial decay widths, $\Gamma_{W^\pm \rightarrow f_i \bar{f}_i}$, for each of the accessible W decay channels shown in Figure 1.4. These are calculated from the matrix element for each $W \rightarrow f \bar{f}$ process assuming massless fermions⁸. A precise measurement of Γ_W may therefore provide evidence for physics beyond the Standard Model, for example the decay of a W boson into supersymmetric particles. The width for each decay channel is affected by the corrections δ_{EW} and δ_{QCD} described in the previous section. These can be accounted for by parameterising the lowest-order (Born) width in terms of G_F and M_W , giving an improvement to the width calculated from the Born approximation in each channel [30],

$$\Gamma_{W^\pm \rightarrow \ell_i \nu_i} = \frac{G_F M_W^3}{6\sqrt{2}\pi}, \quad (2.28)$$

for leptonic decays, and

$$\Gamma_{W^\pm \rightarrow q_i \bar{q}_i} = \frac{G_F M_W^3}{6\sqrt{2}\pi} 3|V_{ij}|^2 \left(1 + \frac{\alpha_s(M_W^2)}{\pi}\right), \quad (2.29)$$

for decays into quarks. The factor 3 in Equation 2.29 corresponds to the number of quark colours⁹ and V_{ij} is the CKM matrix which describes the flavour mixing between quarks. The fact that the strong coupling constant α_s appears only in the quark partial decay width is due to the δ_{QCD} correction. The W width is then the sum of $\Gamma_{W^\pm \rightarrow q_i \bar{q}_i} + 3\Gamma_{W^\pm \rightarrow \ell_i \nu_i}$:

$$\Gamma_W = \frac{3G_F M_W^3}{2\sqrt{2}\pi} \left(1 + \frac{2\alpha_s(M_W^2)}{3\pi}\right). \quad (2.30)$$

The W mass measurement technique is discussed in detail in Chapter 5, but in short it relies on the calculation of the Born matrix element for the $e^+e^- \rightarrow 4f$ process to fit M_W . The dependence of M_W on Γ_W used in the fit to measure the W mass is taken to be the (Standard Model) relation in Equation 2.30 for the analysis in this thesis. Other approaches concerning the M_W measurement may be adopted,

⁸This is considered a valid approach since $m_f \ll M_W$.

⁹The electroweak interaction does not distinguish colour, so there are three identical contributions for a given decay mode.

for example Γ_W can be fixed to the SM prediction or be treated as a free parameter and fitted simultaneously with M_W .

The current world average measurement of the W width is [31] $\Gamma_W = 2.06 \pm 0.05$ GeV, in agreement with the SM prediction of $\Gamma_W = 2.067 \pm 0.021$ GeV.

2.3.3 The Off-Shell Cross Section

In a proper treatment of the process

$$e^+e^- \rightarrow W^+W^- \rightarrow f_1\bar{f}_2f_3\bar{f}_4, \quad (2.31)$$

the W bosons must be described as BW resonances with a finite width (off-shell) and their presence analysed through their decay products. In lowest order this is described by the CC03 diagrams in Figure 1.3 where both W's decay into a $f\bar{f}$ pair. However, the full four-fermion process contains contributions from other diagrams (452 in total) which have the same initial and final states, but proceed through different intermediate states. These are summarised in Table 2.3. Notice that only the two lightest quark generations are included, as the W cannot decay into t quarks and mixing between quark generations is suppressed by the CKM matrix, while the full lepton family is present. The total cross section for process 2.31 in terms of

	du	$\bar{s}c$	$\bar{e}\nu_e$	$\bar{\mu}\nu_\mu$	$\bar{\tau}\nu_\tau$
$d\bar{u}$	43	11	20	10	10
$e\bar{\nu}_e$	20	20	56	18	18
$\mu\bar{\nu}_\mu$	10	10	18	19	9

Table 2.3: Number of diagrams contributing to the $e^+e^- \rightarrow W^+W^- \rightarrow 4f$ process. The vertical and horizontal columns represent the W^- and W^+ bosons, respectively.

the total cross section for the process $e^+e^- \rightarrow W^+W^-$ with two off-shell W bosons, $\sigma(s, s_1, s_2)$, is [32]:

$$\sigma(s) = \int_0^s ds_1 \rho(s_1) \int_0^{(\sqrt{s}-\sqrt{s_1})^2} ds_2 \rho(s_2) \sigma_o(s, s_1, s_2), \quad (2.32)$$

where s is the e^+e^- centre of mass energy squared and s_1, s_2 are the invariant masses squared of the two virtual W bosons. $\sigma_o(s, s_1, s_2)$ is the $e^+e^- \rightarrow W^+W^-$ cross section from the CC03 diagrams (including their interference). The on-shell W^+W^- cross

section is then simply $\sigma_{on-shell} = \sigma_o(s, M_W^2, M_W^2)$. The weight factor $\rho(s_i)$ comes from the W boson propagator (BW resonance),

$$\rho(s_i) = \frac{1}{\pi} \frac{\Gamma(s_i)}{(s_i - M_W^2)^2 + \Gamma^2(s_i)}, \quad (2.33)$$

where,

$$\Gamma(s_i) = \begin{cases} s_i \frac{\Gamma_W}{M_W} & \text{running width} \\ \Gamma_W M_W & \text{fixed width} \end{cases}$$

Equation 2.32 shows that the dependence of the cross section on Γ_W and M_W enters exclusively through the off-shell W propagator (neglecting the small dependence through radiative corrections) and has a large effect on the Γ_W and M_W measurements in the threshold region (see Figure 2.3). Precision measurements made during LEP1 at the Z resonance used a *running* width in the description of the Z boson propagator, while the Monte Carlo used for the W mass measurement in this thesis uses a *fixed* width in the W propagator¹⁰. To make the measurements consistent for the LEP result combination, the following correction must be applied to the measured W mass, M_W^{meas} [33]:

$$M_W = M_W^{meas} - \frac{1}{2} \frac{(\Gamma_W^{meas})^2}{M_W^{meas}} = M_W^{meas} - 27 \text{ MeV}/c^2. \quad (2.34)$$

The issue of gauge invariance arises from two sources when going from the on-shell to the off-shell W^+W^- pair production cross section. The first is the result of using an incomplete set of diagrams (only the CC03 diagrams) in the cross section calculation. The only way to obtain a gauge invariant result is to include all contributing four-fermion diagrams. However, this is inefficient due to the complexity of the calculation and in practice the CC03 approximation is sufficient, at least for the direct W mass measurement within current statistics.

The second and more fundamental source concerns the poles which occur in the resonant diagrams. This is the case where $s = M_W^2$ in Equation 2.33. These singularities have to be cured by introducing the finite width in one way or another, while at the same time preserving gauge invariance and unitarity. Again, the inclusion of all contributing diagrams can solve this, since in field theory such a width naturally

¹⁰This is not to be confused with the way the M_W dependence on Γ_W is treated in the fit procedure (as discussed in Section 2.3.2); the current discussion is the actual treatment of the finite W width in the W boson propagator.

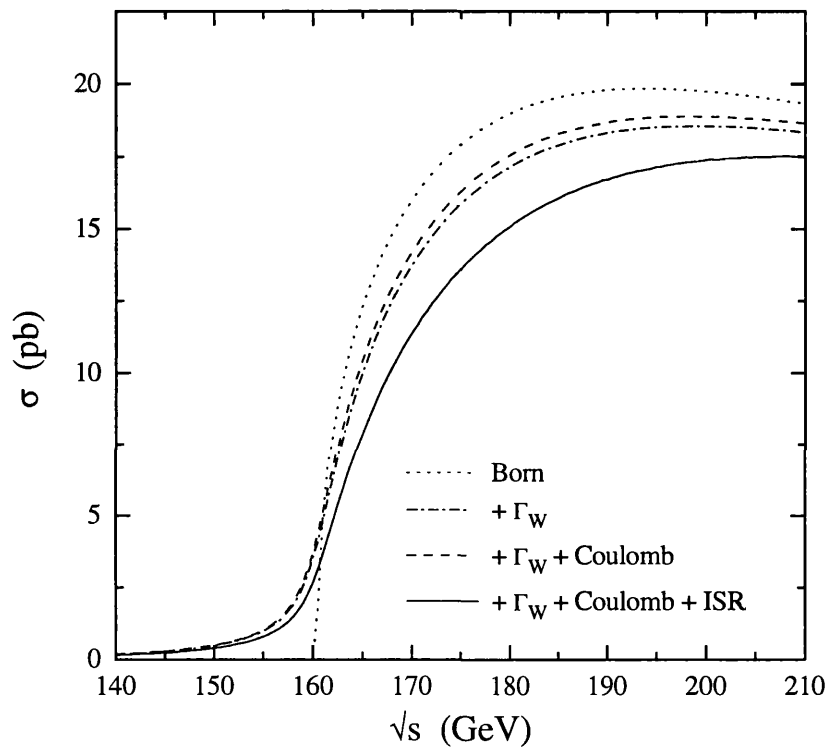


Figure 2.3: The $e^+e^- \rightarrow W^+W^-$ cross section showing the effect of various approximations: (i) Born (on shell) cross section, (ii) Born (off shell) cross section, (iii) including Coulomb corrections, and (iv) including initial state radiation (ISR correction).

arises from the imaginary parts of higher order diagrams. A discussion of the many schemes that have been developed to solve this problem, including the *fixed* and *running* widths mentioned above, is given in ref. [28] pp. 110-115.

2.4 Fragmentation

The short distance interactions of fundamental particles can be described using perturbative quantum field theory, which is sufficient for the case of leptons and colourless bosons. For the case of the quarks and gluons, which are confined in colourless hadrons by the nature of the strong force, an additional picture is necessary to describe the transformation of coloured partons into colourless jets. This process can be divided into three stages:

Parton shower: where the initial partons split into quarks and gluons (perturbative QCD);

Hadronisation: where these combine to form jets of hadrons, leptons and photons;

Decay: the subsequent decay of particles formed after hadronisation.

These definitions vary between texts, but for the purpose of discussion in this section, and in the evaluation of their systematic effects on the W mass measurement (Section 5.6.2), they are replaced by the single term ‘fragmentation’ in the following. For the case of $e^+e^- \rightarrow W^+W^- \rightarrow q\bar{q}q\bar{q}$ processes the initial parton structure of four quarks therefore becomes considerably more complicated, producing final states of perhaps > 50 particles. The hadronisation process is not yet understood from first principles, and is based on phenomenological models.

The most developed hadronisation model to date is the ‘string fragmentation’ model [34], which describes the colour dipole field between the initial $q\bar{q}$ pair as a narrow flux-tube or ‘string’. The constant energy per unit length of the tube causes the energy stored in the colour field to increase linearly with the quark separation, which may become large enough to create a new $q\bar{q}$ pair, thus ‘breaking’ the string. The adjacent quarks at the end of each string are then combined to form hadrons

(baryons containing 3 quarks and mesons containing quark pairs) which may subsequently decay further. The decay stage is simulated using tables of decay modes and branching ratios to distribute the contents of the final state. The string fragmentation model forms the basis of the JETSET program [35], which is implicit in the $W^+W^- \rightarrow q\bar{q}q\bar{q}$ Monte Carlo event simulation used in the analysis in this thesis.

The HERWIG program [36] is an alternative general purpose event generator which describes the hadronisation process using a ‘cluster fragmentation’ model. In this picture, jets of quarks and antiquarks are formed from gluon splitting which are then combined in all allowed colour-singlets to form clusters. Each cluster has a mass distribution and spatial size and fragments into hadrons according to these properties.

2.5 Final State Interactions

The Monte Carlo event simulation used in this analysis assumes the W^+ and the W^- decays are independent and that each W system proceeds through the fragmentation stage without reference to the other. At LEP2 energies the average separation of the W^+W^- decay vertices is ~ 0.1 fm (due to the large W width), which is less than the typical hadronisation distance (~ 1 fm). In the hadronic decay channel the subsequent fragmentation of the two W ’s into streams of hadrons (jets) may therefore no longer be considered independent. This will influence the W -mass reconstruction [37]. These Final State Interactions (FSI) can be identified as two different physical processes, colour reconnection and Bose Einstein effects. Their understanding is of paramount importance for a precision measurement of the W mass from the hadronic channel¹¹.

¹¹Since the semi-leptonic channel contains only a single hadronic W decay, and therefore no interconnection effects, evidence for FSI may be revealed through comparing observables from the semi-leptonic and hadronic channels. This will be discussed in Chapter 7.

2.5.1 Colour Reconnection

Colour reconnection (CR) is a QCD phenomenon relating to the connection of coloured partons parented by the two different W 's in the hadronic final state. In the process $e^+e^- \rightarrow W^+W^- \rightarrow q_1\bar{q}_2q_3\bar{q}_4$, the colour singlets ($q_1\bar{q}_2$ and $q_3\bar{q}_4$) may be transmuted to new ones ($q_1\bar{q}_4$ and $q_3\bar{q}_2$). This can therefore bias the reconstruction of the invariant mass distribution.

The perturbative part of W decay is firmly based on fundamental QCD and the effect of CR in this region is predicted to be small [37]. However, the non-perturbative stage where CR is predicted to have a large influence relies on phenomenological models. All current CR models are based on a space-time picture, in which objects are formed at the hadronisation stage through a local interaction which may combine products of the two W decays in regions where they overlap.

JETSET contains two main models labelled (I) and (II), based on different hypotheses on the structure of the QCD vacuum and of the confinement mechanism.

- **Model (I)** Fragmentation strings are viewed as cylinders and the probability of reconnection in each event is related to the overlap ϕ of the colour strings:

$$\mathcal{P}_{reco} = 1 - e^{-k_\phi\phi}, \quad (2.35)$$

where k_ϕ is a parameter governing the strength of CR.

- **Model (II)** Strings are viewed as vortex lines with thin cores and reconnection takes place when the core regions of two strings intersect. An additional model II' is similar but reconnection is suppressed if there is no reduction in the overall string length.

The reconnection probability in Model (II) is partly predicted, while in Model (I) it is a completely free model parameter, k_ϕ . The effects of CR are therefore difficult to estimate as their strength is not predicted absolutely.

2.5.2 Bose Einstein Correlations

BE effects are phenomena arising from Bose Einstein statistics [38] and account for a significant uncertainty on the measurement of M_W in the hadronic channel. The effect was first observed in the angular distributions of like charge pions in $p\bar{p}$ collisions [39], which showed deviations from the angular distribution for *unlike* charge pions. In the standard (Fermi-Dirac) statistical model this distinction cannot be made.

The BE effect in collider physics is studied using the two-boson correlation function $f(Q)$, where $Q^2 = (\mathbf{p}_1^2 - \mathbf{p}_2^2)$ is a measure of the distance in momentum space between two bosons with momentum \mathbf{p}_1 and \mathbf{p}_2 . The BE enhancement $f(Q)$, relative to a reference with no BE effects, occurs at low Q^2 and is parameterised by

$$f(Q) = 1 + \lambda e^{-R^2 Q^2}, \quad (2.36)$$

where R is the radius of a Gaussian source describing particle production and λ is the incoherence (effective strength) parameter, in the range $0 \leq \lambda \leq 1$.

The overlap of the hadronisation regions of the W^+ and W^- might cause an enhancement of the production of identical bosons (mainly pions) from different W 's, relative to the production from two single W decays. This could result in a bias in the reconstructed invariant mass distribution. The effect on the W mass is difficult to estimate because BE correlations arise from quantum mechanical interference which is simply not included in Monte Carlo simulation.

Attempts at describing BE effects include models where the final state particles are redistributed to reproduce the expected two-boson momentum correlations, although in adjusting particle momenta to respect overall energy and momentum conservation this induces spurious long-range correlations and the implications for the W mass may be severe [38]. Other models prescribe a weight for each event which gives more statistical power to events with, for example, pairs of equal-sign particles closer in momentum [40]. This method arises naturally in a quantum mechanical approach but is lengthy because all final state particle permutations must be computed.

Chapter 3

Experimental Apparatus

3.1 Introduction

The Large Electron Positron collider (LEP) is the world's largest e^+e^- storage ring, situated beneath the Franco-Swiss border at CERN, Switzerland. It was built primarily for the study of the Z and W bosons and also to search for physics beyond the Standard Model. ALEPH [41] is an experiment located around one of the four interaction points (IPs) of LEP, the other experiments being DELPHI [42], OPAL [43] and L3 [44]. ALEPH was designed to offer a large acceptance for the particles produced in e^+e^- collisions. This chapter is devoted to a brief description of LEP and the ALEPH detector with emphasis on the measurement of the centre of mass energy of LEP, which is important for the W mass measurement described in this thesis.

3.2 The LEP Experiment

LEP [45] is situated within a tunnel of diameter 3.8m, at a depth of between 80 to 150m. (see Figure 3.1). Its 26.67 km circumference is constructed from 8 straight sections, linked together by curved ones and the ring lies in a seam of soft rock at an incline of $\sim 1.4\%$. The beam pipe itself is elliptical in cross section and surrounded by various magnetic optics necessary to manipulate the bunches of electrons and positrons as they travel around the ring at a rate of ~ 11 kHz under a vacuum of pressure $\sim 10^{-9}$ Torr. There are 3400 dipole bending magnets to guide the beams

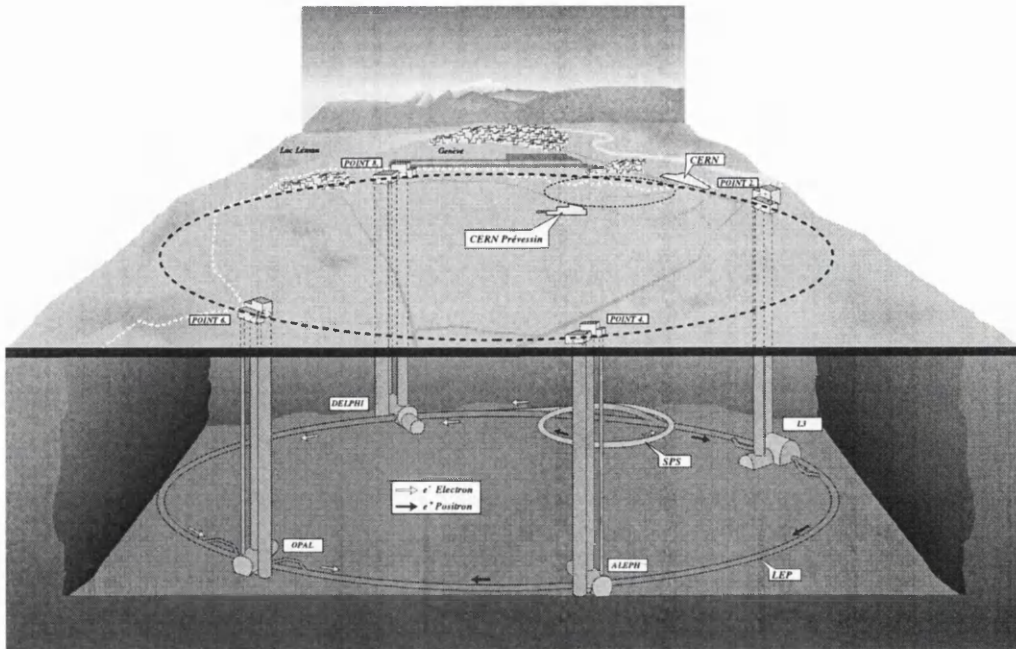


Figure 3.1: Situation and layout of the LEP collider (exaggerated depth).

through a circular orbit and some 1902 quadrupoles, sextupoles and corrector magnets to contain them within the beam pipe. A system of superconducting radio frequency cavities are used to accelerate the electrons and positrons through potential gradients of up to 2300 MV. The beam pipe is constructed from aluminium to prevent field distortions, and is narrower at the IPs where the beams are further focussed with superconducting quadrupoles to ensure a high luminosity (particle production rate).

LEP is the final stage of a large accelerator complex at CERN, illustrated in Figure 3.2. From their production using a pulsed electron gun, electrons are accelerated in a 200 MeV linear accelerator and positrons produced by firing a portion of these into a tungsten converter, producing e^+e^- pairs. The LEP Linear Injector (LIL) then accelerates the electrons and positrons to 600 MeV whence they are fed into the Electron Positron Accumulator (EPA) and separated into bunches. The EPA then injects these into the Proton Synchrotron (PS), a 3.5 GeV e^+e^- synchrotron. These are then fed to the Super Proton Synchrotron (SPS) where they are accelerated to an energy of 20 GeV. Finally they are transferred into LEP where they are

further accelerated to their collision energy.

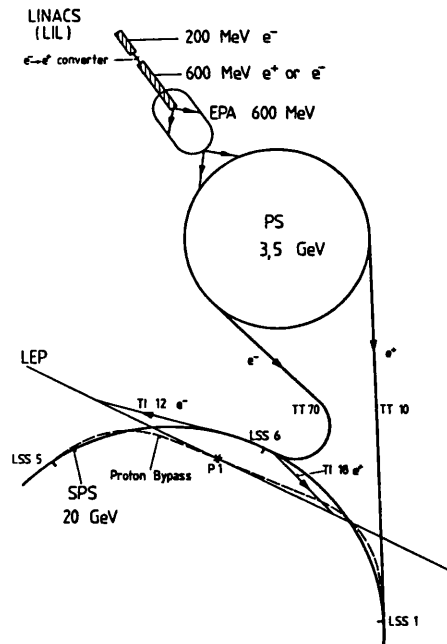


Figure 3.2: Plan view of the LEP injection system.

The LEP1 phase of the machine was devoted to colliding e^+e^- beams of energy ~ 45.5 GeV, allowing particle production via the production and decay of the Z^0 boson. ALEPH collected over four million Z^0 decays which, combined with the other LEP experiments, enabled rigorous tests of the Standard Model. Since 1996, LEP has been operating at a centre of mass energy above that for W^+W^- pair production which is approximately $\sqrt{s} = 161$ GeV. The LEP2 phase will continue into 2000 when the centre of mass energy is expected to reach above 200 GeV¹.

By the end of LEP2 the combined luminosity from all four experiments is expected to allow a statistical precision of 25-30 MeV/ c^2 on the W mass measurement. The uncertainty on the LEP centre of mass energy E_{beam} translates directly to M_W ,

$$\frac{\Delta M_W}{M_W} \sim \frac{\Delta E_{beam}}{E_{beam}}, \quad (3.1)$$

and needs to be < 15 MeV if it is not to make a significant contribution to the systematic error on the W mass measurement.

¹During 1999 LEP reached a centre of mass energy of 202 GeV.

3.2.1 Energy Measurement at LEP1

At LEP1 the average energy around the LEP ring was determined very precisely by a method known as resonant depolarisation (RDP) [46]. This method has been used at other e^+e^- storage rings, providing accurate measurements of the mass of the ω , ϕ and J/ψ mesons, and led to the determination of the Z boson mass at LEP1 to within $2 \text{ MeV}/c^2$.

RDP makes use of the transverse polarisation of the electrons in the beam (Sokolov-Ternov effect). The evolution of the spin vector \vec{S} of a relativistic electron in electromagnetic fields \vec{E} and \vec{B} is described by the Thomas-BMT equation

$$\frac{d\vec{S}}{dt} = \vec{\Omega}_{BMT} \times \vec{S}, \quad (3.2)$$

where,

$$\vec{\Omega}_{BMT} = -\frac{e}{\gamma m_e} \left[(1 + a_e \gamma) \vec{B}_\perp + (1 + a_e) \vec{B}_\parallel - \left(a_e \gamma + \frac{\gamma}{1 + \gamma} \right) \vec{\beta} \times \frac{\vec{E}}{c} \right] \quad (3.3)$$

and \vec{B}_\perp and \vec{B}_\parallel are the transverse and parallel magnetic field components with respect to the particle's velocity βc . e is the charge, m_e the mass, a_e the anomalous magnetic moment and γ the Lorentz factor of the electron. The electrons are maintained in a circular orbit by strong vertical fields B_y produced by the dipole bending magnets, and their precession frequency in the ring is given by the cyclotron frequency $\Omega_C = -(e/\gamma m_e) B_y$. Comparing the definitions of Ω_{BMT} and Ω_C the spin vector will precess $a_e \gamma$ times for one revolution in the storage ring, where the term $a_e \gamma$ is called the spin tune ν . The spin tune is directly proportional to the beam energy :

$$\nu = \frac{a_e E_{beam}}{m_e c^2} = \frac{E_{beam} [MeV]}{440.6486(1) [MeV]}. \quad (3.4)$$

Since a_e is known to within 20 parts per billion (ppb), a measurement of ν provides E_{beam} to high accuracy.

RDP is produced by exciting the beam with an oscillating radial field generated by a vertical kicker magnet. If the resulting spin kick is in phase with the spin precession a resonance condition occurs, the electron spins are swept away from the vertical and polarisation disappears. Because the beam encounters the field only once per turn, the frequency of the resonance depends on the fractional part of the spin tune δ_s .

3.2.2 Energy Measurement at LEP2

Transverse polarisation cannot be maintained at LEP2 energies since the natural increase in beam energy spread overlaps the integer depolarising resonances, therefore RDP cannot be applied². Instead the LEP2 beam energy is determined by an extrapolation of RDP measurements at lower energy points to physics energies.

Since the beam energy is proportional to the total LEP bending field,

$$E_{beam} \propto \oint B \cdot dl,$$

the linearity of this extrapolation can be checked at high energies. The magnetic field is sampled at 16 points around the curved sections of LEP using very accurate NMR probes, and the relationship between these measurements and the beam energy can be precisely calibrated using RDP. The problem is that the NMR probes do not actually measure the *total* bending field of LEP and so their measurements are cross-checked using the ‘flux-loop’. This is the result of integrating magnetic field readings from all 3400 bending magnets, which gives a measurement of $\sim 97\%$ of the total LEP bending field. These magnetic measurements are the largest source of error in the beam energy measurement at LEP2 as non-linearities begin to appear between the NMR and flux-loop measurements at high energies. This is illustrated in Figure 3.3. The systematic contribution to the beam energy measurement from the extrapolation alone is the dominant uncertainty, estimated at 15 MeV for 1998 data taken at $\sqrt{s} = 188.6$ GeV. The total error on the beam energy is estimated to be 20 MeV [47].

In order to realise $\sigma(E_{beam}) \sim 10$ MeV, new methods have been sought. The most promising method is known as the LEP Spectrometer project [48]. This utilises a simple principle, illustrated in Figure 3.4, to measure E_{beam} based on precise measurements of the deflection of the beam through a known magnetic field.

The spectrometer will not make an absolute energy measurement, as the Beam Orbit Monitors (BOM’s) can only give a relative beam position. The absolute energy scale is set by calibrating the apparatus at the Z resonance using RDP. This enables the spectrometer to perform a continual beam energy measurement.

²The highest beam energy for which RDP has been observed is 61 GeV.

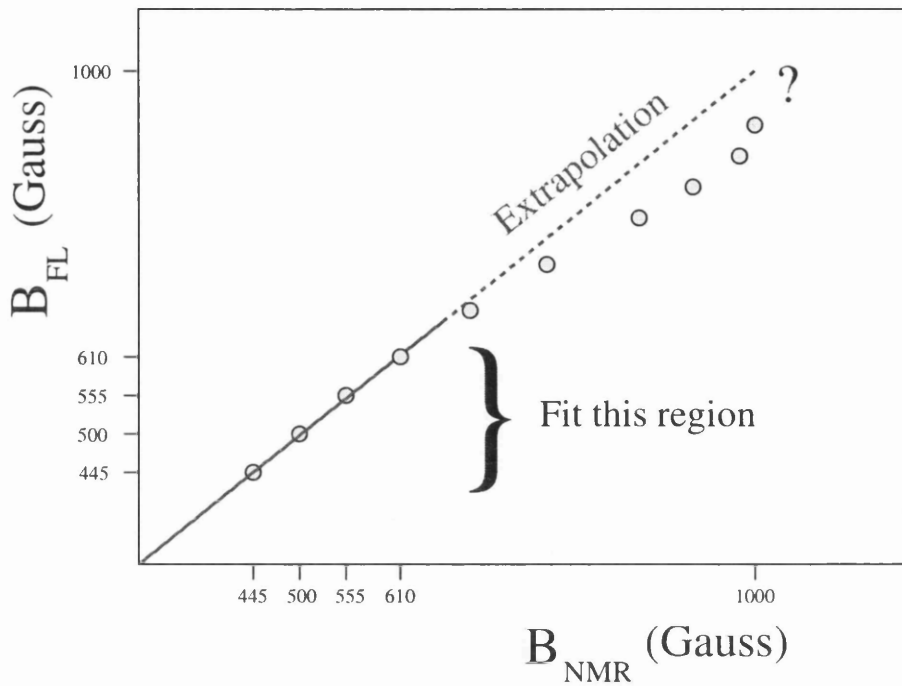


Figure 3.3: Schematic illustration of the source of uncertainty in the LEP2 centre of mass energy measurement. RDP measurements at low energy are extrapolated to LEP2 physics energy, where there is a disagreement between the two methods for calculating the total LEP bending field.

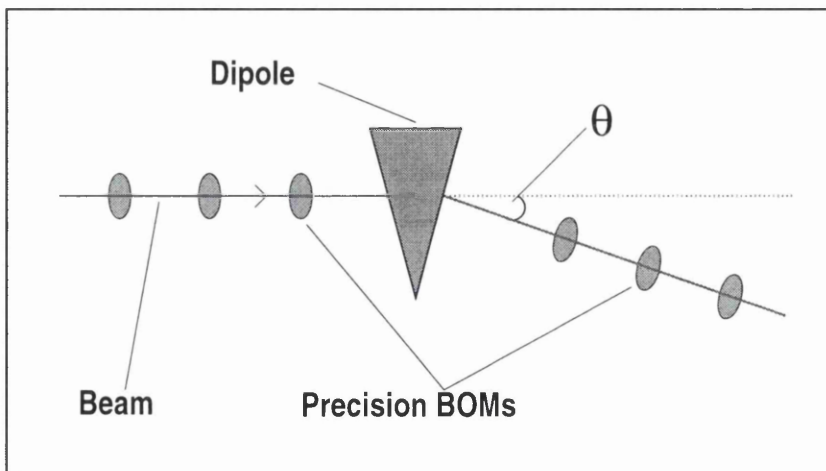


Figure 3.4: The principle of the LEP spectrometer. The beam energy is proportional to the angle of deflection of the beam through a known magnetic field.

In order to obtain $\sigma(E_{beam}) \sim 10$ MeV the project relies on measurements of the beam deflection θ and the dipole bending field B_{dipole} to the level of 10^{-5} . This presents a formidable experimental challenge, and due to restrictions in the tunnel once the spectrometer is in place, the mapping of the dipole has to be performed on a test bench before installation. The BOMs are able to give relative positions to a precision of $\sim 1\mu\text{m}$.

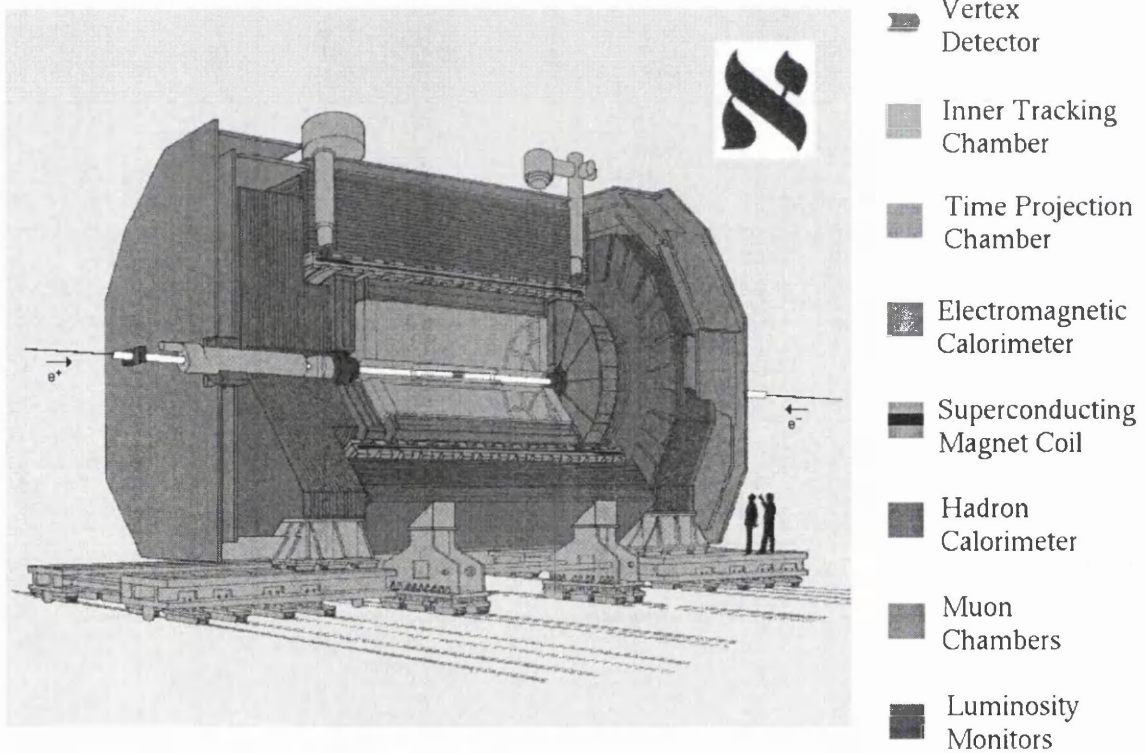
Assuming the field can be well modelled, taking into consideration environmental effects and the time dependence of the field during ramping, there is then the problem of physical deformation during transit or installation. The problem is complicated further by the fact that the magnetic field extends beyond the physical length of the dipole by up to 3m either side. The BOM's lie within these highly non linear fringe fields, each one shielded with copper collimators to prevent damage from synchrotron light, which will distort the field further.

To perform the measurement of $\int Bdl$, an automated system is designed which will map the dipole completely and record all relevant parameters for B , as mentioned above. Work began on the data acquisition program for the twenty three temperature probes mounted on the dipole, which could later be combined with the magnetic measurements to parameterise the field.

In 1998 one 'arm' of the spectrometer was in place and closely monitored for its stability. It was found to be mechanically and thermally stable to the desired level of 10^{-4} . In 1999 the spectrometer was fully installed and measurements of the beam deflection were made. These measurements may be reliable enough to allow a reduction in the systematic uncertainty on the W Mass due to ΔE_{beam} for data taken during 1999.

3.3 The ALEPH Detector

The e^+e^- interactions at LEP typically produce events with an average of > 30 charged and neutral particles distributed over the entire solid angle. The event rate is also low, particularly at LEP2 energies. The ALEPH detector [41] (A Detector for LEP Physics) was thus constructed to cover as much of the solid angle as possible³. ALEPH is designed to measure the momenta of charged particles, the energy deposited by charged and neutral particles and to provide particle identification. In addition, high spatial resolution in dense jets and the detection of particles with very short lifetimes were aimed for. To achieve this the detector is built in six cylindrical layers (sub-detectors) around the interaction point (IP). See Figure 3.5. It weighs over 3000 tons and has some 700 000 individual readout channels.



The ALEPH Detector

Figure 3.5: Schematic showing a cutaway view of the ALEPH detector.

³In practice ALEPH achieves a coverage of $\sim 3.9\pi$.

Tracking is performed by three sub-detectors: a vertex detector immediately surrounding the IP, a drift chamber which also provides part of the trigger system and a large time projection chamber (TPC) which extends to a radius of 1.8 m. The magnet bends charged tracks in a field of 1.5 Tesla in order to obtain momentum and energy measurements from the TPC. Energy measurement is achieved by a highly granular electromagnetic calorimeter and a 1.2 m thick iron hadronic calorimeter which also serves as the return yolk for the superconducting solenoid. The outermost layer is for muon identification, the only particles energetic enough to penetrate this far (neutrinos escape the entire detector). In addition, smaller sub-detectors measure the intensity and condition of the beams delivered to the experiment by LEP. Unless otherwise stated, references for this section are in [49, 50].

3.4 Tracking

3.4.1 Vertex Detector

The Vertex DETector (**VDET**) is a silicon microstrip device which extends from a radius of 5.5 to 12.8 cm, constrained by the beam pipe and inner tracking detector respectively. Its purpose is to identify short-lived particles, particularly b and c quarks, with a high efficiency. An upgrade of the original VDET was installed for LEP2, which increases the angular coverage, contains less passive material and is more able to cope with the higher radiation dose [51]. This improvement has provided a better chance for the discovery of the Higgs ⁴.

It is constructed from two concentric layers of silicon wafers, separated maximally to increase the lever arm for track reconstruction, which have readout electronics on both sides. Strips parallel to the beam provide the azimuth angle ϕ of tracks, while the perpendicular strips measure the z -coordinate. These measurements have a spatial resolution (normal incidence) of ~ 10 and $16 \mu\text{m}$ respectively, and the 40 cm length of active material gives an angular acceptance of $|\cos\theta| < 0.95$, where θ is the angle relative to the beam direction.

⁴The Higgs is expected to decay predominantly into b quarks.

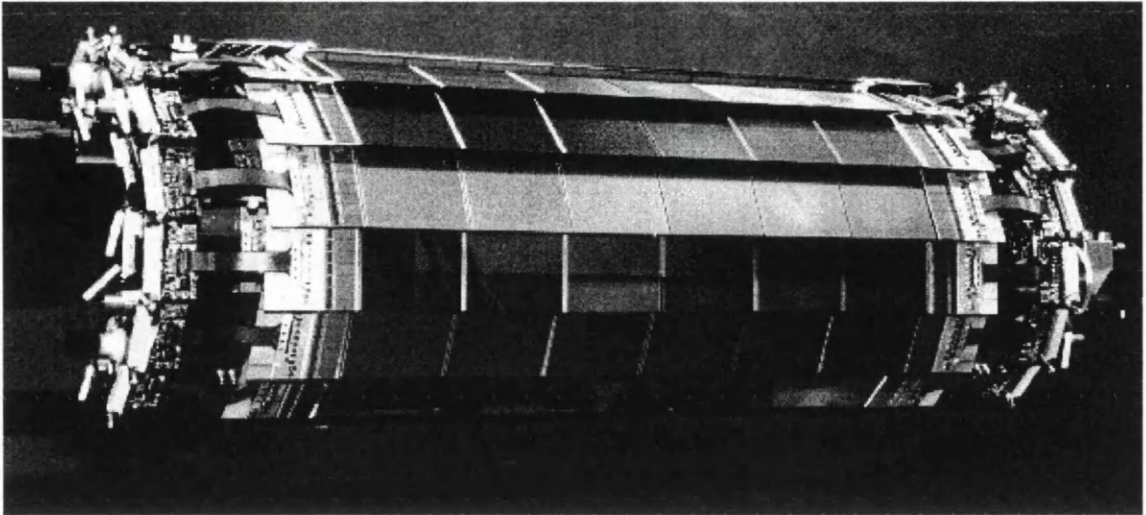


Figure 3.6: Photograph of the LEP2 Vertex Detector.

3.4.2 Inner Tracking Chamber

The second tracking component is the Inner Tracking Chamber (ITC) [52]. This is a 2 m long cylindrical drift chamber which covers the radial region of ALEPH between 16 and 26 cm. It consists of eight concentric layers of anode sense wires (960 wires in total) where each wire acts as an individual proportional counter, thereby allowing good spatial resolution. Hexagonal drift cells parallel to the beam are defined by six surrounding wires held at ground potential, illustrated in Figure 3.7. Neighbouring cells share two common wires, to form a ‘close-packed’ structure which reduces left-right ambiguity in associating hits to tracks.

The resolution in $r - \phi$ is determined by the cell drift time and is on average $\sim 100 \mu\text{m}$, which provides a maximum of 8 $r - \phi$ points usable for tracking. The z -coordinate is measured from the drift time at the ends of the wires themselves and thus has a resolution of a few cm. The ITC can therefore provide three dimensional readout of charged-particle trajectories, and the fact that the drift cells are small means this information is available for the trigger in less than $3 \mu\text{s}$. It provides the only tracking information arriving in time for the Level 1 trigger decision.

3.4.3 Time Projection Chamber

The Time Projection Chamber (TPC) [53] is the main tracking detector in ALEPH. It is a large, cylindrical drift chamber extending from 0.26 to 1.8 m radially within

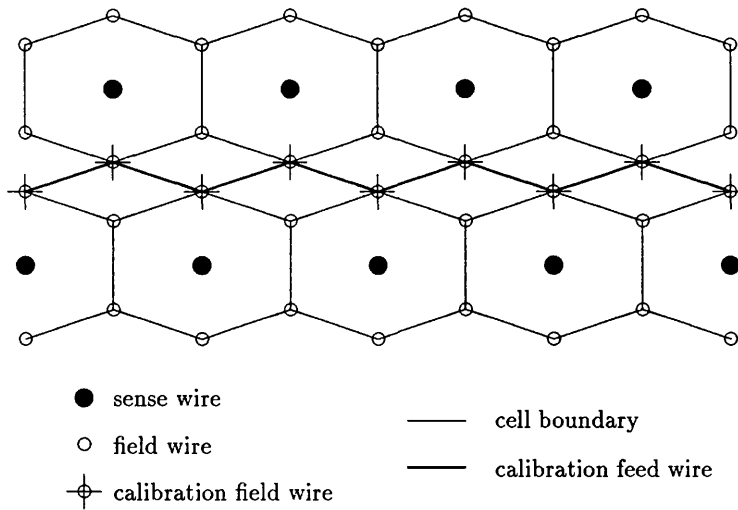


Figure 3.7: Diagram showing the drift-cell structure in the ITC.

the superconducting solenoid, its dimensions being motivated by the need for a good momentum and angular resolution as well as optimum pattern recognition in the high multiplicity events resulting from e^+e^- annihilations. Figure 3.8 shows the basic elements of the detector.

Electrons produced by the ionising passage of a charged particle through the argon-methane chamber travel in tight spirals through a highly uniform electric field and arrive at the two end plates. Here, the signal is recorded by a system of proportional wire chambers arranged in a pattern of 18 sectors, and read out using segmented cathode pads arranged in 21 concentric circles lying just behind the wire planes. The ϕ coordinate is determined by interpolating signals induced on nearby pads and the r coordinate is simply measured by the radial position of those pads. A measurement of the drift time, along with a knowledge of the drift velocity, provides a measurement of the z coordinate and thus the TPC system provides 21 three dimensional coordinate measurements for fully contained tracks. Figure 3.9 shows a slice through the edge of a sector.

Above the cathode wire plane lies a grid of wires for the TPC gate, which is used to prevent the build up of space charge in the drift region due to positive ions resulting from the avalanches on the cathode plane. Such space charge build up would influence the local electric field and distort tracks. The gating grid is ‘open’

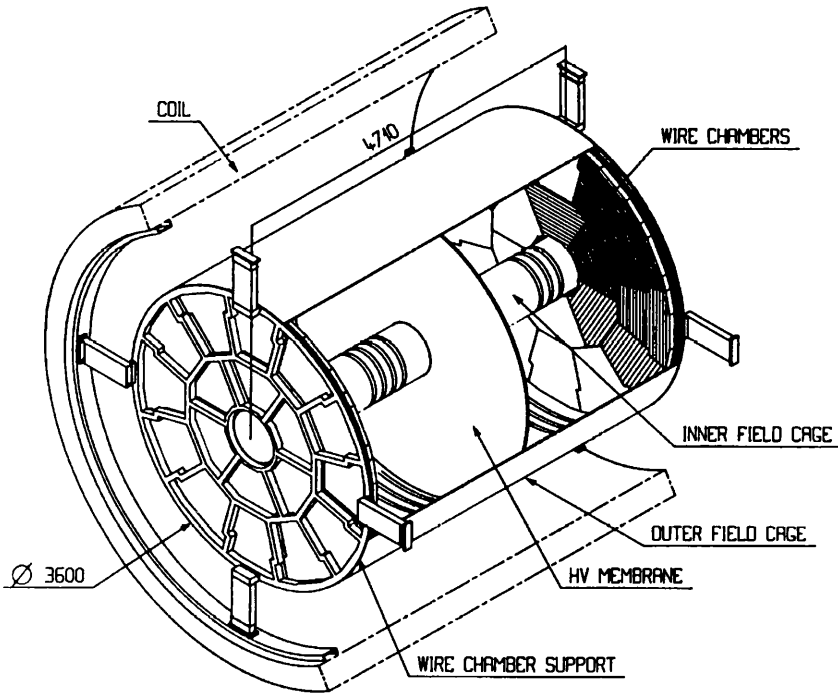


Figure 3.8: Cut-away view of the Time Projection Chamber. The central membrane is held at negative potential while the end-plates are grounded, giving rise to an axial electric field for the ion pairs to pass through.

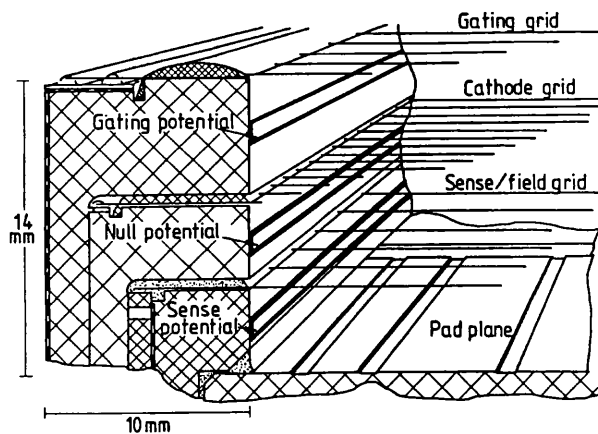


Figure 3.9: Side view of a TPC sector edge showing the pad-wire plane.

when the trigger decides to read out an event by placing a negative potential on the wire plane so that it is transparent to the passage of charged particles. In the closed state a positive potential is placed on alternate wires, thus preventing positive ions escaping into the chamber.

The spatial resolution in $r-\phi$ is $\sim 180 \mu\text{m}$ at $\theta = 90^\circ$. It depends on the magnetic field and the incidence of the track with respect to the pad-wire plane. The z resolution of $\sim 1 \text{ mm}$ is dominated by electronic systematics caused by varying cable lengths and pulse shaping time across the end plates. The error on the momentum can be expressed by the formula

$$\frac{\Delta p}{p} \simeq 10^{-3} p(\text{GeV}/c) \left(\frac{\langle \sigma \rangle}{150 \mu\text{m}} \right) \left(\frac{1.5\text{T}}{\text{B}} \right) \oplus 0.003,$$

where p is the transverse momentum and $\langle \sigma \rangle$ the average error on each coordinate. The last term, which has to be added in quadrature, is due to multiple scattering in the chamber gas. A momentum resolution of $\Delta p/p^2 = 1.2 \times 10^{-3} (\text{GeV}/c)^{-1}$ is obtained from studying $Z^0 \rightarrow \mu^+ \mu^-$ events.

To monitor track distortion and to provide a measurement of the drift velocity within the chamber, a laser calibration system is in place [54]. Two NdYAG lasers fire UV shots which are split into 30 beams within the TPC and arranged so as to simulate their origin at the interaction point (Figure 3.10). The ionisation tracks left in the chamber are straight and multiple shots can be fired reducing the statistical error. It is thus an excellent way to study systematic effects in the detector.

It is essential that the system be fully automated during the data taking and there are many practical considerations. The energy output of the lasers must be sufficient to cause ionisation in the TPC gas with maximum efficiency. The ionisation levels are constantly monitored and the laser voltage adjusted accordingly to achieve optimum operation. Over the course of the year dust from the cavern walls entering the optical path becomes ‘burned’ onto the optical elements. Once a reasonable maximum laser voltage no longer causes ionisation, manual intervention is required. Using a soft alcohol solution and acetone each element within the laser itself must be cleaned, and occasionally replaced. In addition, great care must be taken so as not to lose the alignment of the system. The lever arm is such that a beam displacement

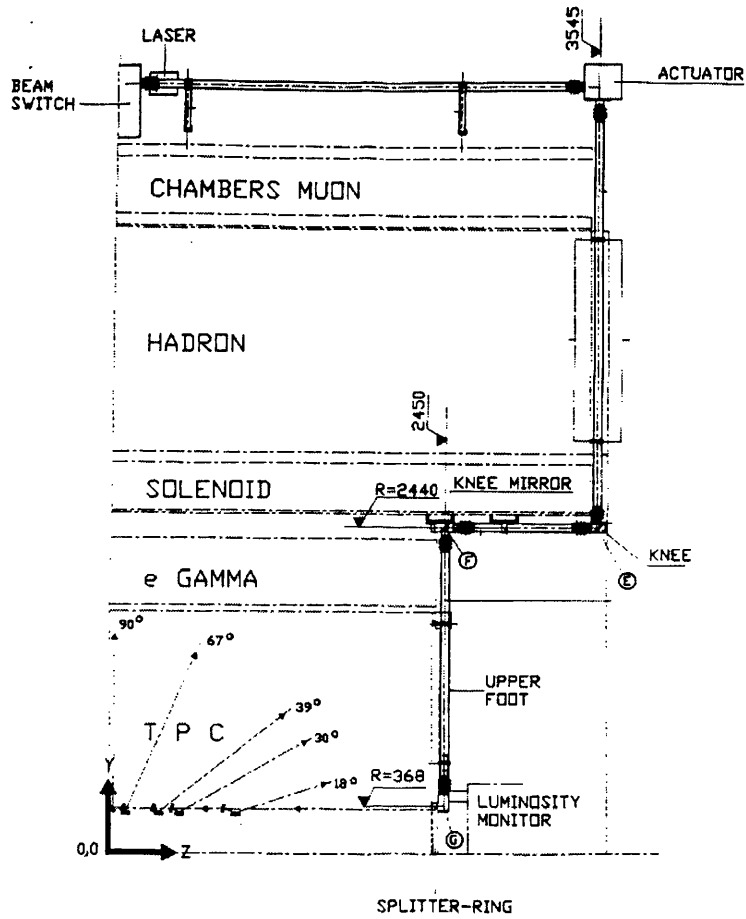


Figure 3.10: The TPC laser calibration system.

of 1 mm at the laser output translates to a few cm in the TPC, which is more than enough to lose the alignment. The mirrors used to guide the beams into the detector are mounted on motors enabling rotation and translation of the mirror surface. A remote system thus enables the alignment to be regained, but only when it has not moved too much. In one instance the alignment was lost on one side of the TPC for most of the 1997 physics data taking, due to a disturbance of the inner mirror knee on the closing of the ALEPH end caps. The laser system does not have enough priority to force the whole detector to be affected in its maintenance, as although it provides good cross-checks, it does not affect the ALEPH data taking. During the run in 1997 the control software for the laser system was completely re-written and improved greatly, ensuring smooth operation throughout 1998 and 1999.

Finally in addition to its role as a tracking detector, the TPC wire plane measures the energy loss by ionisation, dE/dx , thus providing particle identification via the Bethe-Bloch formula. This, along with calorimeter information, provides excellent electron identification in jets and can distinguish pions from kaons or protons. The resolution on dE/dx measurements is $\sim 1.5\%$.

3.4.4 Track Reconstruction

Associating detector hits to tracks to reconstruct the passage of a charged particle through ALEPH begins with the TPC. First of all, neighbouring hits are linked to form track segments, then the segments are connected together with the condition that a helix hypothesis is fulfilled. The track is then extrapolated into the ITC and VDET, where consistent hits are assigned, and after fitting with the errors on the hits the final reconstructed track is built. Table 3.1 summarises the measured resolution on the fitted track for these stages, using $Z \rightarrow \mu^+\mu^-$ events, and Figure 3.11 is an enlarged cross section of the ALEPH central tracking region, showing the associated hits.

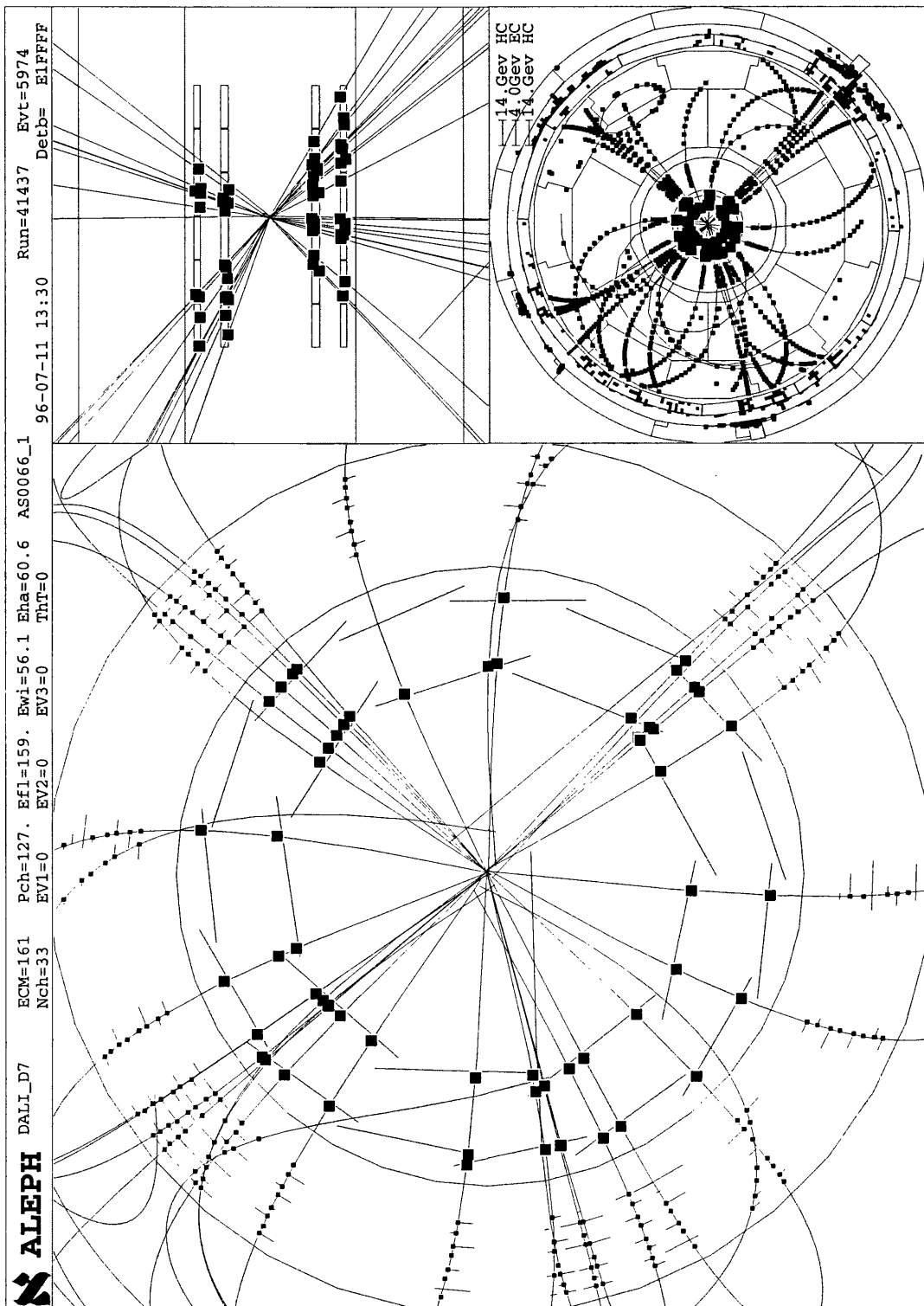


Figure 3.11: A W^+W^- decay into 4 jets showing the VDET and ITC (bottom and top left). Nearly all tracks passing through the VDET have been assigned to hits. The full ALEPH detector (fish eye view) including the TPC and calorimeters is shown in top right.

Tracking Detector	$\sigma p/p^2$ (GeV/c) ⁻¹
TPC	1.2×10^{-3}
+ ITC	0.8×10^{-3}
+ ITC and VDET	0.6×10^{-3}

Table 3.1: Momentum resolution of the ALEPH tracking detectors.

3.5 Calorimetry

3.5.1 Electromagnetic Calorimeter

The ALEPH electromagnetic calorimeter (ECAL) exploits the electromagnetic shower phenomenon [55] to detect high energy electrons and photons and sample their energy. It consists of a 4.77 m long barrel surrounding the TPC, along with end-caps which close it at both ends. Both the barrel and end-caps are made up of 12 modules, each covering 30 degrees in ϕ , which consist of 45 layers of lead sheets and wire chambers shown in Figure 3.12. The number of layers is justified by the total number of radiation lengths X_0 required⁵, which at LEP energies is provided by ~ 40 cm of lead corresponding to $\sim 22X_0$.

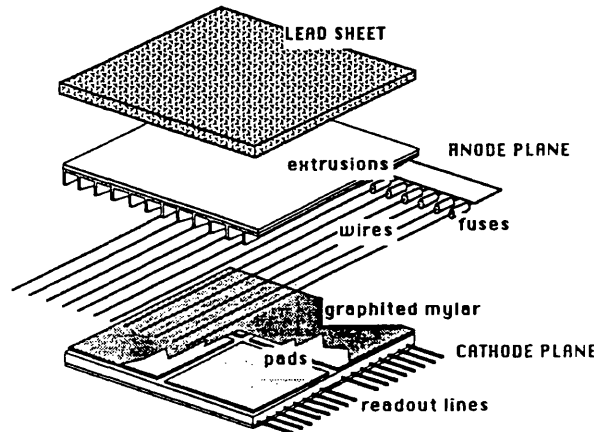


Figure 3.12: The components constituting an ECAL layer.

Electrons, positrons and photons penetrating the lead sheet will produce an electromagnetic (e.m.) shower of e^+e^- pairs which is sampled by the wire planes.

⁵One radiation length reduces the energy of a particle by a factor $1/e$.

Ionisation in the gas from these showers produce avalanches to the anode wires and these induce signals on small cathode pads. To obtain good spatial separation of e.m. showers for particle identification, the cathode pads are read out in projective towers pointing back towards the interaction point. This way a granularity of $0.9^\circ \times 0.9^\circ$ is achieved from $\sim 74\,000$ towers. The depth of ECAL is further segmented into three stories, corresponding to 4, 9, 9 X_0 , to allow e.m. shower identification by measuring the shower profile as it develops.

The energy resolution of Bhabha scattered electrons in ECAL has been parameterised as

$$\frac{\sigma(E)}{E} = \frac{0.18}{\sqrt{E(\text{GeV})}} + 0.009,$$

by comparing the measured ECAL energy with the track momentum or beam energy. In addition, the signal on the module wire planes is available as a trigger.

3.5.2 Hadronic Calorimeter and Muon Chambers

The hadronic calorimeter (**HCAL**) provides the main mechanical support for ALEPH, the return flux of the magnet and serves as a detector for hadrons and muons. Its structure is similar to that of the ECAL in that its barrel and end-caps are arranged in modules covering the full azimuthal angle. See Figure 3.13. The ECAL and HCAL calorimeters are however rotated with respect to each other, to avoid an overlap of the inactive ‘cracks’ between neighbouring modules (total inactive region of a few percent).

Although the calorimeters are similar in design, hadronic showers propagate through the iron via nuclear processes rather than the electromagnetic processes in ECAL. About half the incident hadron energy is passed on to additional fast secondaries, with the remainder being absorbed predominantly in the production of slow pions⁶. This has the overall effect of producing showers which are more spread out laterally and more penetrating, thus hadronic calorimeters must generally be deeper [55].

HCAL modules are constructed from 23 iron slabs separated by layers of plastic streamer tubes which constitute $\sim 7\lambda_0$. The active detector element is a graphite

⁶The longitudinal development of hadronic showers scales with the nuclear interaction length, λ_0 , and depends on the atomic number of the active material.

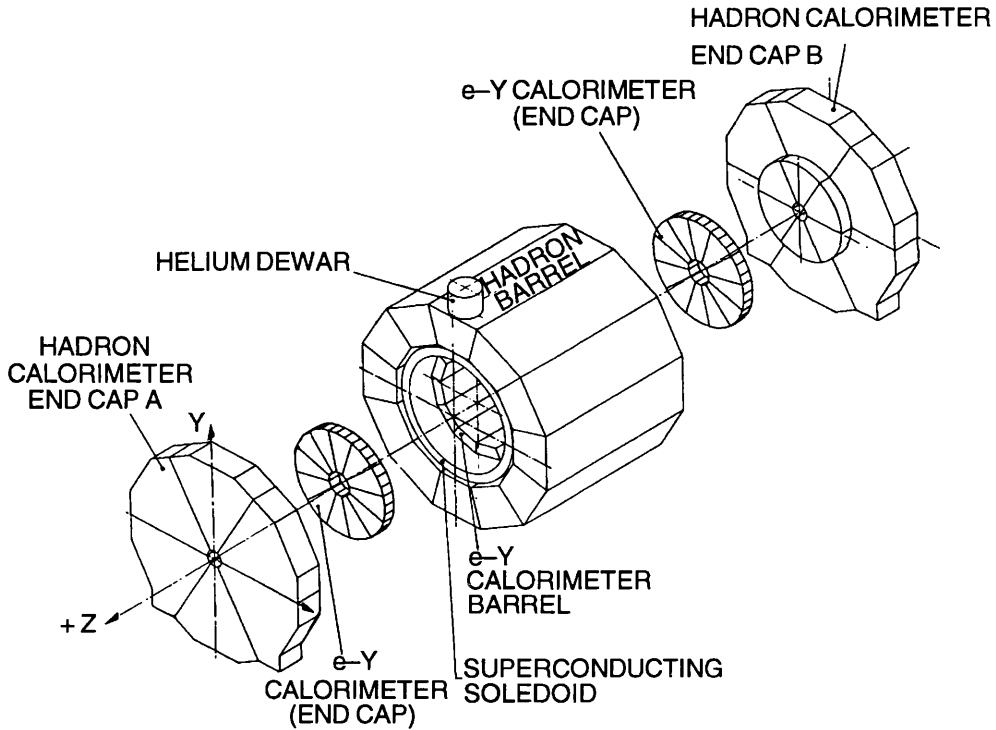


Figure 3.13: The hadronic calorimeter surrounding the magnet and electromagnetic calorimeter.

coated plastic tube containing eight wire counter cells. Each tube layer is read out with pad electrodes to give an integrated energy measurement and, with parallel digitizing strips, to reconstruct the shower structure⁷. As in the ECAL, the pads are connected to form projective readout towers pointing to the interaction point. The energy resolution obtained is

$$\frac{\sigma(E)}{E} = \frac{0.84}{\sqrt{E(\text{GeV})}},$$

parameterised using pions at $\theta = 90^\circ$.

Muons leave a characteristic signature in HCAL (and ECAL), distinguished by a single track with no shower development, making it important for muon identification. In addition, two further planes of streamer tubes situated outside the HCAL (the ‘muon chambers’) which serve as muon tracking detectors. Their relatively large separation (0.5m in the barrel) enable track segments to be measured with an accuracy of 10-15 mrad.

⁷A two-dimensional readout of the energy deposited is built from logical signals which say whether the cell is active or inactive.

3.5.3 Luminosity Monitors

Integrated luminosity is defined to be the ratio of the observed number of $e^+e^- \rightarrow e^+e^-$ interactions to their cross-section⁸ and its value is important for the calculation of observed cross-sections, e.g. for the Z^0 and W^+W^- lineshape scans. In addition to the main calorimetry described above, three additional, smaller calorimeters exist at low θ on both sides of ALEPH to measure the luminosity. They also monitor the general beam quality delivered to ALEPH by LEP, which is important for the safety of inner detector components.

- The Luminosity Calorimeter (**LCAL**) is a lead-wire sampling calorimeter which extends from 10 - 52 cm around the beam pipe and provides the primary luminosity measurement in ALEPH . It lies at a distance ± 2.62 m from the IP and, being similar to the ECAL in construction, attains approximately the same energy resolution but is sensitive from a lower polar angle of $\sim 2.6^\circ$. It measures the luminosity by counting the number of Bhabha events (symmetric back-to-back energy deposits observed) over the period that ALEPH is data-taking.
- The Solid-State Luminosity Calorimeter (**SiCAL**) was responsible for the luminosity measurement at LEP1 where it achieved a high precision since it extends to a polar angle as low as 1.4° . However, the increased background at LEP2 has necessitated low angle tungsten shielding to protect the central tracking detectors, which obscures part of this detector. Two such detectors are mounted on either side of the IP and consist of 12 tungsten sheets separated by active layers of silicon pads. These detectors now provide a larger angular acceptance in the ALEPH calorimetry.
- The Bhabha Calorimeter (**BCAL**) consists of two modules of 12 tungsten-scintillator layers, located ± 7.7 m from the IP. At this position the rate of Bhabha events is much higher than the LCAL and SiCAL receive, thereby allowing higher statistical precision on the luminosity measurement. However, it

⁸The theoretical cross section for $e^+e^- \rightarrow e^+e^-$ ('Bhabha') events is known to great accuracy.

sits just inside the final LEP focussing quadrupole magnet and needs to be calibrated with LCAL. It gives an instantaneous measurement of the luminosity in this region and also provides an online background monitor for ALEPH.

3.6 Data Flow and Event Reconstruction

3.6.1 Trigger

The e^+e^- bunch crossing rate in LEP is ~ 11 kHz, which is too high for ALEPH to record the result of every interaction. In any case, most of these are not genuine e^+e^- interactions, but the result of beam-gas interactions and off-momentum scatterings in collimators near the ALEPH IP. A trigger is required to reduce this background to a manageable level. In particular it has to reduce dead time in the data acquisition, make it acceptable for the TPC gate and minimise the amount of unwanted data recorded to tape. To realise these three criteria the signals from the individual ALEPH sub-detectors combine to build three corresponding logic stages, summarised in Table 3.2.

Stage	Decision time	Rate (Hz)	Information used
Level 1	$5 \mu\text{s}$	few 100	pad/wire readout from ECAL+HCAL hit patterns in ITC
Level 2	$50 \mu\text{s}$	10	TPC tracking
Level 3	62 ms	1-3	All subdetectors

Table 3.2: Summary of the ALEPH trigger system.

Level 1 makes a quick decision on whether or not to read out all detector elements. Once an event passes a Level 1 ‘YES’, the TPC gate is open and Level 2 checks that the charged trajectories originate close to the interaction point. If the Level 1 state cannot be confirmed the readout process is stopped and cleared for the next event. The Level 3 trigger acts on the complete detector readout of events passing levels 1 and 2. It is performed by an online analysis program which reduces the rate for practical data storage. The combination of these stages provide a highly efficient and flexible trigger which is sensitive to single particles and jets produced in e^+e^- interactions.

3.6.2 Data Acquisition

The ALEPH detector is highly modular in structure and the data acquisition is designed to complement this, linking the data from the sub-detectors individually to eventually record the entire event. Its hierarchical structure is shown in Figure 3.14.

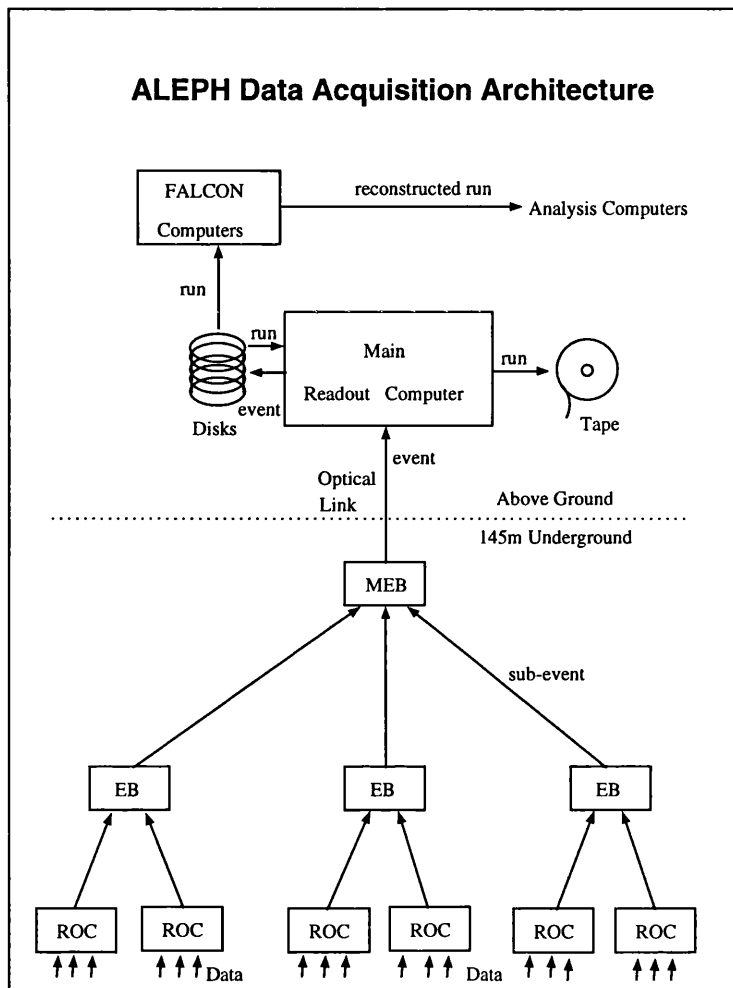


Figure 3.14: Simplified structure of the ALEPH data acquisition (DAQ) process.

The Main Trigger Supervisor (MTS) synchronises the readout electronics with the bunch crossing and communicates this to the readout controller's (ROC's) via their Trigger Signal Receiver (TSR). The ROC's initialise subdetector electronics and, on passing a Level 2 'YES', reads them out. Event Builders (EB's) then build the event at sub-detector level (subevent) to be fed into the Main Event Builder (MEB). The MEB combines and resynchronises all subevents before passing the

event to an online computer at the surface. The Level 3 trigger then performs a basic event selection before the accepted event is stored on disk by the Main Readout Computer. Immediately after a ‘run’ has finished⁹ it is written to tape, and the ‘Facility for ALepH COmputing and Networking’ (FALCON) fully reconstructs events by running the ALEPH program, JULIA [56]. This performs the track fitting mentioned in Section 3.4.4 and calorimeter reconstruction. Finally the events are stored in data files which provide the input for physics analyses using the ALPHA software package [57].

3.6.3 Energy flow

The energy flow reconstruction algorithm [41] builds a set of ‘objects’ from the hits and clusters in an event, characterised by their energies and momenta, for use in physics analyses. It uses the track momenta and photon, electron, hadron and muon identification capabilities of the calorimeters to improve the overall energy resolution. The first stage in the algorithm requires events to contain at least 4 hits in the TPC, or 8 if $p_{track} > 15 \text{ GeV}/c$, and tracks which originate in a cylinder ($\ell = 20 \text{ cm}$, $r=2 \text{ cm}$) around the interaction point. This latter selection will however reject tracks which are the result of a secondary decay vertex (so called V^0 decays, for example $\gamma \rightarrow e^+e^-$), which are cross checked by considering hits in the ITC. In addition, systematically noisy calorimeter channels are masked so as not to bias jet-clustering, and fake energy from occasional noise is removed if pad and wire signals in the calorimeters are incompatible.

After this stage charged tracks are extrapolated to the calorimeter clusters to form an energy flow subset called ‘calorimeter objects’. The energy associated with identified particles e , μ , γ , π^0 , is not included in the calorimeter objects, thus classifying the remaining particles as charged and neutral hadrons. The energies of the former are calculated as if they were pions and subtracted from the remaining calorimeter energy, and the energy remaining in HCAL is attributed to neutrals. Finally, the neutrino energies are inferred from the total missing energy in the event.

The energy flow algorithm thus produces a list of objects per event which are expected to be a good representation of the true particles, and allows the total energy

⁹A ‘run’ is the term used for two hours of data taking, or 600 Mega-bytes of data storage.

in the event to be measured with an accuracy of $\sim 7\%$. This is an improvement of $\sim 5\%$ over simply summing up all the raw energy found in the calorimeter cells with no particle identification. These objects are the starting point for the measurement described in this thesis.

3.7 Event Simulation

A central feature of the analysis in this thesis is the Monte Carlo simulation of the production and decay of W boson pairs through e^+e^- annihilation, from the fundamental physical processes involved to the fully reconstructed final state events. This is generally the case in experimental high energy physics, where a constant comparison of theory and experiment is exercised. Any discrepancy between data and Monte Carlo means that something has not been understood (in one and/or the other) and, overall, leads to a deeper understanding of the subject.

Monte Carlo simulation proceeds in three stages: Firstly the event kinematics are generated according to Standard Model production and decay processes using the KINGAL package [58]. The particular Monte Carlo generators used in this analysis to simulate the final state events will be described in more detail in the following section. The next stage is to simulate the response of the ALEPH detector to these events as they pass through it. This is performed using a GEANT [59] based program, GALEPH [60], which simulates the interactions of different particles in the various detector components¹⁰ and converts the ‘energy depositions’ into electrical signals. Finally the events can then be reconstructed with JULIA as if they were real, and hence are stored in exactly the same energy flow format. The only difference in the final simulated data is of course the information available at generator or ‘truth’ level, which is crucial for the optimisation of the W mass analysis presented here.

3.7.1 Monte Carlo Generators

The KORALW generator [61] was used to simulate the process $e^+e^- \rightarrow W^+W^-$ at different W mass values. This has the option of generating W^+W^- final states

¹⁰This includes *all* matter in the detector including the electronic response of the readout.

through the tree level (CC03) diagrams, or to include all 4-fermion (4f) diagrams, the latter being used predominantly. Below are listed the features of KORALW of importance to this analysis:

- Matrix element for W^+W^- production
- All decay channels into lepton and quark pairs
- QED effects in the initial state plus the Coulomb correction
- Arrangement of quarks from W decay into coloured strings
- Fragmentation to hadrons according to the LUND model [62]
- Massive kinematics with exact four-momentum conservation for the whole $e^+e^- \rightarrow W^+W^- \rightarrow 4f$ process [63]

Background from $e^+e^- \rightarrow q\bar{q}$ and $e^+e^- \rightarrow ZZ$ are simulated using the KORALZ [64] and PYTHIA [62] generators, respectively. Table 3.3 shows the Monte Carlo samples used for the analysis in this thesis.

Process	Cross-section (pb)	Generated events
Signal ($e^+e^- \rightarrow W^+W^-$)		
4f $M_W = 79.85 \text{ GeV}/c^2$	16.88	59998
4f $M_W = 80.35 \text{ GeV}/c^2$	16.926	307958
4f $M_W = 80.85 \text{ GeV}/c^2$	16.9599	59995
CC03 $M_W = 80.35 \text{ GeV}/c^2$	16.926	98746
Background		
$e^+e^- \rightarrow u\bar{u}$	20.299	120000
$e^+e^- \rightarrow d\bar{d}$	20.018	119999
$e^+e^- \rightarrow s\bar{s}$	20.055	120000
$e^+e^- \rightarrow c\bar{c}$	20.310	119999
$e^+e^- \rightarrow b\bar{b}$	19.604	120000
$e^+e^- \rightarrow ZZ$	2.7594	89997

Table 3.3: Number and type of Monte Carlo simulated events used in this analysis and their cross section at $\sqrt{s} = 189 \text{ GeV}$.

There are several additional Monte Carlo samples generated for the purpose of systematic error studies, which will be described in Chapter 5.

Chapter 4

Event Selection and Mass Reconstruction

The most direct way to extract the W mass is from the reconstruction of the W^+W^- decay products at energies above W^+W^- pair production threshold. At $\sqrt{s} = 189$ GeV, ALEPH collected an e^+e^- integrated luminosity of $\mathcal{L} = 174.2$ pb $^{-1}$, which corresponds to an *expected* number of W^+W^- events $N_{WW}^{exp} = \mathcal{L} \cdot \sigma_{WW} \simeq 2800$. Of these, 46.6% are expected to be fully hadronic W decays. Once a hadronic event has been selected there are several stages required to obtain the invariant mass distribution of the final state, from which the W mass can be extracted. A schematic hadronic event is illustrated in Figure 4.1 in terms of evolution from the point of initial W^+W^- pair production.

The final state consists of multiple hadron tracks and energy deposits. Assuming that these are the products of W^+W^- decay, the next stage is to associate them with their parent quarks to form jets (jet finding). Once this has been performed, the four reconstructed jet momenta are varied within their resolutions to make use of constraints from energy and momentum conservation. This kinematical fit improves the reconstructed mass resolution. Finally, a jet pairing procedure is applied to associate two di-jets to two W 's. Each of these reconstruction stages may introduce a bias in the final W mass measurement and a loss of purity in the sample. This chapter describes these stages in detail, with emphasis on the selection and jet finding algorithms. The last section details the final event samples in data and Monte Carlo which are subsequently used to extract the W mass in Chapter 5.

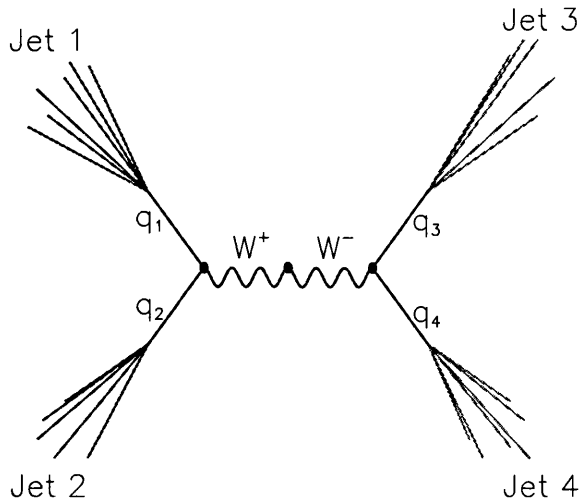


Figure 4.1: Schematic of a $e^+e^- \rightarrow W^+W^- \rightarrow q\bar{q}q\bar{q}$ final state, consisting of four jets from which the mass of the W propagator is reconstructed.

The analysis described in this thesis, which measures the W mass from data collected at $\sqrt{s} = 189$ GeV, has evolved from the optimisation of each analysis stage. Many of these studies have been made at previous LEP centre of mass energies¹, which is considered a valid approach since the topology of hadronic W^+W^- decays does not change dramatically once the LEP centre of mass energy is above the threshold for W^+W^- pair production (approximately 161 GeV).

4.1 Hadronic Event Selection

Hadronic W^+W^- decays are characterised by a high multiplicity, a four jet structure and low missing momentum (see Figure 4.2). Consequently they have a spherical topology and a total energy close to the centre of mass energy of LEP. At $\sqrt{s} = 189$ GeV, the background physical processes to the hadronic channel are:

$$\begin{aligned}
 e^+e^- &\rightarrow q\bar{q} \\
 e^+e^- &\rightarrow ZZ \\
 e^+e^- &\rightarrow W^+W^- \rightarrow q\bar{q} \ell\nu \\
 e^+e^- &\rightarrow Ze^+e^-
 \end{aligned}$$

¹LEP delivered a centre of mass energy of 172 and 183 GeV during 1996 and 1997, respectively.

$$e^+e^- \rightarrow W^+W^- \rightarrow l\nu l\nu,$$

in decreasing order of four jet final state cross section. By far the most dominant is the $q\bar{q}$ contamination, with a cross section of ~ 100 pb (c.f. $\sigma_{WW} \sim 17$ pb). Apart from the ZZ final state, the remaining processes have negligible cross section. The $e^+e^- \rightarrow Ze^+e^-$ process is not included in this analysis.

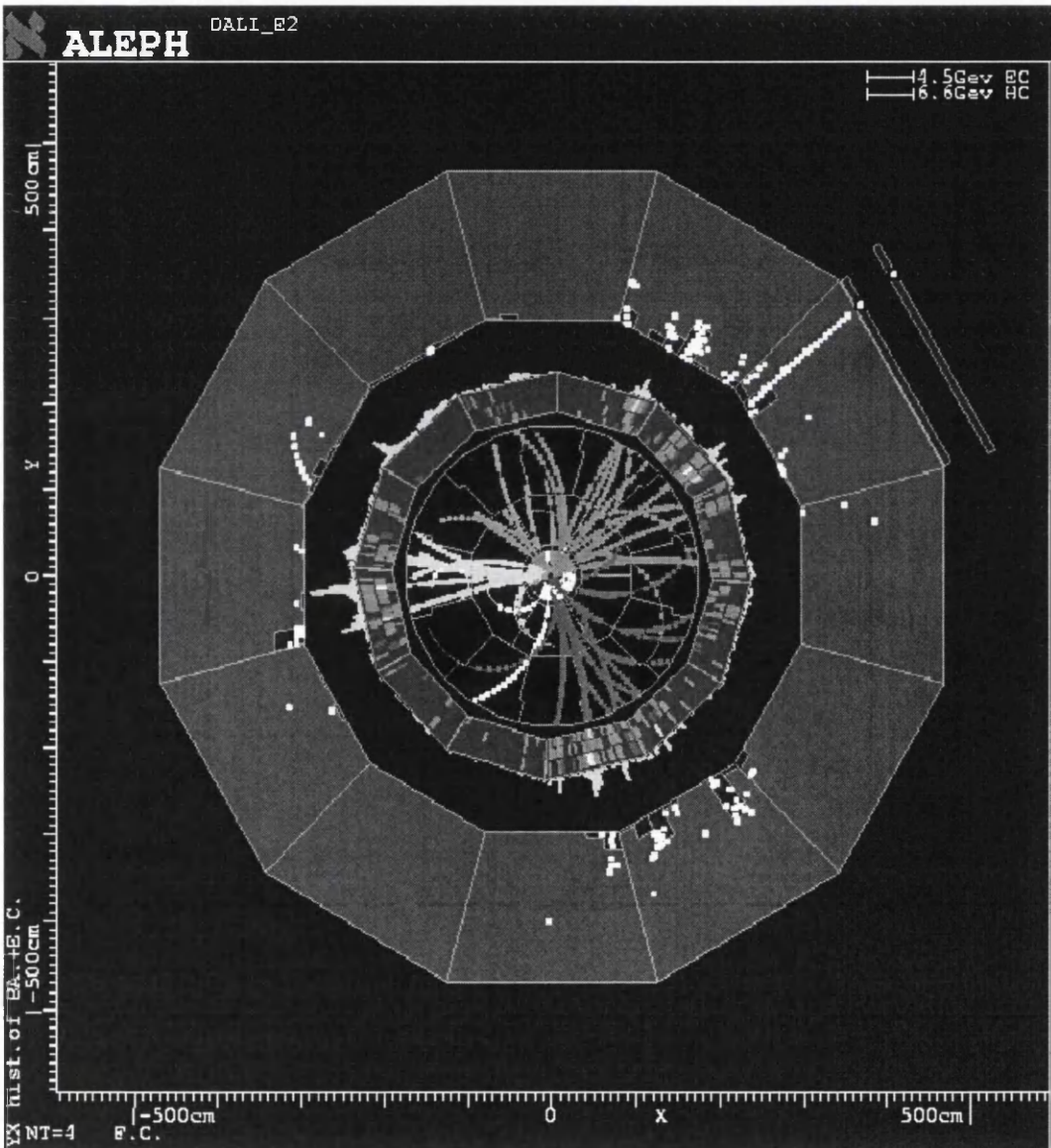


Figure 4.2: ALEPH event display showing a 4-jet event. Particle momenta are measured by the curvature of the tracks shown in the centre while their energies are shown as histograms in the calorimeters.

4.1.1 Optimising the Event Selection

The most efficient algorithms for selecting W^+W^- hadronic decays are based on a preselection stage, consisting of simple event variable cuts, followed by the construction of some dimensionless parameter which further discriminates signal from background. This, for example, can be a weight or probability built from multidimensional variable space or the output from a neural network. At $\sqrt{s} = 183$ GeV three different algorithms were studied to optimise the selection of fully hadronic W pair decays: ‘Weights’ [65], ‘Probability’ [66] and a 21 variable neural network ‘NN21’ [67]. The value and stability of the selection efficiency are the main criteria for comparison. A first step is to look at the dependence of the efficiency on the W mass, using MC’s generated with different input W masses, ranging from 79.25 to 81.25 GeV/ c^2 , as is shown in Figure 4.3.

All three show a mass dependence on their efficiency to select hadronic W decays. This causes a bias in the analysis, as higher masses are preferred to lower ones, hence a distortion exists in the mass distribution. Therefore the selection with the least mass dependence is favourable. The NN21 selection shows the least severe effect, moreover its overall efficiency is the highest of the three selections. A further important check is the stability of this mass dependence with the selection output cut. Figure 4.4 shows the gradient of the efficiency versus W mass, plotted as a function of selection output cut.

As can be seen the neural net is stable with the cut value, while the others are not, thus combined with its higher efficiency the neural network method was used for the ALEPH W mass analysis at $\sqrt{s} = 183$ and 189 GeV, rather than the weights or probability method.

4.1.2 Neural Networks

Neural networks (NN’s) are algorithms which find patterns in data, hence their use for event selection in particle physics. They are based on a number of simple interconnected processing elements called nodes and the processing ability of the network is stored in their connection strengths (weights) obtained by learning from a set of training patterns. The idea is to train the neural network using Monte Carlo

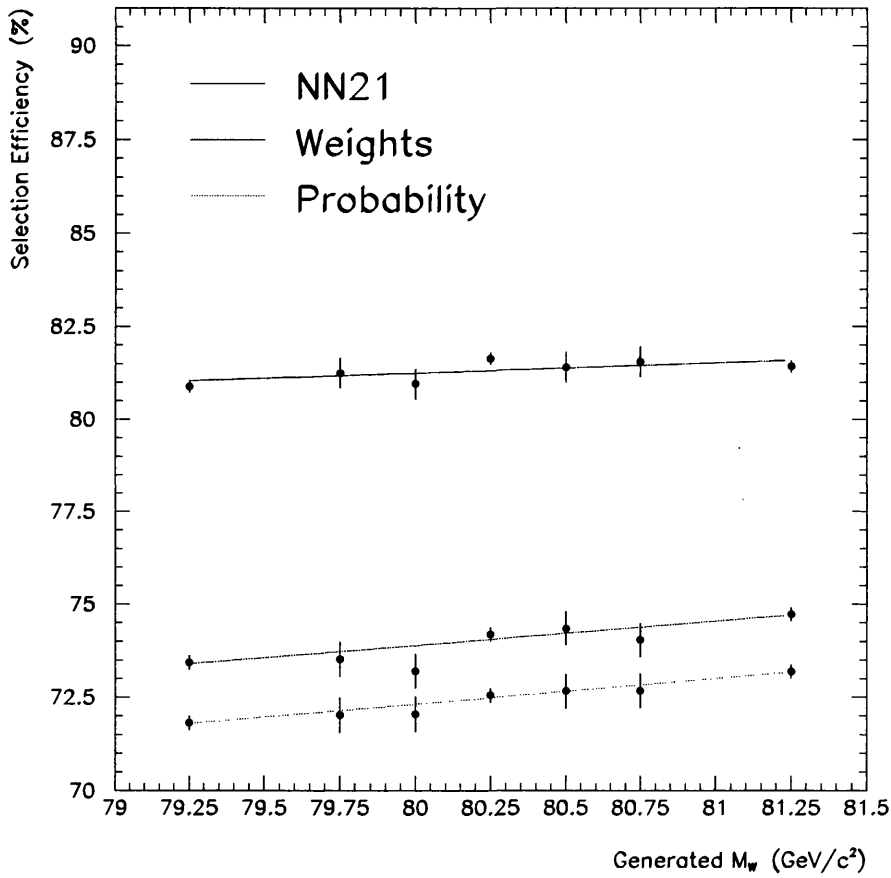


Figure 4.3: The mass dependence of the efficiency for three hadronic event selection algorithms studied at $\sqrt{s} = 183$ GeV. The NN21, weights and probability selections are shown by the top, middle and bottom points, respectively.

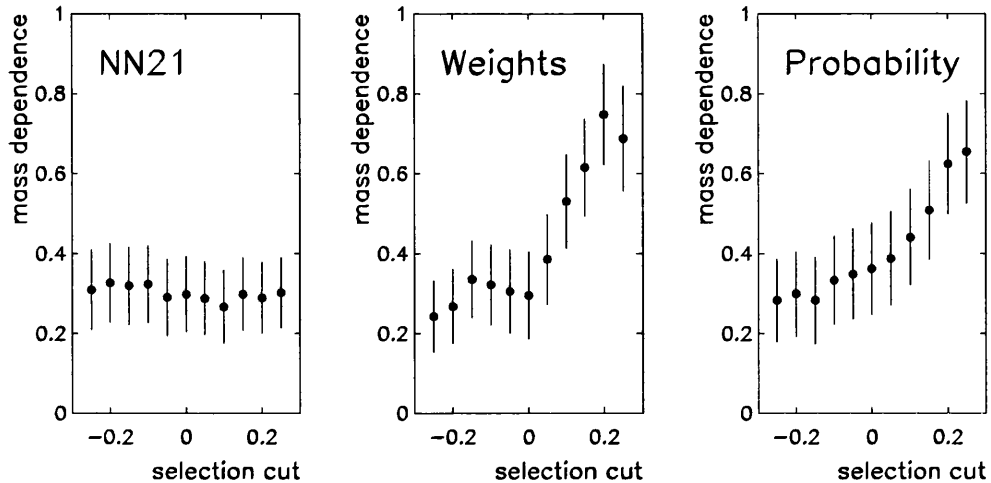


Figure 4.4: The mass dependence on the efficiency is defined as the gradient of the plot of efficiency versus W mass for each selection algorithm (at $\sqrt{s} = 183$ GeV). The zero corresponds to the ‘optimum’ cut value for that selection algorithm.

simulated $e^+e^- \rightarrow W^+W^- \rightarrow q\bar{q}q\bar{q}$ events and then to run over the real data to select hadronic W^+W^- decays. The variables used to build the event probability, on which a cut is made to identify hadronic events, are chosen in terms of their discriminating power. The number of variables in the NN is arbitrary and generally includes global event variables and variables describing the jet properties. For a mass measurement they must have minimal mass dependence as this could cause biases in the efficiency as discussed above. It is also important that the variables are well matched between data and MC, which means the minimum choice is favourable.

The neural network used in the analysis at $\sqrt{s} = 172$ GeV [68] used 21 variables, which were well matched in data and MC [67]. This agreement was checked further by looking at the correlations between the variables in both the data and MC, which should also be consistent. By considering the data/MC ratio of the 21×21 covariance matrices, discrepancies are clearly seen. The largest of these was found to be the correlation between the total charged multiplicity and the ‘number of objects in jet 1’² which had relative discrepancies of the order of 30 % [69]. The source

²The jets are ordered in energy from high (jet 1) to low (jet 4), defined by the jetfinding algorithm DURHAM-P, which will be described in detail in Section 4.2.1.

of this lies in the incorrect modelling of real physics processes in the MC, and in particular could be due to Colour Reconnection. This is a QCD effect (described in Section 2.5.1) for which most models predict a decrease in jet multiplicities that was not modelled in the Monte Carlo used. Other correlations which were not well matched were those involving the missing energy, which may be due to inadequate modelling of initial state radiation (this will be discussed in Section 5.6.3). This, along with results in the WW cross section measurement which showed that certain variables caused large biases, lead to the dropping of the two variables ‘total charged multiplicity’ and ‘number of objects in jet 1’. In addition, variables which were found to be highly correlated with the di-jet masses were replaced and the event selection was finally revised to ‘NN19’, used in the analysis at $\sqrt{s} = 183$ GeV [70].

4.1.3 Event selection at $\sqrt{s} = 189$ GeV

For the analysis at $\sqrt{s} = 189$ GeV a neural network event selection has been used with a better performance yet fewer variables (14) than at $\sqrt{s} = 183$ GeV. To remove as much background as possible the event must first pass the preselection by satisfying the following criteria:

- “CLASS 16”. This is a class of events which have ≥ 5 good tracks (‘good’ tracks must have at least 4 TPC hits and their reconstructed vertex must be physical), all of which must be within the detector acceptance and the total energy of all tracks must carry at least 10% of the LEP centre of mass energy.
- $|p_z| < 1.5(M_{vis} - M_Z)$, where M_{vis} is the total mass of all energy flow objects. This suppresses radiative returns³ to the Z .
- $y_{34} > 0.001$, where y_{34} is the y_{cut} value where four jets become three jets (this is described in detail in Section 4.2.1). This cut selects events with four jets.
- Maximum charged track energy fraction of a jet < 0.9 . This rejects semi-leptonic W^+W^- events, which are characterised by an high energy, isolated charged lepton.

³Approximately 50 % of $e^+e^- \rightarrow Z/\gamma \rightarrow q\bar{q}$ events are affected by initial state radiation, which reduces the $q\bar{q}$ centre of mass energy to the Z mass.

- Maximum electromagnetic energy fraction in a 1° cone around any particle < 0.95 . This cut eliminates events which have ISR contained within the detector acceptance.

Events which pass this preselection are then characterised by the response of a 14 variable neural network ‘NN14’ [71]. As in previous NN’s these variables, listed in Table 4.1, have been chosen for their discriminating power and minimum di-jet mass bias to give maximum efficiency. It is not straight forward to characterise these variables in terms of their discriminating power due to the strong correlations among them.

Global Variables	1	Thrust†
	2	Sphericity†
	3	Missing energy
Jet Properties	4	Max. e.m. energy fraction of a jet in any 1° cone
	5	Max. charged track energy fraction of a jet
	6	Charged multiplicity of lowest energy jet
W^+W^- Kinematics	7	Sum of 4 smallest di-jet angles
	8	Angle between 2nd and 3rd jets
	9	Maximum jet energy
	10	2nd minimum jet energy
	11	Minimum jet energy
	12	2nd minimum jet mass
	13	Minimum jet mass
Flavour Tagging	14	b-tag event probability

Table 4.1: The physical variables used as input to the neural network to discriminate signal from background. † refers the reader to Appendix A for a definition. Their numbers correspond to their appearance in Figures 4.5- 4.7.

The NN14 is trained on a large sample of $100,000 W^+W^-$ and a similar number of $q\bar{q}$ and ZZ events to recognise hadronic W^+W^- decays, thereby discriminating against background. The agreement between data and MC in these variables is shown in Figures 4.5 - 4.7, for events which pass the preselection only. Checking this agreement after the actual cut on the NN output would bias the results since the NN14 was trained on signal events. The effect of the preselection cuts can clearly be seen in variables 4 and 5. The agreement between data and MC is generally good, within the limited data statistics. Relatively large discrepancies are seen for lower

values of sphericity, variable 2, where the MC predicts more events than are found in data.

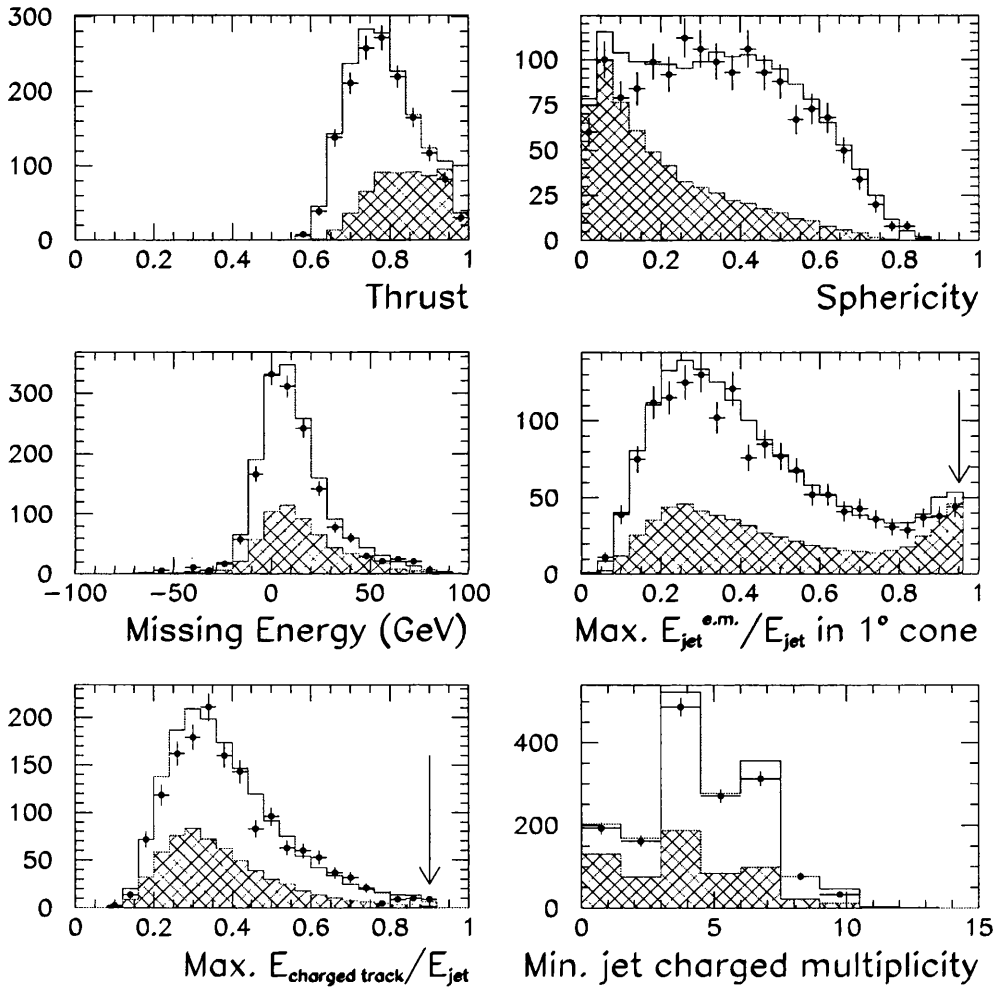


Figure 4.5: NN variables 1-6, used to discriminate between signal and background using a neural network. The vertical arrows show the effect of a preselection cut in that variable (variables 4 and 5). The empty histogram represents MC (signal+background), normalised to the observed number of events. The solid histogram represents the $q\bar{q}$ and ZZ background and the data collected at $\sqrt{s} = 189$ GeV are shown by the points.

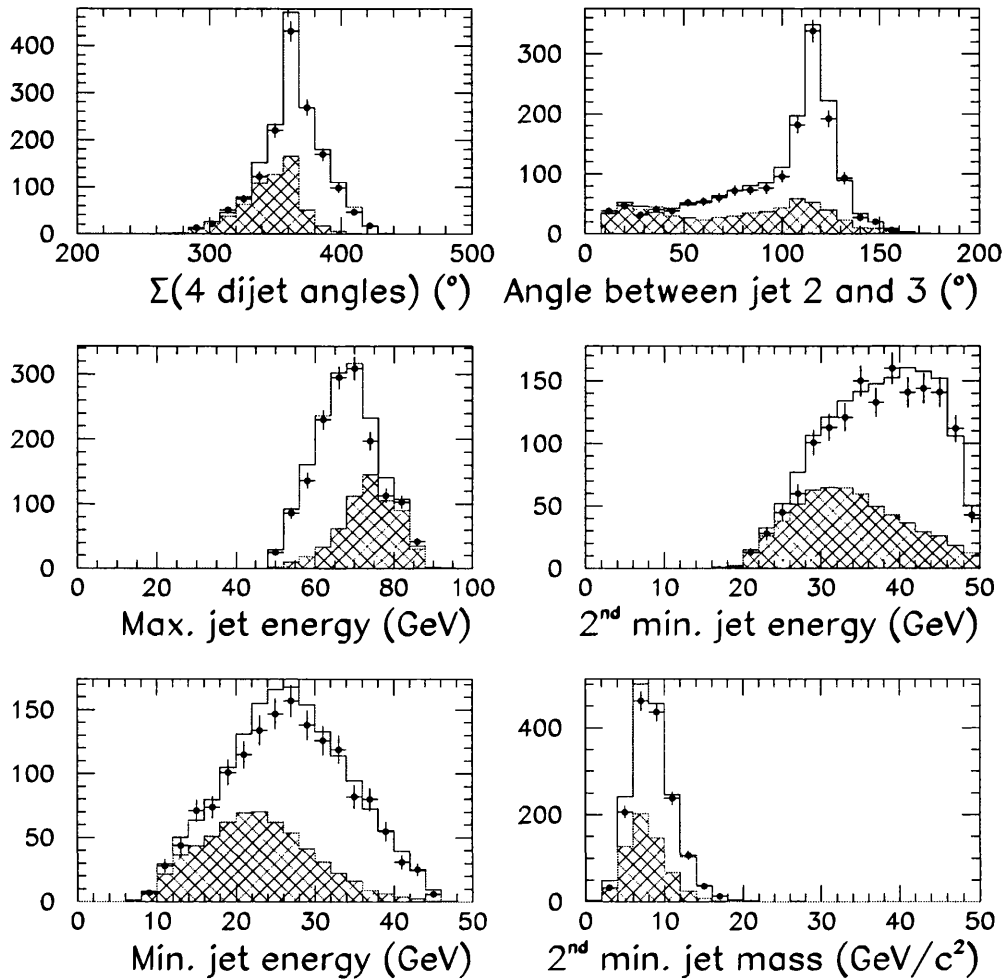


Figure 4.6: NN variables 7-12, used to discriminate between signal and background using a neural network. The empty histogram represents MC (signal+background), normalised to the observed number of events. The solid histogram represents the $q\bar{q}$ and ZZ background and the data collected at $\sqrt{s} = 189 \text{ GeV}$ are shown by the points.

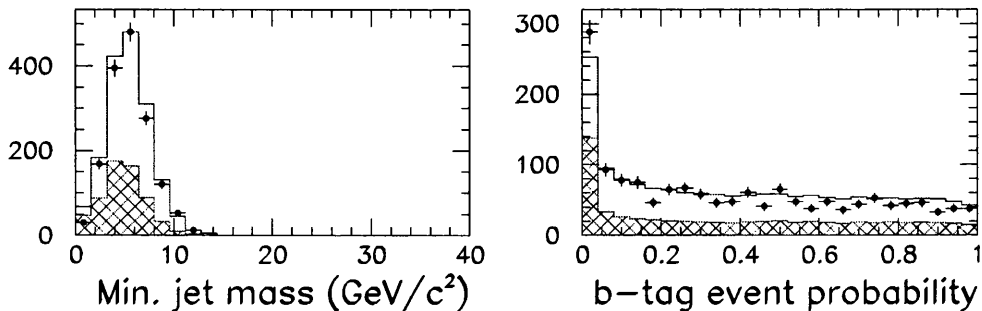


Figure 4.7: NN variables 13 and 14, used to discriminate between signal and background using a neural network. The empty histogram represents MC (signal+background), normalised to the observed number of events. The solid histogram represents the $q\bar{q}$ and ZZ background and the data collected at $\sqrt{s} = 189$ GeV are shown by the points.

The correlation between two variables x_i, x_j is expressed with the dimensionless correlation coefficient $\rho \in [-1, 1]$, calculated from:

$$\rho_{x_i, x_j} = \frac{V_{x_i, x_j}}{\sigma_{x_i} \sigma_{x_j}} = \frac{\overline{x_i x_j} - \overline{x_i} \overline{x_j}}{\sqrt{(\overline{x_i^2} - \overline{x_i}^2)(\overline{x_j^2} - \overline{x_j}^2)}},$$

with a statistical error for large N approximated by [72]:

$$\delta\rho = \frac{1}{N}(1 - \rho^2).$$

The correlation coefficients for each variable with all other variables are shown in Figures 4.8 and 4.9 in Monte Carlo (the errors on the correlation coefficients are therefore negligible). The difference in the correlation coefficients between all 14 neural network variables in data and Monte Carlo is shown in Figures 4.10 and 4.11. The correlations are generally well matched in data and MC. The largest discrepancies are found when the correlation between two variables is high. This can be seen as a spread in the di-jet angular variable number 8, as this is highly correlated with the jet properties. The variables used in the neural network should therefore be chosen partially for their small correlation. The correlation between thrust and sphericity has the largest discrepancy of about 5 sigma.

The output of the neural network is a number between 0 and 1; the closer to 1 the more ‘ W^+W^- like’ the event. The optimum cut value is found by studying the

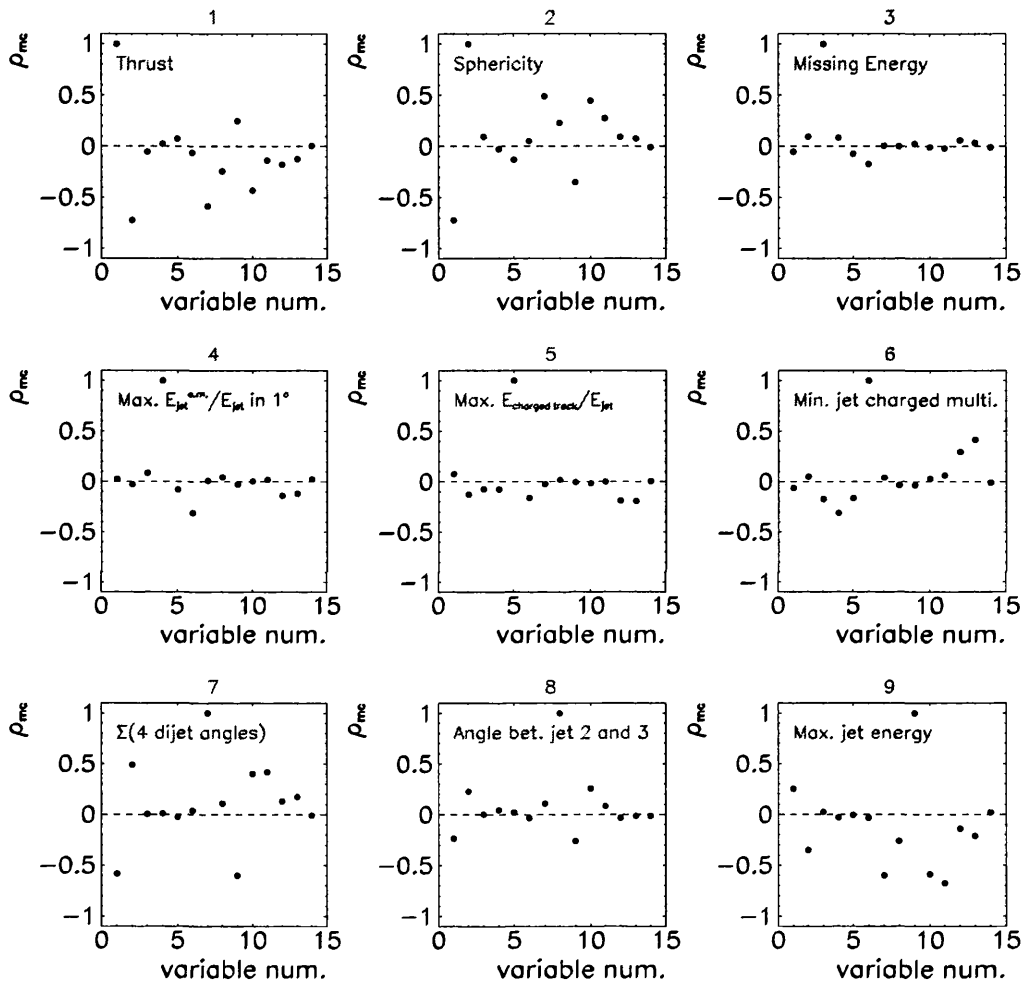


Figure 4.8: The correlation coefficients in MC for NN variables 1-9. Each variable is shown with its correlations with all other variables, hence $\rho = 1$ for correlations of a variable with itself.

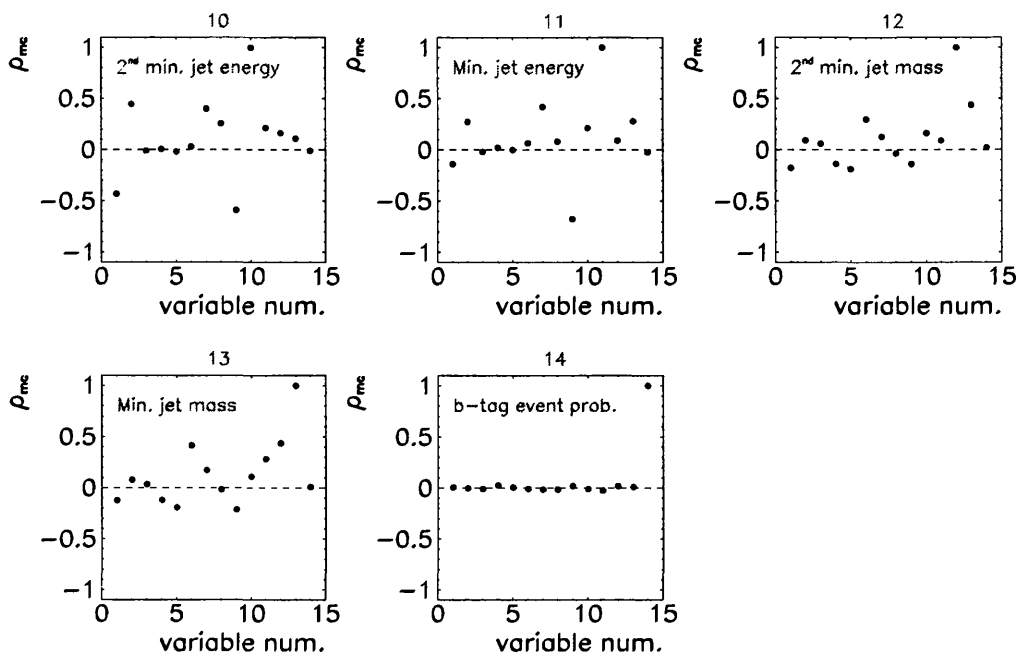


Figure 4.9: The correlation coefficients in MC for NN variables 10-14. Each variable is shown with its correlations with all other variables, hence $\rho = 1$ for correlations of a variable with itself.

distribution of the NN output for signal and background MC. These are shown in Figure 4.12, along with the real data signal. In addition, it is important to optimise the cut value in terms of the selection efficiency and purity, which should both be as high as possible. This is shown in Figure 4.13.

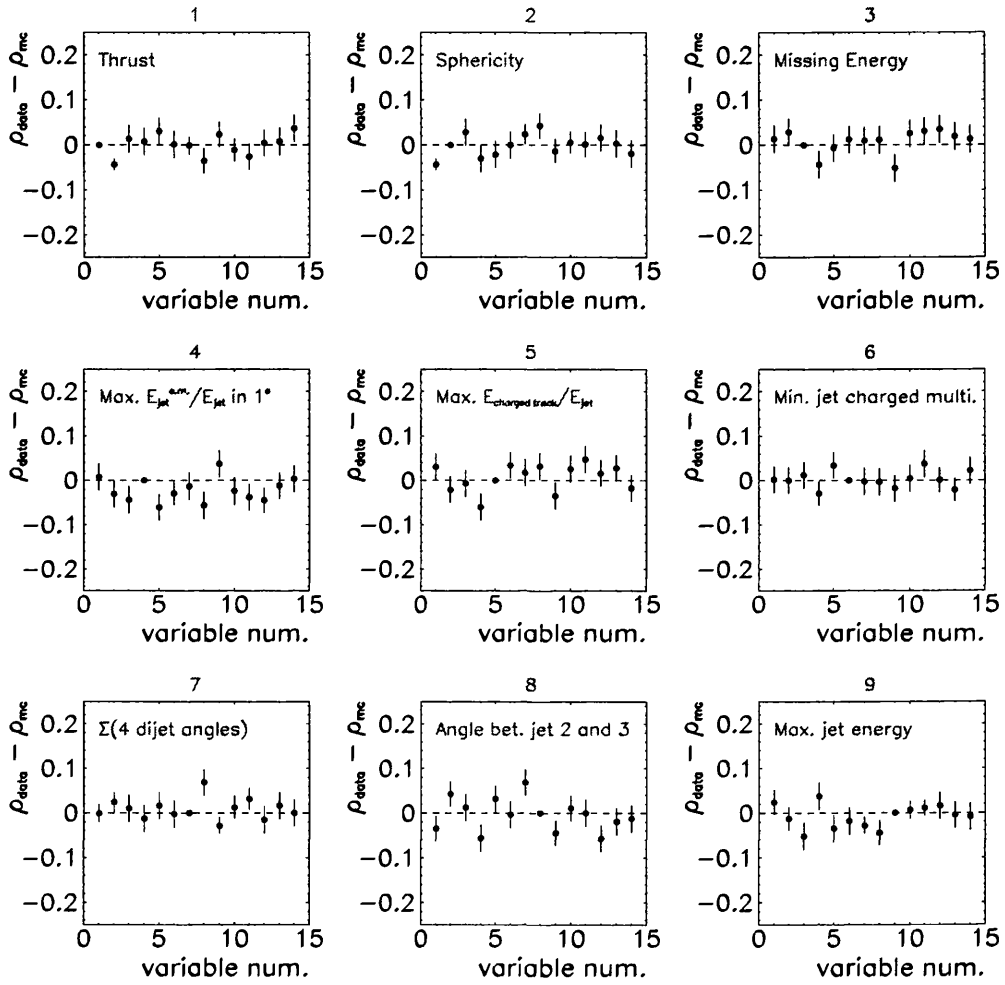


Figure 4.10: The difference in correlation coefficient between data and MC for NN variables 1-9. Each variable is shown with its correlations with all other variables, hence the difference in ρ is zero for correlations of a variable with itself.

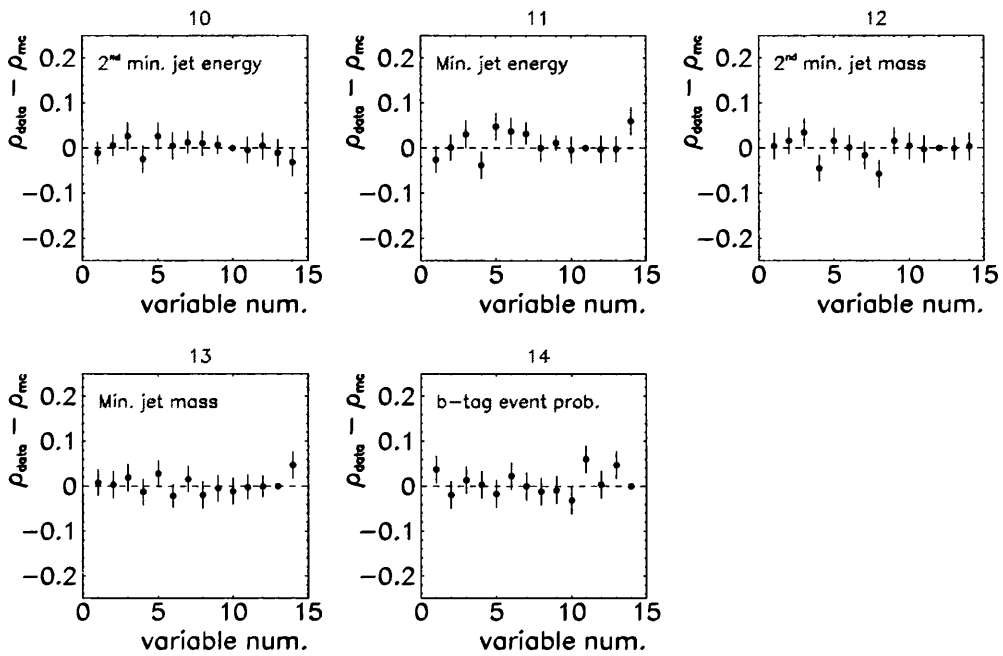


Figure 4.11: The difference in correlation coefficient between data and MC for NN variables 10-14. Each variable is shown with its correlations with all other variables, hence the difference in ρ is zero for correlations of a variable with itself.

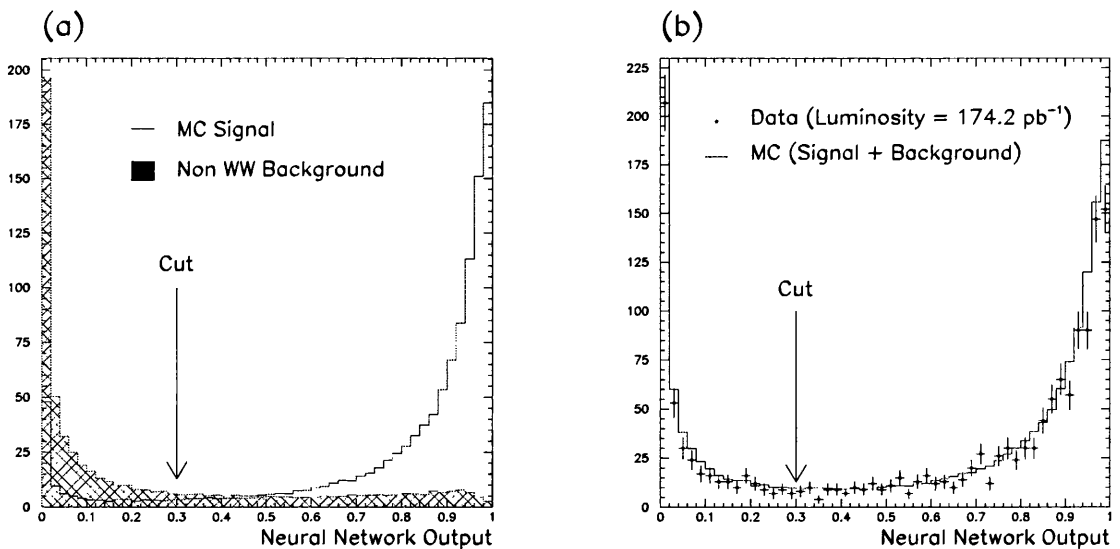


Figure 4.12: The output of the neural network. The cut is made at 0.3, which gives good efficiency and purity of the selected sample (a). The agreement of the neural network output between data and MC (signal + background) is shown in (b).

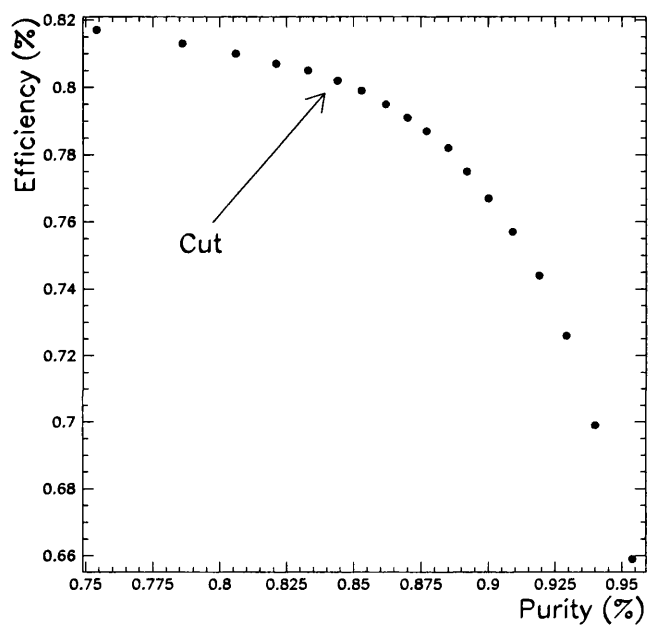


Figure 4.13: Signal efficiency versus purity for different values of the neural network output cut (cut value increases from left to right). The arrow indicates the 'optimal' value used, 0.3.

4.2 Jet Finding

The reconstruction of the quark system can be a major source of bias in the hadronic channel and one which is particularly difficult to eliminate. This is due to associating hadrons to incorrect jets, thus sometimes the wrong parent W 's, causing particle mixing between jets. Jet finding, or clustering, is therefore an important stage in the reconstruction procedure and there are many different algorithms which perform this.

4.2.1 Clustering Algorithms

The general clustering procedure is to calculate some 'distance parameter', y_{ij} , between each reconstructed object in the detector and combine the pair of objects which minimises it into a pseudo-particle⁴. This step is then iterated, treating the particles and pseudo-particles on the same footing, until $y_{ij} > y_{cut}$ for all remaining objects. At this point the remaining pseudo-particles are considered to be jets. The distance parameter may be defined in several ways using the track energies and momenta, but is normally some mass variable, M_{ij}^2 , scaled by the visible energy in the detector,

$$y_{ij} = \frac{M_{ij}^2}{E_{vis}^2}. \quad (4.1)$$

Thus in each event, any reasonable number of jets can be found by setting a different value of y_{cut} . Alternatively, the reverse approach may be taken, where the event is forced into a particular number of jets by stopping the clustering iterations when the desired number of jets is reached. This is the method adopted in this analysis, since only four-jet events are of interest⁵. Several versions of these algorithms exist, differing in their definition of M_{ij}^2 . These are shown in Table 4.2.

In the original jet finding algorithm, proposed by JADE, the mass variable is the invariant mass of the track pair, assuming $m_i = m_j = 0$. This means that JADE will cluster two soft (low energy) particles together even if they are at a large angle. This can result in the algorithm not being sensitive to extra gluon jets⁶,

⁴This is the result of adding the 4-momenta of two particles to form one object.

⁵Recent advances in the analysis consider potential improvement by allowing for the possibility that events may contain 5-jets.

⁶The quark may radiate a gluon, in analogy with the radiation of a photon by an electron, which subsequently fragments into hadrons.

Version	Mass Variable, M_{ij}^2
JADE	$2E_i E_j (1 - \cos \theta_{ij})$
DURHAM	$2 \min\{E_i^2, E_j^2\} (1 - \cos \theta_{ij})$
GENEVA	$\frac{8}{9} E_i E_j (1 - \cos \theta_{ij}) / (E_i + E_j)$
MASS	$(p_i + p_j)^2$

Table 4.2: The definition of M_{ij}^2 for different jet finding algorithms.

which tend to be softer than quark jets. The DURHAM algorithm was introduced to improve on this. It can be interpreted as evaluating the transverse momentum of the softer particle with respect to the harder one, which makes it sensitive to soft gluon radiation. GENEVA is similar to DURHAM in this respect and was developed for the measurement of α_s , the strong coupling constant. The MASS algorithm uses the massive form of the JADE mass variable.

In addition, each version is implemented with one of three schemes, which define the way in which the jet 4-momenta are calculated from the individual particles in each jet. The different schemes are shown in Table 4.3.

Scheme	Calculation of track 4 momenta
E SCHEME	$E_{ij} = E_i + E_j, \quad p_{ij} = p_i + p_j$
P SCHEME	$E_{ij} = p_{ij} , \quad p_{ij} = p_i + p_j$
E0 SCHEME	$E_{ij} = E_i + E_j, \quad p_{ij} = E_{ij}(p_i + p_j) / p_i + p_j $

Table 4.3: The different schemes available to each jet finding algorithm.

The P and E0 schemes calculate the new cluster 4-momenta so as to form massless jets, in contrast to the E scheme which simply sums the 4-vector components, hence retaining the jet masses. The combining process has less influence on the structure of the jets and subsequently the choice of combination scheme is less critical than the clustering method. DURHAM PE is a variation of the DURHAM algorithm which clusters the particles as if they were massless (P scheme) but combines the particles in the jet to form massive jets via the E scheme. The idea behind using the P scheme first is to reduce particle mixing between jets, one of the main sources of error in jet finding [73], because it performs this more effectively than the E scheme alone.

It is thought [62] (pp.278) that the method adopted by these algorithms is not optimal, as there is no possibility of reassigning particles to different jets at the end of the clustering procedure. Two further algorithms have been developed to incorporate this step, based on considerations of the particles' transverse momenta, p_T .

PTCLUS [74] first forms pre-clusters around the most energetic tracks, then clusters all the particles with a squared transverse momentum greater than 0.25 (GeV/c)^2 with respect to this. This is repeated until all tracks have been assigned to a cluster. In the second step, pre-clusters are combined into jets according to a scheme and version, as above, and finally particles are reassigned to jets so as to minimise their p_T with respect to each jet.

LUCLUS [75] defines a jet as a collection of particles which have limited p_T with respect to a common jet axis, and hence also with respect to each other. The distance

$$d_{ij} \approx \frac{|p_i \times p_j|}{|p_i + p_j|},$$

in the limit of small angles, has the simple physical interpretation of the transverse momentum of either particle with respect to the direction given by the sum of the two particle momenta. Track pairs which minimise d_{ij} are combined until the required number of jets is reached. Particles are then swapped among jets to ensure that all particles in the event are reassigned to the closest of the clusters. LUCLUS is similar to DURHAM, but allows particle-jet reassignment.

4.2.2 Optimisation

The analysis to obtain a W mass from a final state of four jets relies upon the jet algorithm to reconstruct the jets as accurately as possible. To this end, a study was made of these jet finding algorithms with a view to optimising the resolution on the W mass measurement. This was performed by constructing a simple Monte Carlo analysis chain which follows the basic steps described at the beginning of this chapter and then running it with different jet finders to see the effect on the reconstructed invariant mass distribution.

Using a MC sample of 100 000 WW events, generated at a centre of mass energy of 172 GeV and at a mass $M_W^{\text{ref}} = 80.25 \text{ GeV/c}^2$, 46361 fully hadronic events were

selected using the truth level information in the MC sample. All other channels were rejected and physics background has not been included in this study. The kinematic fit was performed by a package QFITWW [76], which imposes overall 4-momentum conservation along with an additional approximate⁷ W^+W^- equal mass constraint. Finally the fitted jets were paired using an ‘Asymmetry’ method [77], which uses MC truth information to determine which di-jet contains the W^+ and W^- daughters. Mass, energy and angular distributions for the reconstructed W^\pm were taken to be those of the two correctly paired di-jets. Using the reconstructed and true W masses per event, the shift in the W mass could be calculated. For comparison of the bias caused by each jet finder, the mass shift is displayed in Figure 4.14. It is immediately clear from the relative mass shifts that jet finding has an effect on the final W mass distribution. However, before any further conclusion is drawn from this plot, it should be stated that these mass shifts from the zero line are not necessarily solely the effect of the jet finder. Each stage in the analysis (jet pairing, kinematic fitting etc.) might induce a mass shift. If the analysis were repeated with different kinematic fitting, for example, the zero line on the plot may shift from the value shown. In addition there are biases within the particular MC used. For example, within a MC sample there is a certain parameterisation of the hadronisation process (where the initial partons fragment into jets) which is an approximation controlled by various fragmentation parameters. This has an effect on the jet finding, which essentially runs the hadronisation process in reverse.

The mass shifts shown in Figure 4.14 have resulted from a particular analysis chain in which all stages other than jet finding have been kept the same. The dominant effect in producing the relative mass shifts is that caused by the jet finder, but there are contributions from the other analysis stages. In addition, the different stages in the analysis are not completely independent. For example, if a pairing algorithm uses di-jet masses, it will also depend on jet finding. These interactions between analysis stages produce a second order contribution to the mass shift, although they are likely to be small by comparison to the effect of the different jetfinders. It is therefore important to realise that this plot applies only to

⁷The W has a finite width, which in the Standard Model is $\Gamma_W = 2.07 \text{ GeV}$ for $M_W = 80.25 \text{ GeV}/c^2$.

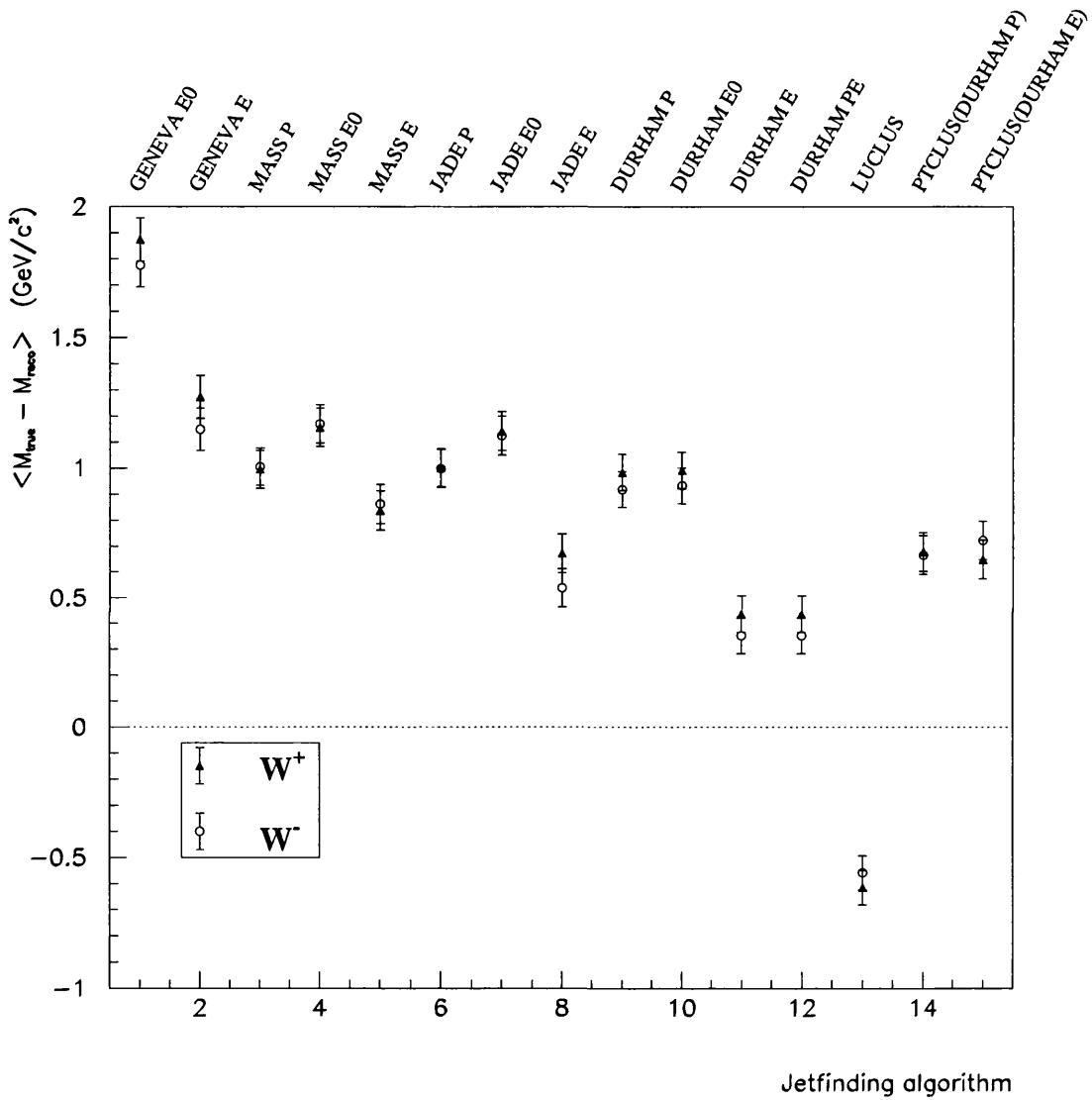


Figure 4.14: The mean value of the quantity $M_{\text{true}} - M_{\text{reco}}$ (the shift in the reconstructed invariant mass distribution) obtained from running the analysis using different jet finding algorithms.

this particular analysis chain, and that to reach a more general conclusion on the performance of jet finders requires an understanding of all the mass shifts induced by each stage, and the effect of their interaction.

Within this constraint, jet finding algorithms produce a lower mass shift when implemented via the E scheme. This is expected, since this is the only scheme which incorporates massive jet four momenta. The DURHAM E and PE algorithms produce the smallest mass shift in the reconstructed W. To determine which algorithm produces the best resolution on the final mass, the RMS of the mass distributions have been considered. These are shown in Figure 4.15 for each jet finder. The re-

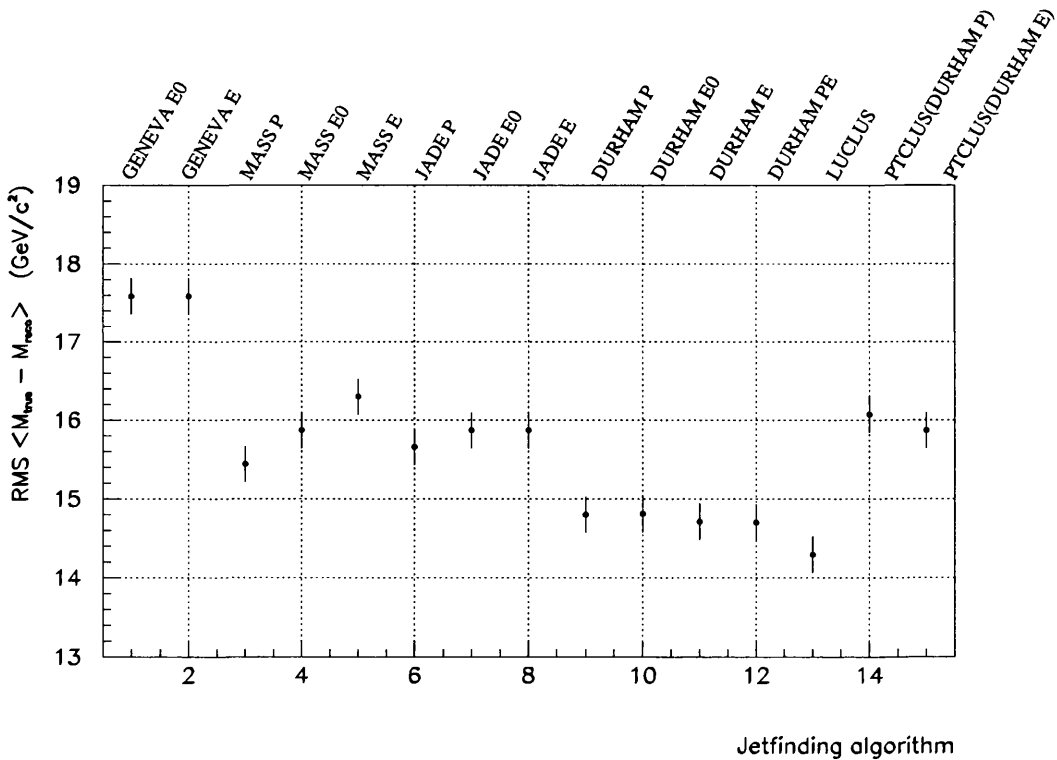


Figure 4.15: The RMS of the mass shift distributions. The RMS values for the W^+ and W^- are the same within the statistics used.

sults follow roughly the same pattern as the mass *shifts* shown in Figure 4.14, which is expected. The DURHAM algorithm consistently produces some of the best mass resolutions, although LUCLUS performs equally well. However, no distinction can be made between them within the statistical error. From these results it was decided to choose the DURHAM PE algorithm for the W mass analysis. LUCLUS was not

favoured, as its RMS is not significantly lower than those of DURHAM and moreover, the distance measure it uses is based strongly on a particular hadronisation model.

4.3 Kinematical Fit

The fact that jet 4-momenta are reconstructed from the final state hadron tracks observed in the detector, where overall 4-momentum conservation of the event and other physical information have not been exploited, results in a broadening of the invariant mass distribution. A four-constraint (4C) kinematic fit uses precise knowledge of the LEP beam energy to constrain each event with energy and momentum conservation, thereby improving the jet resolution.

Within the kinematic fit three parameters, denoted a_i, b_i, c_i , transform the measured jet momenta \mathbf{p}_i^{meas} to the corrected one \mathbf{p}_i^{corr} , such that

$$\mathbf{p}_i^{corr} = a_i \mathbf{p}_i^{meas} + b_i \mathbf{u}_i^\theta + c_i \mathbf{u}_i^\phi,$$

where \mathbf{u}_i are unit vectors. \mathbf{u}_i^θ is in the plane defined by the measured jet axis and the z axis and is perpendicular to \mathbf{p}_i^{meas} . \mathbf{u}_i^ϕ is perpendicular to both \mathbf{u}_i^θ and \mathbf{p}_i^{meas} . The coefficient a_i is an energy correction while b_i and c_i describe angular corrections. These are determined from MC and defined such that their spread from the average values, determined for each bin of jet energy and polar angle θ , are Gaussian with small correlation. The fit allows all measured values to vary around their means and within their R.M.S.'s in order to fulfill the following constraints:

$$\sum_{i=1}^4 E_i = 2E_{beam} \quad \text{and} \quad \sum_{i=1}^4 \mathbf{p}_i = 0.$$

A χ^2 is constructed from the fit parameters and the constraints are imposed by Lagrange multipliers. This is then minimised using an iterative procedure and for all events the fit converges successfully [70].

The discrepancy between a_i in the data and MC is dealt with by a parameterisation as a function of $\cos\theta$. This is shown in Figure 4.16, where it can be seen that the main corrections are in the overlap region between the calorimeter barrel and end caps, and in the region in close proximity to the beam axis.

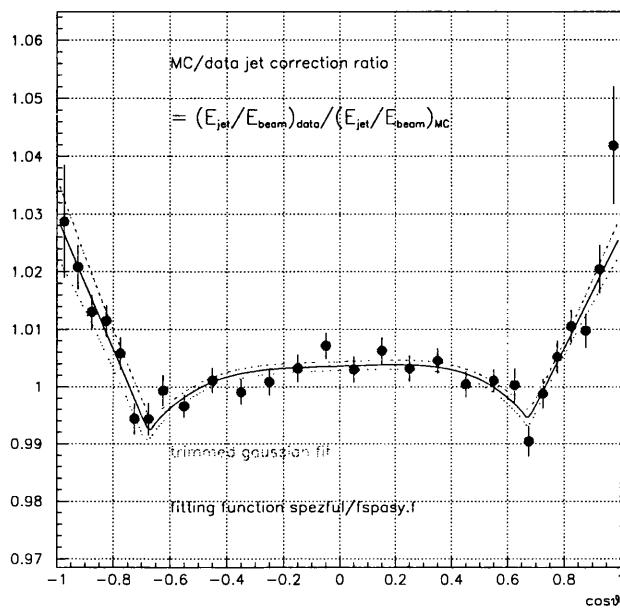


Figure 4.16: Average corrections applied to measured jet momenta before the kinematic fit. The largest corrections are in the overlap region between the detector barrel and end caps ($|\cos\theta| \sim 0.7$), and close to the beam axis ($|\cos\theta| > 0.9$).

The 4C kinematic fit gives rise to two masses per event, corresponding to the two candidate W bosons. A further gain in mass resolution can be obtained by scaling the fitted masses m_{ij} by the ratio of the beam energy E_{beam} and the jet energies E_i and E_j . The rescaled masses,

$$m_{ij}^{resc} = m_{ij} \frac{E_{beam}}{E_i + E_j},$$

are not in themselves better estimators of the di-jet masses, but combined add more information through their dependence on the W velocities. An analytical explanation of the source of this gain [78] is given in Appendix B. The improvement in the di-jet mass resolution from the kinematic fit is shown in Figure 4.17. The 4C + rescaling fit gives the best resolution on the mass and is the method used in the analysis at $\sqrt{s} = 189$ GeV .

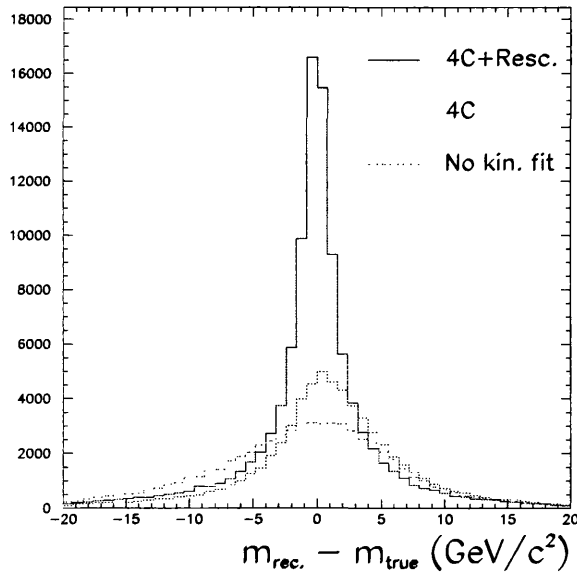


Figure 4.17: The mass resolution when using no kinematical fit and the improvement when forcing energy and momentum conservation (4C fit). A 4C fit plus rescaling with the beam energy gives the best mass resolution at $\sqrt{s} = 189$ GeV.

The kinematic fit produces a 2×2 covariance matrix for each event, which allows the possibility of weighting each event by dividing m_1 and m_2 by their respective errors. Since events which are badly reconstructed should have a larger error, they

should have a lower weight in the invariant mass distribution, thereby improving the mass resolution further. However, in order to apply the event-by-event errors to the invariant mass distribution, their origin and behaviour must be understood.

4.4 Jet Pairing

At this stage in the analysis, there are four kinematically fitted jets per event, two from each W decay. The next step is determining which jet pair came from which W boson. There are three possible ways to form two di-jet systems in a four jet event. An algorithm is required to select the correct combination, using kinematic information. The simplest method is to choose the di-jet combination which has the smallest mass difference (since the correct pair came from a W^+W^- decay), and then class the di-jets in terms of their opening angle (since near threshold the W bosons decay almost back-to-back). This was the method adopted in the analysis at $\sqrt{s} = 183$ GeV [70] and for the preliminary W mass measurement at $\sqrt{s} = 189$ GeV [79].

It has been found that a method using the $e^+e^- \rightarrow 4f$ matrix element gives a better efficiency and an improvement in the statistical error on the W mass measurement [80]. This algorithm calculates the CC03 matrix element \mathcal{M} for each of the three di-jet combinations and the correct one is taken to be the one with the largest value of \mathcal{M} (i.e. the highest probability that it came from a W^+W^- pair decay). The effect of this algorithm is shown in Figure 4.18, where the 1st, 2nd and 3rd combinations are ordered by their value of \mathcal{M} .

The three di-jet combinations are also ranked in order of their opening angles, as before. If the selected combination (i.e. largest value of \mathcal{M}) has the smallest opening angle, then it is replaced by the combination with the second largest value of \mathcal{M} . The combination with the smallest value of \mathcal{M} is never reconsidered. Both masses for the selected combination must lie within the mass window 60-86 GeV/ c^2 and at least one of the two masses must be between 74 and 86 GeV/ c^2 . If this mass window condition fails, then the combination with the second largest value of \mathcal{M} is accepted instead, provided its two masses satisfy the window criteria; otherwise the event is rejected.

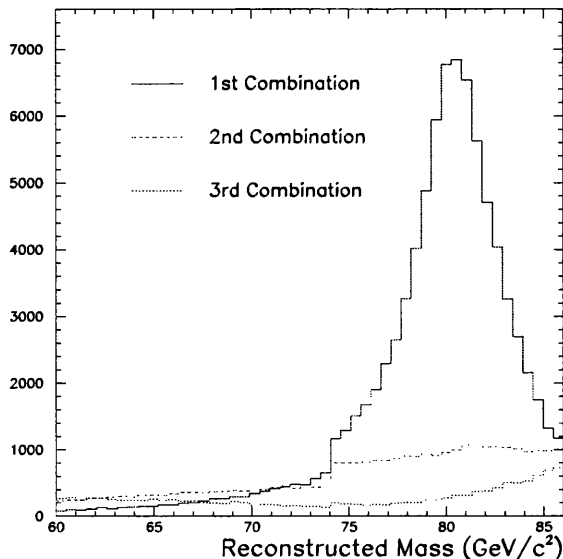


Figure 4.18: The reconstructed mass for the correct and incorrect di-jet pairs, based on the largest matrix element weight.

This method was chosen to find the correct combination in selected signal Monte Carlo events with an efficiency⁸ of 87% whilst also ensuring that the combinatorial background in the W mass peak region is approximately flat [81].

4.5 Events from which to extract the W mass

The method used to extract the W mass uses the invariant mass distributions in data and MC, which have been built using the stages described in the previous sections (the extraction method itself is the subject of Chapter 5). This section gives a description of the MC and data events which are finally selected as input to the W mass extraction stage.

4.5.1 Monte Carlo Events

The MC events which finally enter the 2-D invariant mass distributions from which the W mass is determined are listed in Tables 4.4 and 4.5 for W^+W^- and non-

⁸The absolute efficiency of the pairing algorithm is difficult to calculate, due to particle mixing between jets at the jet-clustering stage. The efficiency is estimated using the number of combinations which *most closely* match the directions of the original W quark-pairs.

W^+W^- processes, respectively.

Process	$W^+W^- \rightarrow q\bar{q}q\bar{q}$	$W^+W^- \rightarrow q\bar{q}l\nu$	$W^+W^- \rightarrow l\nu l\nu$
Generated events	140983	133315	33660
Class 16	139671	132681	436
Preselected	136209	18089	0
Neural net cut	126866	580	0
Jet pairing	106109	403	0
Efficiency (%)	75.3	0.30	0

Table 4.4: W^+W^- events passing selection and mass reconstruction cuts.

Process	u \bar{u}	dd	s \bar{s}	c \bar{c}	bb	ZZ
Generated events	120000	119999	120000	119999	120000	89997
Class 16	105376	108346	108316	105267	109332	58350
Preselected	16049	11619	11581	16476	12548	21425
Neural net cut	2601	1652	1602	2247	747	8817
Jet pairing	1627	1029	973	1414	483	5166
Efficiency (%)	1.36	0.86	0.81	1.18	0.40	5.74

Table 4.5: Non W^+W^- events passing selection and mass reconstruction cuts. Each quark flavour produced in $e^+e^- \rightarrow q\bar{q}$ processes is shown, along with $e^+e^- \rightarrow ZZ$ events.

Figure 4.19 shows the 2-D scatter plots of m_1 and m_2 for signal and background MC. The effect of the pairing mass window is clear and shows how the Breit Wigner tails are included. The key point of the mass measurement in two dimensions is that the event-by-event (m_1, m_2) correlations are naturally taken into account, which will be discussed in detail in Chapter 5. The W^+W^- signal can clearly be seen forming a peak around the reference W mass value ($M_W^{\text{ref}} = 80.35 \text{ GeV}/c^2$), while the background is essentially flat.

The number of events which are expected for the data luminosity at $\sqrt{s} = 189 \text{ GeV}$, $\mathcal{L} = 174.209 \text{ pb}^{-1}$, is calculated from the cross section for each physical process from:

$$N_{\text{exp}} = \sigma \mathcal{L} \epsilon,$$

and each are shown in Table 4.6. The total number of expected events is 1526 (1220 signal and 306 background), taken to be the number of events passing the neural net output cut⁹.

⁹The jet pairing stage reduces the number of events further, but this should not be associated

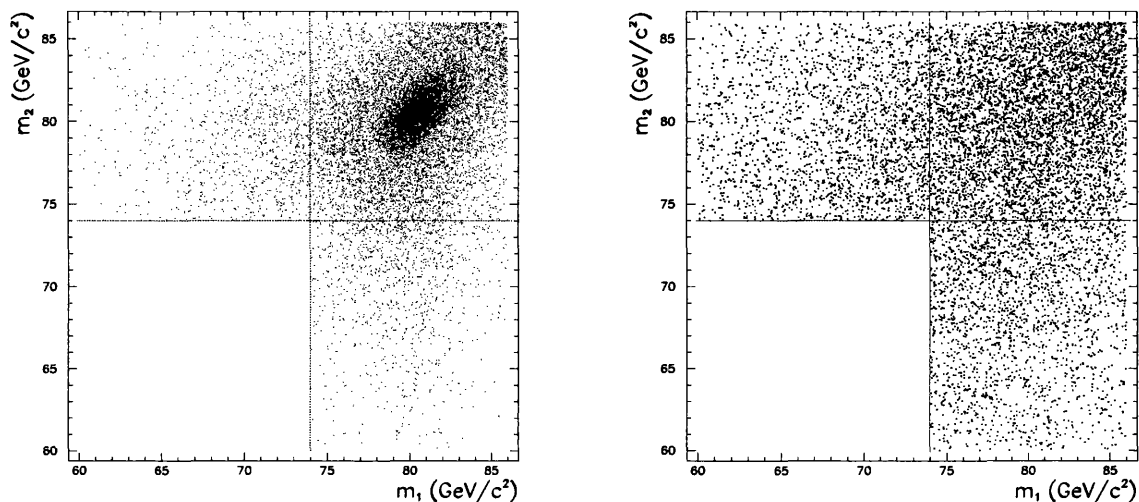


Figure 4.19: Scatter plots showing the (m_1, m_2) mass coordinates of each selected event in signal (left) and background (right). The correlation between m_1 and m_2 in signal and background is $8.0 \pm 0.5\%$ and $1.4 \pm 1.0\%$, respectively for the entire plane and $15.2 \pm 0.5\%$ and $7.0 \pm 1.0\%$ for the $[74, 86]$ GeV/c^2 peak region.

Process	W^+W^-	$u\bar{u}$	$d\bar{d}$	$s\bar{s}$	$c\bar{c}$	$b\bar{b}$	ZZ
N_{exp}	1220	76.65	48.01	46.64	66.25	21.23	47.09

Table 4.6: The number of events for each process which are expected in a sample the size of the real data collected by ALEPH at $\sqrt{s} = 189$ GeV.

4.5.2 Data Events

The number of data events at $\sqrt{s} = 189$ GeV passing all selection cuts and stages in the invariant mass reconstruction procedure are listed in Table 4.7. The expected number of events (1526) is larger than the number actually seen in data (1435), making the measured cross section lower than that predicted by the Standard Model. Figure 4.20 shows the (m_1, m_2) mass coordinates for the selected data events. The

Data events	
Class 16	21724
Preselected	3438
Neural net cut	1435
Jet pairing	1097

Table 4.7: Data events passing selection and mass reconstruction cuts.

final reconstructed 2-D invariant mass distributions in data and Monte Carlo, which are used to measure the W mass, are shown in Figure 4.21.

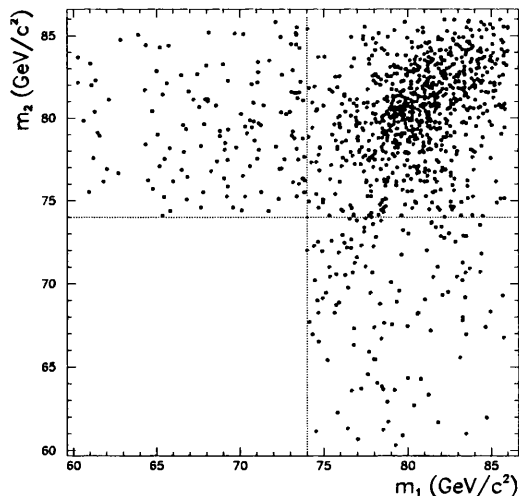


Figure 4.20: Data (m_1, m_2) scatter plot. The correlation between m_1 and m_2 is $6 \pm 3\%$ for the whole plane, and $11 \pm 3\%$ in the $[74, 86]$ GeV/ c^2 peak region, in agreement with the Monte Carlo.

with N_{exp} as it is specific to the mass measurement and not the W^+W^- cross section.

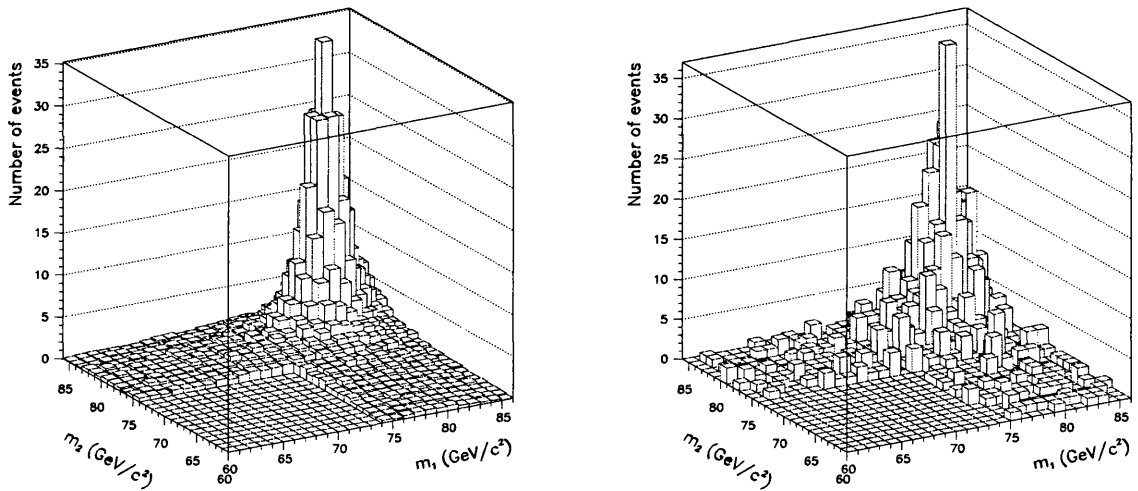


Figure 4.21: The two dimensional distributions used to measure the W mass. In the Monte Carlo (left) the signal and background are added, normalised to the observed number of data events, and the high statistics result in a smooth profile. Statistical fluctuations are clearly seen in the data (right), especially in the distribution tails.

Chapter 5

W Mass Measurement

5.1 Mass Extraction Methods

There are several strategies available to extract a W mass estimator from the distribution of reconstructed invariant mass [11]. For a precision measurement of M_W a method which allows tight control of *systematic* effects is necessary, whilst also keeping the statistical uncertainty as low as possible. The statistical error is largely determined by factors outside the mass extraction method, such as the size of the data sample and the resolution of the invariant mass distribution. A brief description of these methods and their precision relative to the method adopted in this thesis (Monte Carlo reweighting) is given below.

5.1.1 Breit Wigner Fit

The invariant mass distribution is fitted with a function, e.g. a double Breit Wigner (BW) (see Equation 2.33) convoluted with a Gaussian to describe the signal peak which is added to another simple function to describe the background. However, the experimental distribution is distorted due to background contamination, detector resolution, initial state radiation, phase space restrictions, and the general reconstruction procedure. These cause biases and distortions in the distribution, which cannot be accurately incorporated into a simple analytical fit. The bias can be removed by calibrating¹ the measurement from MC, which constitutes a further systematic error. This method is straight forward, but limited in that the fit function

¹This is the technique of correcting for the known response of the fitted W mass to the true W mass, which is determined from numerous samples generated with various values of M_W^{true} .

is not unique and its choice can therefore influence the mass estimator and corresponding error. When used as a cross-check for the W mass measurement at $\sqrt{s} = 172 \text{ GeV}/c^2$, the statistical precision was $\sim 10\%$ less than the method of one dimensional MC reweighting [68].

5.1.2 Convolution

This method uses the information contained in the differential cross section in terms of the two invariant masses. The use of the correct underlying physics function would eliminate the bias from a simple BW fit. The W mass estimator is built by maximising an event by event log-likelihood function with respect to M_W :

$$\log(\mathcal{L}(M_W)) = \sum_{i=1}^{N_{\text{evts}}} \log \mathcal{P}(s_1^i, s_2^i | M_W),$$

where $\mathcal{P}(s_1^i, s_2^i | M_W)$ is the probability of event i with invariant masses (s_1, s_2) . The first step toward this, known as ‘first generation fitting’, uses the di-jet masses and accounts properly for the dynamics of W pair production. However it does not utilise all the information contained in the event; for example, the combinatorial background in the hadronic channel is not treated at all. A measurement of the W mass from the hadronic channel at $\sqrt{s} = 183 \text{ GeV}/c^2$ using this method [82] gave a statistical precision $\sim 5\%$ less than the method using two-dimensional MC reweighting. The optimal way to measure the W mass (at least in principle) is to extend this method to a ‘second generation fit’, which uses *all* the statistical information in each event. This not only includes the two invariant masses, but the full kinematical information contained in the four fermion four-momenta. A statistical improvement of $\sim 10\%$ over the method of MC reweighting was obtained when applying this method to the hadronic W mass measurement at $\sqrt{s} = 172 \text{ GeV}/c^2$ [83]. However, it is a highly sophisticated analysis involving multi-dimensional numerical integration, and as a result requires many hours of processing time making systematic and stability checks lengthy. Also, there is the possibility that selection cuts may bias the result.

5.1.3 Monte Carlo Interpolation

The invariant mass distribution of the data can be compared directly to a number of Monte Carlo samples generated at different values of M_W to find the best W mass

estimator. The accepted MC events are compared to the accepted data events, thus removing any bias from selection cuts. A χ^2 quantity is built which is interpolated to find the best W mass estimator. The immediate problem with this method is the need to generate large amounts of MC at different W masses, which is impractical. The problem of needing to generate large amounts of MC can be overcome with the procedure of Monte Carlo reweighting.

5.1.4 Monte Carlo Reweighting

The mass extraction method used for the analysis described in this thesis uses the MC reweighting technique [84]. The approach is the same as MC interpolation, but instead of producing many MC samples, a large MC sample is created at one central reference W mass, M_W^{ref} , which is then reweighted to correspond to other W masses, M_W^0 . This procedure is detailed in the following section.

5.2 Monte Carlo Reweighting

Event weights are evaluated using the lowest order CC03 matrix element of the process $e^+e^- \rightarrow W^+W^- \rightarrow q\bar{q}q\bar{q}$. The calculation of this matrix element \mathcal{M} requires the four ($\mu = 1, 4$) generated parton 4-momenta, p_i^μ , for the i^{th} MC event, in addition to a mass (M_W) and width (Γ_W). To reweight each event of the invariant mass distribution generated with $M_W = M_W^{\text{ref}}$ to the distribution corresponding to $M_W = M_W^0$ the event weight would be the ratio of the two corresponding matrix elements,

$$w_i(M_W^0, \Gamma_W^{\text{ref}}) = \frac{|\mathcal{M}(M_W^0, \Gamma_W^{\text{ref}}, p_i^1, p_i^2, p_i^3, p_i^4)|^2}{|\mathcal{M}(M_W^{\text{ref}}, \Gamma_W^{\text{ref}}, p_i^1, p_i^2, p_i^3, p_i^4)|^2}. \quad (5.1)$$

The reweighted distribution is then compared with real data to produce the best estimator of M_W . It is a noticeable feature that the masses of the two W's are implicit in the four four-vectors. The weight is an *event* weight, and therefore may be applied to other event distributions with the implications of being able to use other variables for fit quality studies. The W width, Γ_W , is allowed to vary with the SM prediction defined in Equation 2.30. Figure 5.1 shows the agreement between a mass distribution generated at a particular W mass and a reference distribution reweighted to that mass. Plot (a) is a flat distribution which is expected, with a constant value of

six which is simply the ratio of the different statistics used in the two distributions. The second plot (b) clearly shows the weighting of the reference mass distribution to a lower mass. The effect of using the CC03 diagrams in the calculation of the matrix element, rather than the full four-fermion calculation, is negligible (a W mass shift of $M_W^{CC03} - M_W^{Af} \sim 3 \text{ MeV}/c^2$ was observed at $\sqrt{s} = 172 \text{ GeV}/c^2$ [68]).

To accelerate the fitting procedure, reweighted Monte Carlo invariant mass distributions are generated at $50 \text{ MeV}/c^2$ W mass parameter intervals in the range $[79,82] \text{ GeV}/c^2$. The content of each bin in the invariant mass distribution corresponding to any M_W parameter is then estimated by linearly interpolating between the same bins in the two nearest (pre-calculated) invariant mass distributions. The approximation by the interpolation technique has a negligible effect on the fitted W mass, and accelerates the fitting procedure by a factor of $\sim 10^2$. Figure 5.2 shows the effect on the invariant mass distribution when reweighting the central MC sample to the W mass parameters at the edges of the fit range.

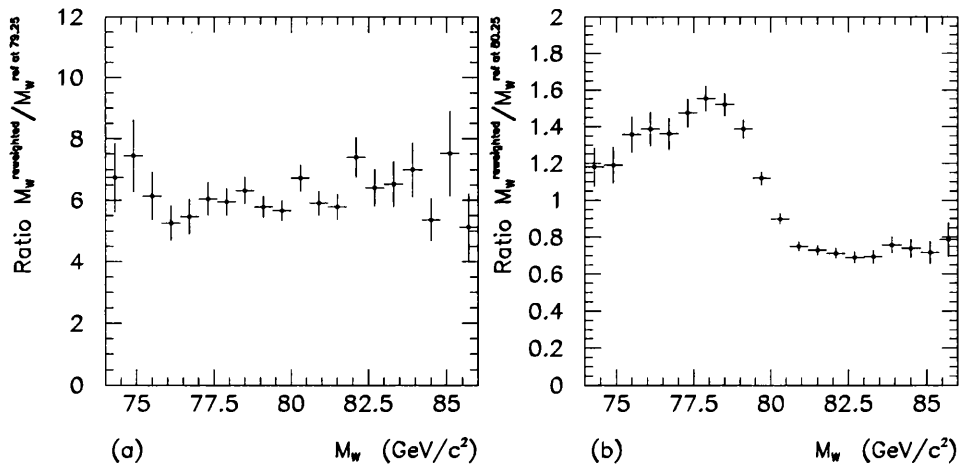


Figure 5.1: (a) The result of dividing the invariant mass distribution produced when reweighting an $M_W^{\text{ref}} = 80.25 \text{ GeV}/c^2$ MC sample to $M_W = 79.25 \text{ GeV}/c^2$ by the actual (mock data) distribution at $M_W^{\text{ref}} = 79.25 \text{ GeV}/c^2$. (b) The same *reweighted* sample divided by the actual MC at $80.25 \text{ GeV}/c^2$.

The success of the technique relies on how well the generated Monte Carlo sample describes the data. This is the case for all the mass extraction methods discussed here, and in fact an inherent uncertainty in most high energy physics analyses. Stringent tests between data and MC simulation are necessary to constrain this uncertainty.

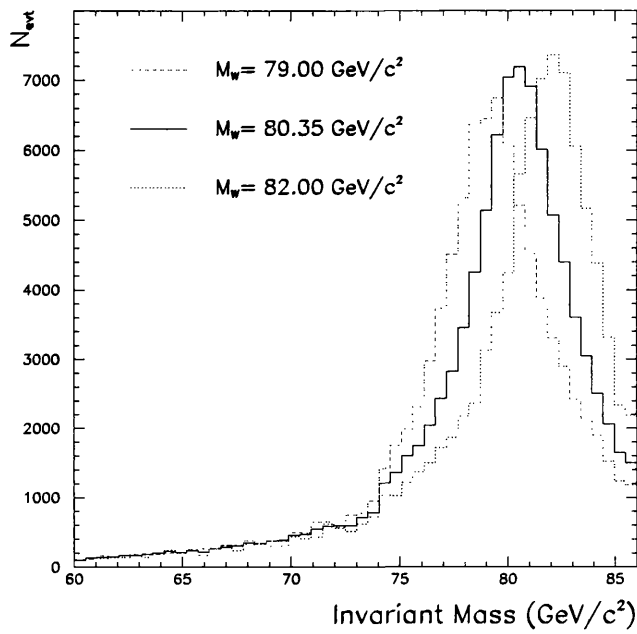


Figure 5.2: The effect on the invariant mass distribution when reweighting the reference MC, generated at $M_W = 80.35 \text{ GeV}/c^2$, to masses corresponding to the lower and upper limits of the fit range [$79.00 - 82.00 \text{ GeV}/c^2$]. The most sensitive region is centered around the reference mass value, while the tails change very little.

5.2.1 Statistical Improvement in 2D

In the analysis of the earlier 172 GeV data [68], the reweighting procedure was applied to the two one-dimensional di-jet mass distributions separately (denoted the ‘1-D’ method). These were each filled by one mass per event, with the two masses randomised. The final mass was calculated as the weighted average of the two fit results $m_1 \pm \sigma_1$ and $m_2 \pm \sigma_2$, taking into account the correlation ρ between the two fitted masses². This is not optimal as it does not utilise the full shape information of the correlations between the two mass distributions. The higher statistics at $\sqrt{s} = 183$ GeV allowed the probability density function to become dependent on both di-jet masses, denoted $p.d.f.(m_1, m_2)$, hence a true 2-dimensional reweighting technique can be applied. The full correlation between the two di-jet masses in the data are then properly accounted for and lead to an improvement in statistical precision compared to the 1-D method [85].

To illustrate this, consider the case where m_1 and m_2 each form Gaussian distributions. By definition, they are correlated only by their covariance, hence there would be no gain in the 2-D over the 1-D method since the covariance is properly taken into account in the combination of the two 1-D fitted masses. However, now consider introducing distortions into the distributions which cause non-Gaussian shoulders and tails. These contain information about m_1 and m_2 by contributing higher orders, or moments, to the correlation, thus changing the *shape* of the $p.d.f.$. This is elegantly expressed by the multivariate Edgeworth expansion [86] for a multivariate $p.d.f.$, $f(x)$, expanded around a multivariate Gaussian $G(x, \lambda)$:

$$f(x) = G(x, \lambda) \left[1 + \underbrace{\frac{1}{6} k^{ijk} h_{ijk}(x, \lambda)}_{\text{skewness}} + \underbrace{\frac{1}{24} k^{ijkl} h_{ijkl}(x, \lambda)}_{\text{kurtosis}} + \frac{1}{72} k^{ijk} k_{lmn} h_{i..n}(x, \lambda) + \dots \right],$$

where x are the expectation values of the data, λ is the covariance matrix, $h_{ij..}$ are Hermite tensors and k the ‘higher-order cumulant’ matrices. k^{ijk} is the skewness and k^{ijkl} the kurtosis matrix. If these higher orders were taken into account in the 1-D method it would be statistically equivalent to the 2-D, but the 2-D $p.d.f.$ contains this naturally. In the W mass analysis real distortions are implicit in the Breit Wigner distributions of m_1 and m_2 , which contain W mass information.

²The weighted average is calculated from: $\bar{m} = p_1 m_1 + p_2 m_2$ with a statistical error of $\bar{\sigma} = p_1 \sigma_1 + p_2 \sigma_2$, where $p_1 = \frac{\sigma_2^2 - \rho \sigma_1 \sigma_2}{\sigma_1^2 + \sigma_2^2 - 2\rho \sigma_1 \sigma_2}$ and $p_2 = \frac{\sigma_1^2 - \rho \sigma_1 \sigma_2}{\sigma_1^2 + \sigma_2^2 - 2\rho \sigma_1 \sigma_2}$.

5.2.2 Building the *p.d.f.*

The two-dimensional MC reference mass distribution is binned separately on two (m_1, m_2) planes, one for signal and one for background. Each event produces a single ‘mass coordinate’ on this 2-D plane, which is reflected about the diagonal $m_1 = m_2$ (this is for algorithmic simplicity). The probability density function for a *data* event to have a certain invariant mass coordinate (m_1, m_2) , is the sum of the signal and background contributions:

$$p.d.f.\textit{.signal} + p.d.f.\textit{.background} = \rho_s(M_W) \frac{N_s^{ij}(M_W)}{\Delta_{ij}^s N_s^{tot}} + \rho_b(M_W) \frac{N_b^{kl}}{\Delta_{kl}^b N_b^{tot}}, \quad (5.2)$$

where the signal and background bins are denoted by the coordinates (i, j) and (k, l) , respectively. The Δ are the bin area, defined as $(\delta m_i^s \cdot \delta m_j^s)$ and $(\delta m_k^b \cdot \delta m_l^b)$. For the case of the background contribution, N_b^{kl} is simply the number of events found in bin (k, l) . For the signal the number of events in each bin depends on the W mass, as the events are weighted:

$$N_s^{ij}(M_W) = \sum_{ievt=1}^{N_{ref}^{ij}} w_{ievt}(M_W), \quad (5.3)$$

where N_{ref}^{ij} is the number of events in bin (i, j) when $M_W = M_W^{ref}$, i.e. *un*-weighted events. N_s^{tot} and N_b^{tot} are the sum over all bins on the (m_1, m_2) plane for signal and background. w_{ievt} is the event weight from Equation 5.1.

ρ_s represents the signal purity, thus $\rho_b = 1 - \rho_s$, and is defined as

$$\rho_s(M_W) = \frac{\epsilon_s \sigma_s(M_W)}{\epsilon_s \sigma_s(M_W) + \epsilon_b \sigma_b}, \quad (5.4)$$

where ϵ_s and ϵ_b are the signal and background efficiencies, respectively. Since the W^+W^- cross section σ_s changes with the W mass (see Section 2.3.3), this needs to be incorporated into the fit to ensure the correct signal to background normalisation as the W mass parameter varies. The W mass dependence is small compared to the effect of reweighting and it is therefore sufficient to parameterise it with a parabola in the region around M_W^{ref} . This is shown in Figure 5.3.

The best estimator of the W mass is taken to be the one which maximises the likelihood function,

$$\mathcal{L}(m_w) = \prod_{i=1}^{N_{evt}} p.d.f.(m_1^i, m_2^i | M_W), \quad (5.5)$$

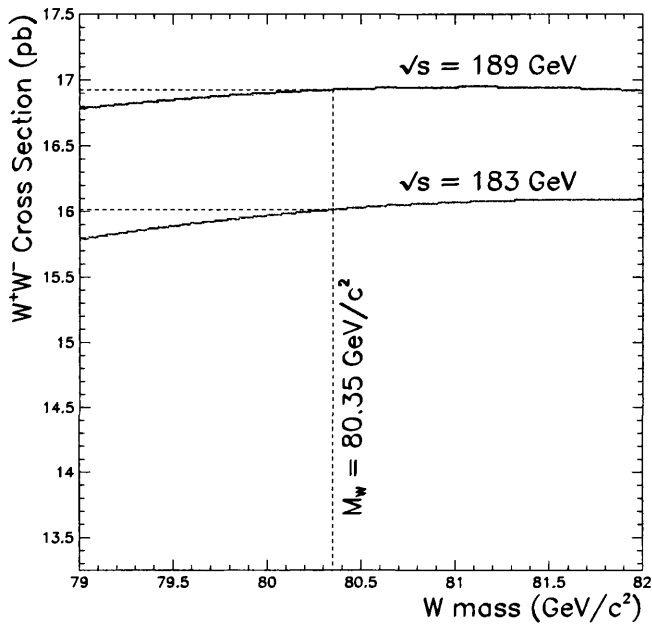


Figure 5.3: The parameterisation of the W^+W^- cross section dependence on M_W in the fit region [79.00 - 82.00 GeV/c^2] at $\sqrt{s} = 189$ GeV and at $\sqrt{s} = 183$ GeV for comparison, showing the values at the reference mass. The functional form of the parabola at $\sqrt{s} = 189$ GeV is: $\sigma_s(M_W) = \sigma_s(M_W^{ref}) \left(1 + 0.003358(M_W - M_W^{ref}) - 0.002178(M_W - M_W^{ref})^2 \right)$, calculated using the GENTLE package [87].

where N_{evt} is the number of selected data events. Since the same event selection and invariant mass reconstruction procedure is applied to data and Monte Carlo, the final W mass estimator does not need to be calibrated. The central value of the mass estimator and its statistical error are determined using the minimisation tool ‘MINUIT’ [88].

5.3 Statistical Limitations of MC reweighting

The reweighting technique is statistically limited, as the effective number of events n_{eff} decreases the further the central MC sample is reweighted:

$$n_{eff} = \frac{(\sum w_i)^2}{(\sum w_i^2)}. \quad (5.6)$$

The effective number of events must be much larger in the MC than in the data sample fitted. In addition, if n_{eff} is small compared to the true (unweighted) number of events in the reference MC, the reweighting procedure is inefficient, and this may bias the W mass estimator.

The statistical fluctuations implicit in the finite reference sample are amplified the further the sample is reweighted away from its generated mass. This effect is critical in the 2-D method, where two dimensional bins in the tails of the (m_1, m_2) distribution do not contain many events. The effect of making the binning small in the tails and then reweighting is to produce a reweighted mass distribution dominated by statistical fluctuations. Containing little information other than the reference mass value, the resulting fitted W mass will tend towards the value of the reference mass used. This is clearly seen in Figure 5.4, where reference samples at the extreme mass points have been reweighted in bins of 0.5×0.5 GeV/ c^2 across the whole *p.d.f.*. The fitted W masses are ‘pulled’ towards the reference sample mass. For this reason, the effect of finite statistics in the reference is included as a systematic error on the W mass and will be discussed further at the end of this chapter. In the 189 GeV analysis the final fitted W Mass is not far from the reference sample mass, so the effect of non-linearity would be minimal.

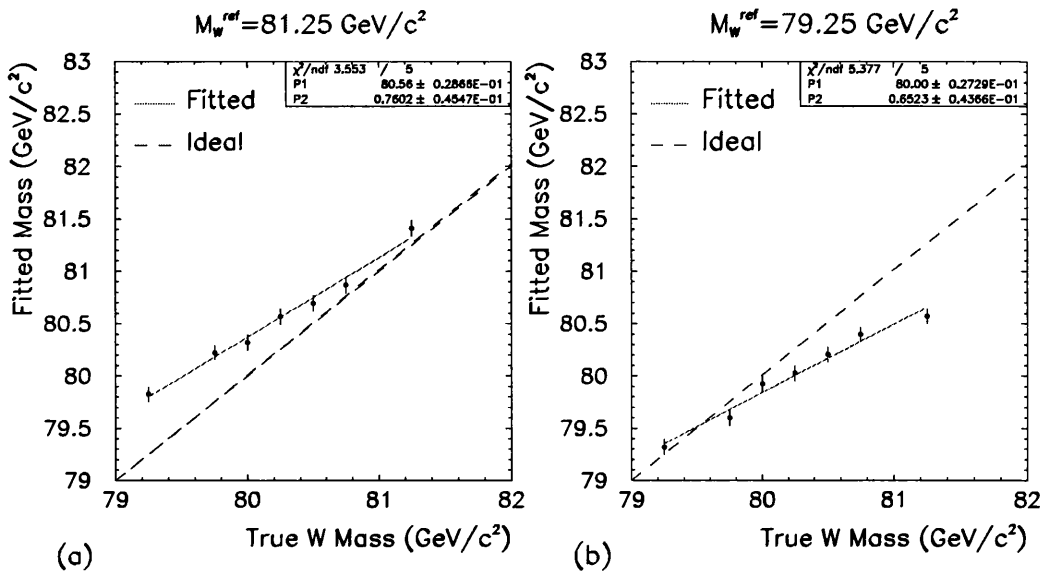


Figure 5.4: The effect of finite Monte Carlo statistics on the linearity of the 2-D reweighting technique at $\sqrt{s} = 183 \text{ GeV}$ when reweighting too far from the reference mass (constant bins of $0.5 \times 0.5 \text{ GeV}/c^2$ were used across the whole $p.d.f.$). Monte Carlo generated at (a) $81.25 \text{ GeV}/c^2$ and (b) $79.25 \text{ GeV}/c^2$ were used for the reference sample.

5.3.1 Binning of the $p.d.f.$

The binning of the $p.d.f.$ must be chosen carefully to minimise possible bias from the finite reference statistics, while maximising the sensitivity to the W mass. Many studies were performed using different binning schemes to optimise the precision of the mass measurement. To illustrate the effect on the W mass, Figure 5.5 shows the linearity using two simple binnings; $0.5 \times 0.5 \text{ GeV}/c^2$ and $1.0 \times 1.0 \text{ GeV}/c^2$ of constant size across the whole $p.d.f.$. With smaller bins across the whole $p.d.f.$ the fitted masses at the extreme points are pulled towards the reference mass value, due to there being too few events to sufficiently populate all bins. Enlarging the bin area by a factor of four ensures the linearity of the fit, although these are somewhat large to be optimally sensitive to the W mass.

The choice of binning for the preliminary ALEPH W mass result at $\sqrt{s} = 183 \text{ GeV}$ [89] was a grid of 0.5×0.5 and $1.0 \times 1.0 \text{ GeV}/c^2$ bins in the peak and tail regions, respectively, and is shown in Figure 5.6.

The reference $p.d.f.$ for the measurement at $\sqrt{s} = 189 \text{ GeV}$ [79] has been binned

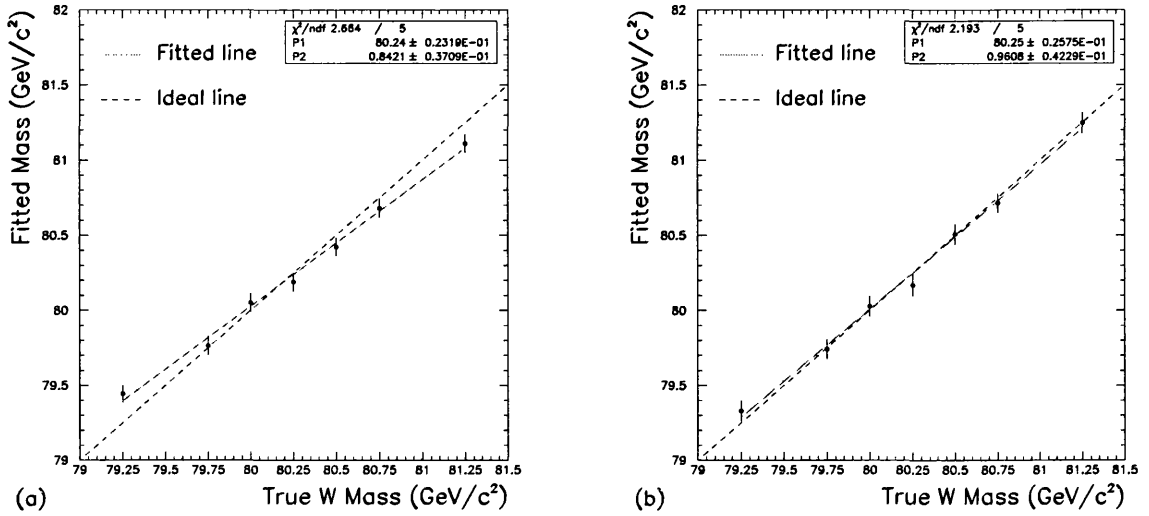


Figure 5.5: Linearity of mass extraction when using fixed binning across the entire *p.d.f.*, showing the improvement when going from bins of (a) 0.5×0.5 GeV/c² to bins of (b) 1.0×1.0 GeV/c².

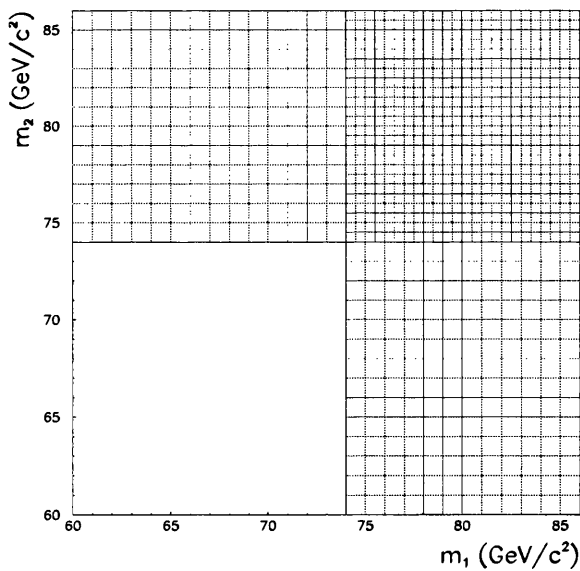


Figure 5.6: The binning used for the preliminary measurement at $\sqrt{s} = 183$ GeV, showing coarse bins in the tails and finer structure in the peak region. The region $(m_1, m_2) \in [60, 74]$ GeV/c² is empty due to the mass window cut.

using a more sophisticated scheme which determines an optimal binning using the following criteria:

- Divide the 2-D plane into different regions of sensitivity;
- Variable bin sizes in each sensitivity region;
- Demand minimum number of events per bin;
- Separate binning for signal and background.

The algorithm constructs three different variable binnings for both the signal and background *p.d.f.s*, corresponding roughly to the peak and tails of the two dimensional Breit Wigner distribution. These regions are naturally defined by the mass window criteria discussed earlier. The requirement of a minimum number of events N_{ij}^{min} in each bin determines the size of the bins. This is performed iteratively for each region in signal and in background. After an initial ‘guess’ binning, the algorithm tunes the number of bins until each one satisfies the N_{ij}^{min} condition. Figure 5.7 shows the resulting binning scheme when $N_{ij}^{min} = 200$.

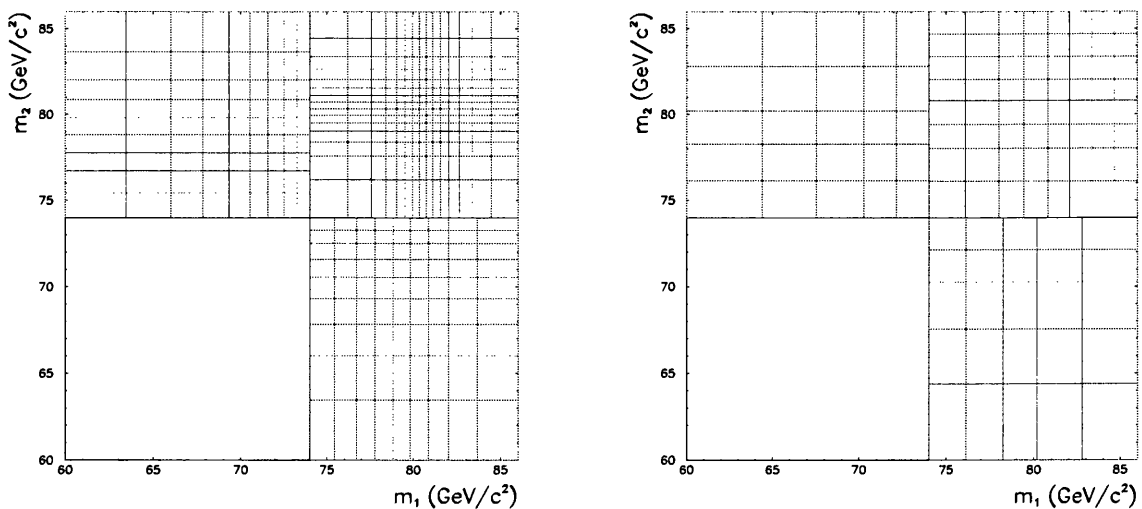


Figure 5.7: Binning for signal (left) and background (right) used for the measurement at $\sqrt{s} = 189$ GeV. The bins are enlarged until they each contain a minimum number of events and the regions of sensitivity can be seen where the bins become small (compare with the actual scatter plots in Figure 4.19).

5.4 W Mass Parameter Estimation

The general method of evaluating the statistical error $\hat{\sigma}$ on an estimated parameter \hat{m} , say, is to calculate its confidence levels (CL), which define a region that contains the *actual* value of the parameter a certain fraction of the time. Normally, a CL of 68% is used to calculate $\hat{\sigma}$, as this corresponds to one standard deviation of a Gaussian distribution. In the limit of large sample sizes, the likelihood function \mathcal{L} , as used to estimate the W mass (Equation 5.5), is Gaussian. Thus $\log(\mathcal{L})$ is a parabola which is maximum at \hat{m} and its derivative is constant. $\hat{\sigma}$ can then be determined analytically by inverting the 2nd derivative of $\log \mathcal{L}$ (the covariance matrix). However, to obtain the particular CL of 68% it is numerically equivalent to simply use

$$\pm \hat{\sigma} = \sigma \left(\log \mathcal{L}_{max} \pm \frac{1}{2} \right) \quad (5.7)$$

as the upper and lower limits of the CL region. This provides a good estimate of the statistical error on the fitted parameter for a single data sample, and is often called the ‘fit error’. However, it is an approximation which assumes the errors are Gaussian and that the response of the analysis to the true parameter is linear. These are discussed in the following sections, respectively. In addition to the fit error, fitting a parabola to the likelihood curve gives a ‘parabolic error’, which should be consistent with the average fit error.

5.4.1 Expected error

The true coverage of the CL interval can only be determined by simulating many experiments using Monte Carlo. Many MC ‘sub-samples’ (typically hundreds) are built which contain the same number of events as observed in the data, and each is fitted using the reweighting procedure in exactly the same way as the data. The R.M.S. spread of these fitted masses is called the ‘expected error’, and is considered a more robust estimate of the statistical error on the W mass. If the fit error (as defined above) is a correct estimate of the statistical uncertainty on the W mass, the expected error should be consistent with the mean of the fit (and parabolic) error distributions. In addition to estimating the error, the method of fitting subsamples

allows the consistency³ of the estimator to be checked. Since only MC events are used, the mean of the distribution of fit results should be equal to the W mass that those subsamples were generated with. The distribution of fitted masses and their fit errors are shown in Figure 5.8.

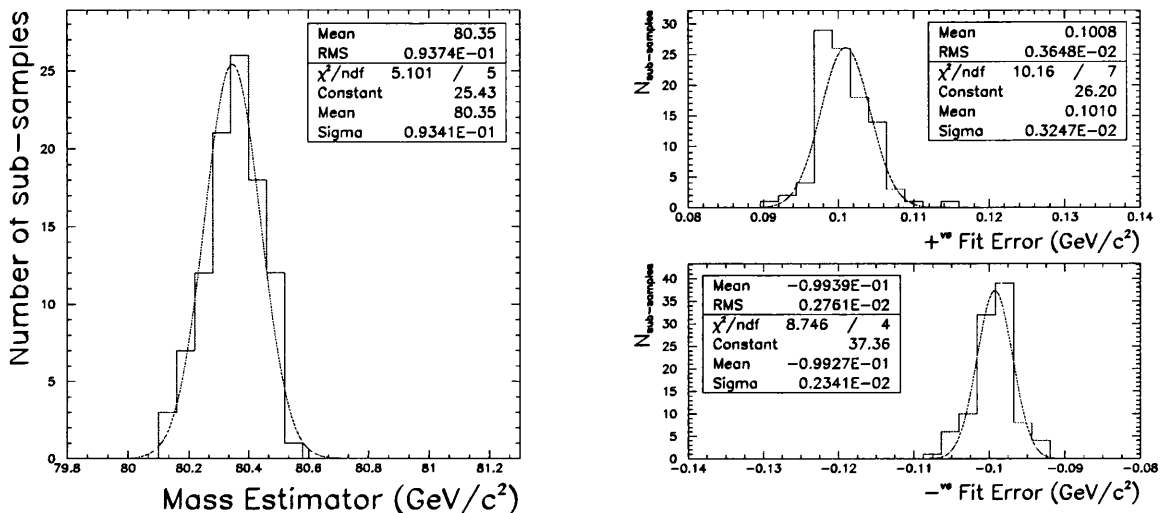


Figure 5.8: The expected error on the W mass is taken to be the R.M.S. of the mass distribution from fitting 100 sub-samples (left). The positive and negative errors from each fit, calculated by MINUIT [88], are shown on the right and are in agreement with the R.M.S.. A fit to a Gaussian gives a low χ^2 and the mean of the mass distribution is consistent with the reference W mass, $M_W^{\text{ref}} = 80.35 \text{ GeV}/c^2$ (for MC generated at $\sqrt{s} = 189 \text{ GeV}$).

5.4.2 Linearity of method

A critical test of the reweighting method is to ensure that the fitted mass agrees with the true input mass, when performing a fit to a MC sample generated with a known M_W . The linearity of the fitted mass with true input mass has been studied using 7 independent MC samples generated at different W masses: $M_W = 79.35, 79.85, 80.10, 80.35, 80.60, 80.85$ and $81.35 \text{ GeV}/c^2$. The gradient of this calibration curve should be equal to unity with a central value of $M_W = M_W^{\text{ref}}$ by definition, since the data and MC are treated identically. This is demonstrated in Figure 5.9.

³When discussing the properties of parameter estimation, the term *consistency* is used to describe how well the estimator reproduces the true parameter value, whilst the statistical precision on this value is described in terms of the *efficiency* of the estimator.

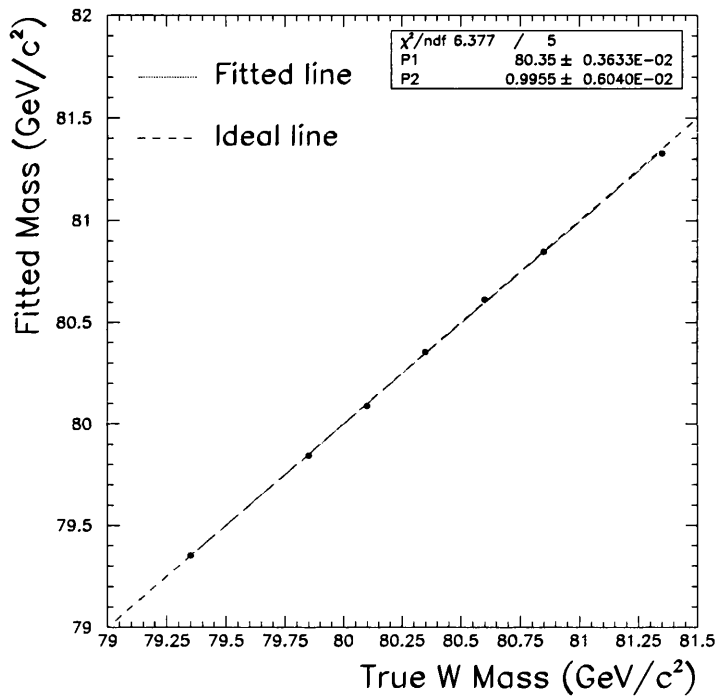


Figure 5.9: Linearity of the 2-D reweighting technique at $\sqrt{s} = 189$ GeV, using the binning shown in Figure 5.7. A straight line fit gives a gradient consistent with 1 and an offset consistent with $M_W^{\text{ref}} = 80.35$ GeV/ c^2 .

5.4.3 Results at 189 GeV

The data invariant mass distribution is shown in Figure 5.10, along with the Monte Carlo signal generated with $M_W^{\text{ref}} = 80.35 \text{ GeV}/c^2$ and the non- W^+W^- background. The fit between data and MC as a function of W mass is shown by the likelihood curve in Figure 5.11, and the best W mass estimator is found to be

$$M_W = 80.539 \text{ }^{+0.109}_{-0.110} \text{ (stat.) GeV}/c^2.$$

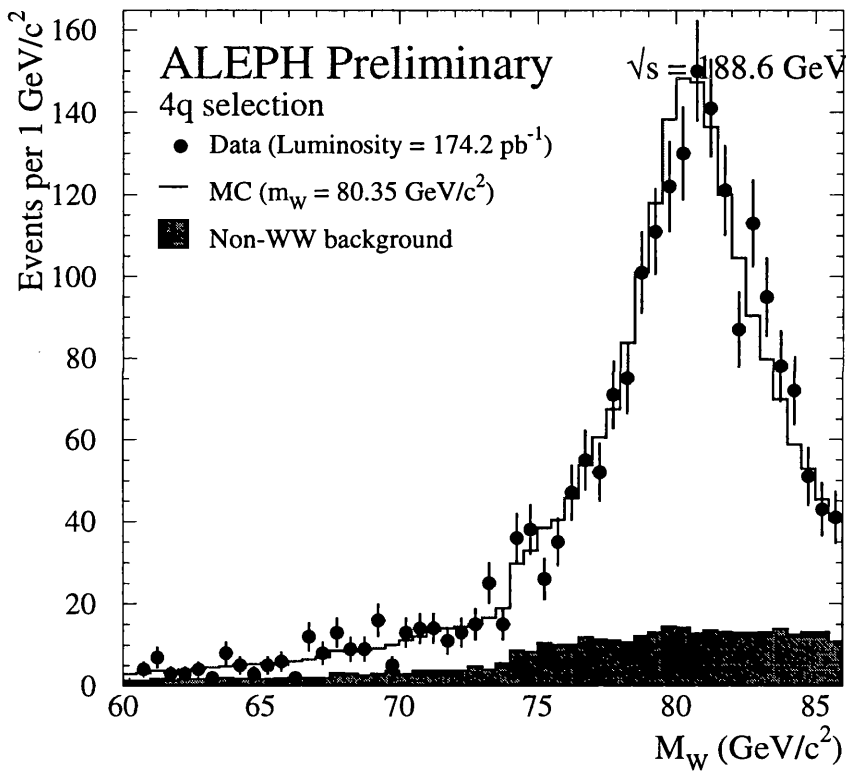


Figure 5.10: The invariant mass distributions in data and MC which are fitted to find the best W mass estimator. There are two entries per event, reducing the 2-dimensional *p.d.f.* to a 1-dimensional plot.

All the information used to check the statistical error on the W mass is contained in Figure 5.12. The lower and upper confidence levels are defined by performing many sub-sample fits at each generated W mass value. The resulting distributions of fitted mass values at each generated W mass are then subject to a simple analysis,

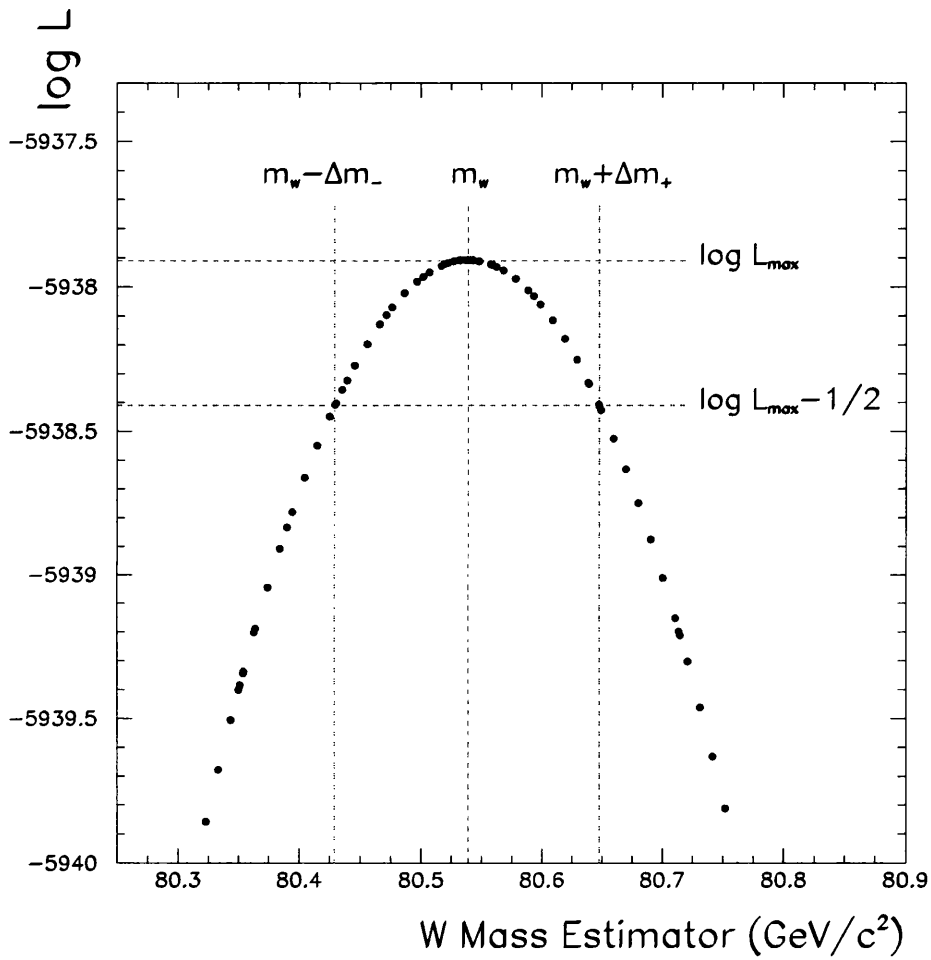


Figure 5.11: The likelihood curve obtained from the fit to data at $\sqrt{s} = 189$ GeV. It describes a parabola with its minimum providing the W mass estimator and statistical errors, as indicated.

which iterates in mass increments symmetrically about their mean until the mass region which contains 68 ± 1 % of the fitted values is determined. Straight lines are fitted to these points and their intercept with the fitted value from data defines the true mass region in which the data value is expected to be found 68% of the time, defining a 68% confidence interval (CI): $M_W \in [80.453, 80.639]$. The lower CL has a gradient equal to one, while the upper CL has a gradient with a small bias to lower masses. The confidence interval is therefore slightly divergent towards higher masses which means the expected error (as defined in Section 5.4.1) on the *measured* W mass is underestimated since it is evaluated at $M_W = 80.35 \text{ GeV}/c^2$. One could define a ‘true’ expected error for the fitted data mass of ${}^{+0.100}_{-0.086} \text{ GeV}/c^2$, which takes into account this divergence. However, the effect of the divergent CI is much smaller than the uncertainty on the expected error itself and in addition, since the measured W mass is not far from the reference mass value the effect is reduced. Therefore the expected error can effectively be considered as independent of the W mass parameter.

5.5 Stability Checks

Several checks of the stability of the mass analysis at $\sqrt{s} = 189 \text{ GeV}$ have been performed, which monitor the linearity, expected error and data fit value while varying certain parameters in the analysis.

5.5.1 Binning

To optimise the bin size used to build the *p.d.f.*, a study is made of the expected error as a function of the minimum number of events demanded per bin. This is shown in Figure 5.13. The expected errors are correlated between each binning scheme used, since the sub-samples which are fitted contain the same events. To see the effect of the change in binning, correlated errors are plotted which are the *difference* in expected error from the one obtained using the ‘standard’, or optimal, method⁴. The expected error is stable with changes in the *p.d.f.* binning, and the

⁴These points are calculated by taking the mean of the sample-by-sample distribution of the difference between masses fitted using $N_{bin}^{min} = 200$ and any other value of N_{bin}^{min} .

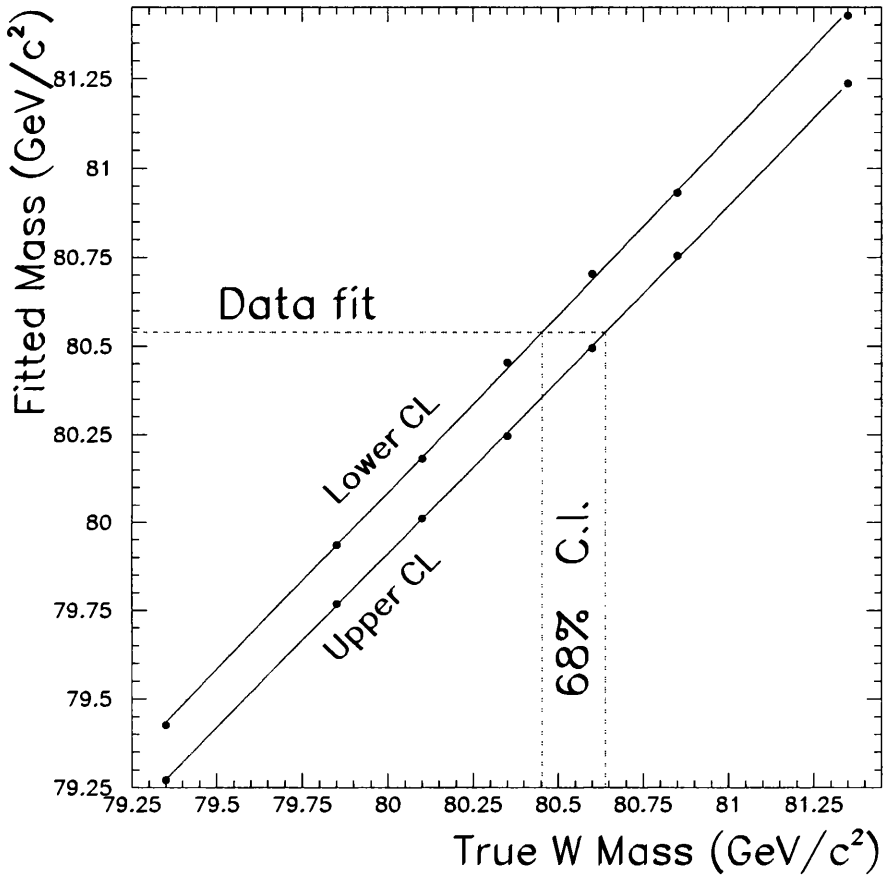


Figure 5.12: Straight line fits give a gradient of 1.003 ± 0.006 and 0.983 ± 0.006 for the lower and upper confidence levels, respectively, which defines the confidence interval (CI). The region defined by the intercept of these lines with the data fit value define the 'true' expected error on the W mass.

deviation from the quoted error is small ($\sim 2\%$). The data value is also stable with

N_{bin}^{min} .

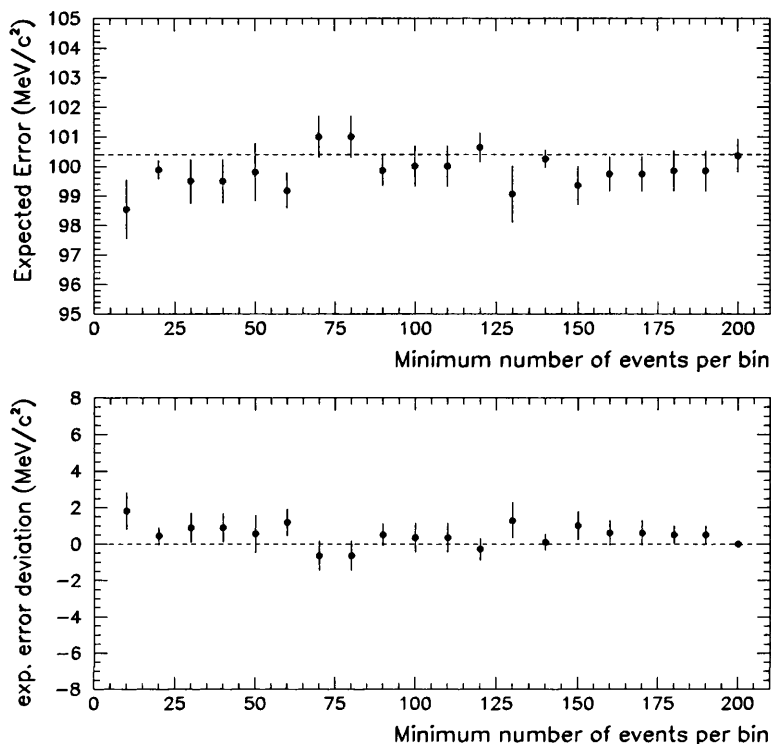


Figure 5.13: Stability of the expected error when changing the minimum number of events in each bin. The top plot shows the mean of the parabolic error (as defined in Section 5.4), while the bottom plot shows the deviation in expected error from the method used for the W mass measurement ($N_{bin}^{min} = 200$). The horizontal dotted lines show the value obtained when using $N_{bin}^{min} = 200$.

The slope of the calibration curve has been checked when varying N_{bin}^{min} (Figure 5.14). As more events per bin are demanded, the effect of finite Monte Carlo statistics on the fitted mass are reduced, and the gradient of the calibration curve approaches unity.

In addition, the binning method has been cross checked by comparing it with a different binning algorithm [90]. The final bin sizes are determined in a similar way by requiring that they must contain a minimum number of events. However, the same bins are used for both signal and background, scaling the background by

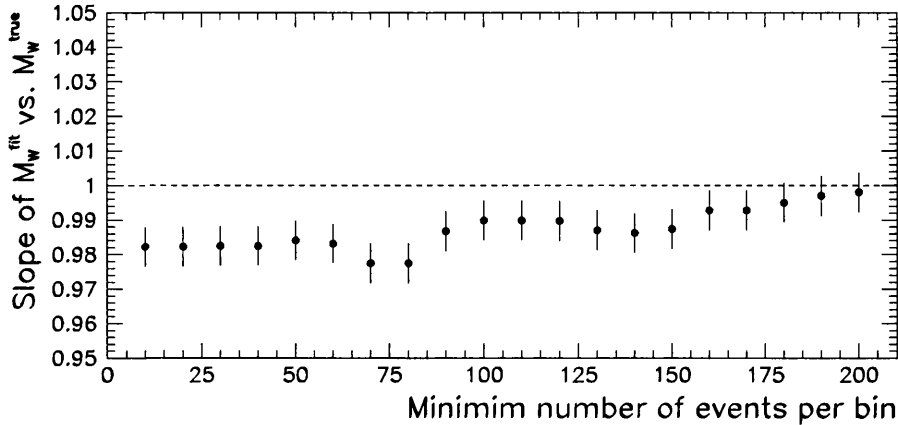


Figure 5.14: Stability of the linearity when changing the minimum number of events in each bin. The slope of the calibration curve approaches unity as the number of events per bin increases, and is considered stable at $N_{bin}^{min} = 200$.

the correct proportions, and the optimisation stage divides (or multiplies) the bin area by a factor of 4 on each iteration. The resulting binning scheme is therefore built from square bins only, and does not have any discontinuity across the *p.d.f.* since both the peak and tail regions are covered by the same iterative steps (c.f. Figure 5.7, where there is a mis-match between bins at the boundaries between the peak and tail regions). This algorithm is somewhat simpler than the one described in Section 5.3.1, but a separate binning for signal and background is favourable from a conceptual point of view.

5.5.2 Neural Net cut

In a similar way, the stability of the expected error and the data fit value as a function of the Neural Network output cut have been studied. Since different values of this cut will select different sub-samples, it is not straight forward to calculate the correlations between the expected errors, although it is expected to be high. Figure 5.15 shows the NN cut dependence, where 0.3 is the value obtained to optimise the efficiency and purity (Section 4.1.3). When using an NN cut of 0.0 the events entering the fit are preselected only. Therefore despite a larger number of events in the fit, the non- W^+W^- background is high and as a result the statistical error on

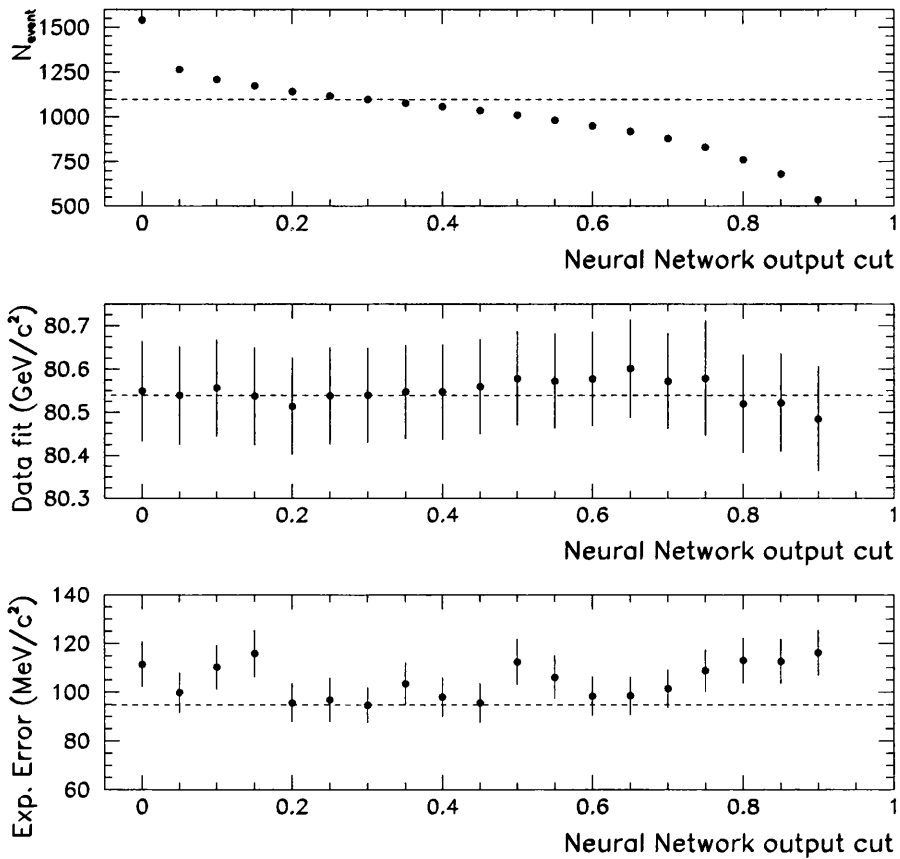


Figure 5.15: Stability of the data fit value (middle) and expected error (bottom), defined as the R.M.S. of the mass distribution in Figure 5.8, when varying the cut made on the NN output. The top plot shows the number of selected data events as a function of NN cut and the dotted lines the values obtained with a cut of 0.3.

the W mass increases. As the cut becomes harder, the selected events are less likely to contain this background but the statistical error increases due to the reduced size of the event sample.

5.5.3 Mass Window

The mass window criteria is checked by varying the size and shape of the mass region in which events are selected. Again the results are correlated but as for varying the neural network output cut, the sub-samples used are different because the mass window serves to reject events which lie outside it. Table 5.1 summarises the effects of changing the mass window when varying the size of the ‘L’ shape plane (see Figure 5.7). The results are stable when varying the lower or upper limits of

Tail Region (GeV/ c^2)	Peak Region (GeV/ c^2)	N_{data}	Data fit (GeV/ c^2)	Expected Error (GeV/ c^2)
60 - 86	74 - 86	1097	80.539 ± 0.110	0.094 ± 0.007
60 - 86	60 - 86	1726	80.621 ± 0.109	0.096 ± 0.007
60 - 86	70 - 86	1125	80.553 ± 0.108	0.104 ± 0.007
50 - 86	74 - 86	1147	80.538 ± 0.111	0.093 ± 0.007
60 - 90	74 - 90	1302	80.570 ± 0.111	0.104 ± 0.007
50 - 90	74 - 90	1345	80.556 ± 0.108	0.095 ± 0.007
50 - 90	80 - 90	1105	80.227 ± 0.178	0.154 ± 0.011
50 - 90	65 - 90	1394	80.548 ± 0.109	0.100 ± 0.007

Table 5.1: The effect of varying the mass window cut on the data and expected error (as defined in Figure 5.8). The ‘L’ shape (m_1, m_2) plane means the upper bounds in each region are the same. The number of selected data events is also shown for each mass window configuration.

the mass window. Increasing the window size in this way allows more events to enter the mass fit, but the effect of higher statistics is compensated by the fact that these events have less sensitivity to the W mass. The most dramatic effect on the measurement is when the peak region is reduced in size⁵ (seventh row down in Table 5.1). The number of selected events using this mass window is almost the same as for the standard configuration. However, the BW signal distributions are only partially contained within this window and the decrease in accepted signal events is compensated by an increased acceptance for non- W^+W^- background events towards

⁵It should be stated *a priori* that this is not a ‘sensible’ choice of window, but more a check of the behaviour of the analysis in extreme configurations.

higher masses (see Figure 4.19). When reweighting the resulting *p.d.f.* as a function of the W mass the fit is less efficient, since the most sensitive region is around the peak of the BW's which are not fully contained. In this scenario it is then perhaps unsurprising that, along with a larger fit error, the central fit value changes by more than $300 \text{ MeV}/c^2$ from the optimal method. The effect of requiring a square mass window for both masses (second row) also adds no gain to the result despite an increased acceptance, due to most of the extra events being background.

5.6 Systematic Considerations

5.6.1 Finite MC Statistics

As discussed in Section 5.3, the finite number of Monte Carlo events used as a reference in the reweighting method contributes a systematic uncertainty to M_W . One way to evaluate the magnitude of this effect is to divide the reference into N_{samp} smaller samples of equal size. Each of these samples is then used as a reference sample, and the data fit repeated. The RMS of the fitted masses scales as the square root of the number of samples that the reference is divided into, shown in Figure 5.16. Applying this method to the reference sample used in the analysis at $\sqrt{s} = 183 \text{ GeV}$, the systematic error coming from the finite reference Monte Carlo statistics was estimated to be $20 \pm 5 \text{ MeV}/c^2$ using the 2-D reweighting method with the binning described in Figure 5.6 [89]. This method is simple to apply, but has the disadvantage of a relatively large uncertainty on the systematic error quoted. A more elaborate but equivalent method uses an analytical approach to calculate the systematic error due to finite statistics [85] (Appendix B). This method uses the fact that each bin in the 2 dimensional *p.d.f.* has a different sensitivity to the W mass as the reference is reweighted, and calculates the statistical error contribution from each bin. Using this method, the finite statistics systematic at $\sqrt{s} = 189 \text{ GeV}$ was calculated to be $10 \text{ MeV}/c^2$. By scaling this uncertainty to correspond to a sample of the same size as the data, it defines the expected error. This is a very efficient way to perform optimisation studies, for example the binning. It should also be noted that this systematic error should compensate for the non-linearities caused by binning, for example the calibration curves shown in Figure 5.5.

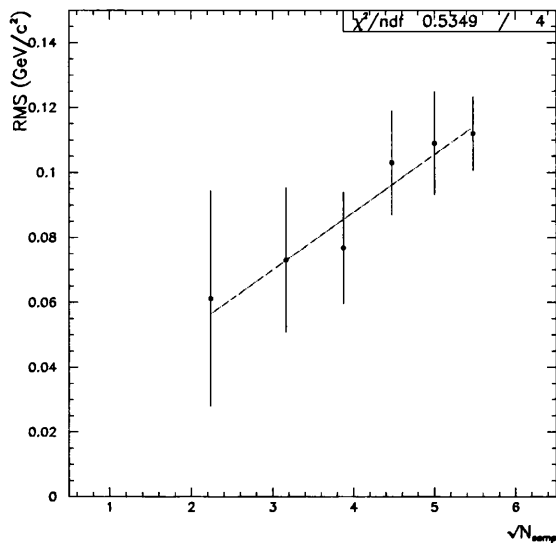


Figure 5.16: A straight line fit to the dependence of the R.M.S. to $\sqrt{N_{samp}}$ gives an estimation of the systematic error arising from the finite nature of the MC reference.

5.6.2 Fragmentation

In the measurement of the W mass from direct reconstruction of the $W^+W^- \rightarrow q\bar{q}q\bar{q}$ (and indeed the $W^+W^- \rightarrow q\bar{q}\ell\nu$) channel, hadronic jets are used to build the invariant mass distribution. It is therefore important that the fragmentation of partons into jets (see Section 2.4) is well simulated since the measurement makes a direct comparison between data and MC. The effects of fragmentation are complicated because the hadronisation model uncertainties are convoluted with the detector resolution and features of the analysis such as jetfinding and jet-pairing, for the hadronic channel. It is therefore of great importance to understand the effect of hadronisation model uncertainties on the W mass.

The JETSET model [35] contains a number of fragmentation parameters, which are tuned to large data samples recorded at the Z resonance [91]. These are listed in Table 5.2. One way of investigating the uncertainty on the W mass measurement coming from fragmentation is to vary these parameters and measure the shift in the W mass. This has been performed (using a fast simulation) for the measurement at $\sqrt{s} = 172$ GeV, by changing the parameters by $\pm 4\sigma$, and found to have a small effect on the W mass (~ 10 MeV/ c^2) [68]. This is perhaps unsurprising due to the

small uncertainties on these parameters, shown in Table 5.2.

Parameter	Description	Value
Λ_{QCD}	Relates to the QCD coupling constant α_s	$0.292 \pm 0.003(stat.) \pm 0.006(syst.)$
M_{min}	Invariant mass cut-off of parton showers	$1.570 \pm 0.040(stat.) \pm 0.130(syst.)$
σ_q	Gaussian width of p_T dist. for primary hadrons	$0.370 \pm 0.002(stat.) \pm 0.008(syst.)$
b	Free parameter in the LUND fragmentation function	$0.796 \pm 0.012(stat.) \pm 0.033(syst.)$

Table 5.2: The JETSET fragmentation parameters which are determined from data taken at the Z resonance. A brief description of their physical nature is given.

However, it is not certain that this is the correct way to estimate the real effects of fragmentation, as it assumes that the string model itself is correct. An alternative approach is to use a different fragmentation *model* and compare the two. The HERWIG model (see Section 2.4) provides an complimentary description of fragmentation to JETSET. To draw any conclusions from a comparison of these two models, it is important to first look at how well they describe reality, i.e. the data. Figures 5.17 - 5.19 show the agreement between data and MC which has been generated using the JETSET and HERWIG fragmentation models. The events in each sample are identical at the parton level and then fragmented with each model, further reducing any statistical contribution in the comparison. The HERWIG sample is fully simulated, rather than the fast simulation used in previous studies. The variables of interest are the ones input to the Neural Network, as in Section 4.1.3. Also, since the fragmentation has a large influence on the jet structure, the variables y_{34} and y_{45} are included (as defined in Section 4.2.1).

Both fragmentation models produce a similar signal which is well matched in data. It is interesting to note that the main difference between the models appears in the minimum jet mass variables (variables 12 and 13). The DURHAM P-E jetfinding algorithm uses massive jets, so is sensitive to the different jet structure produced by different fragmentation models. The y_{34} distribution, plotted as in terms of its logarithm for ease of comparison, does not show significant JETSET - HERWIG discrepancies, while a systematic shift in the y_{45} distribution is visible.

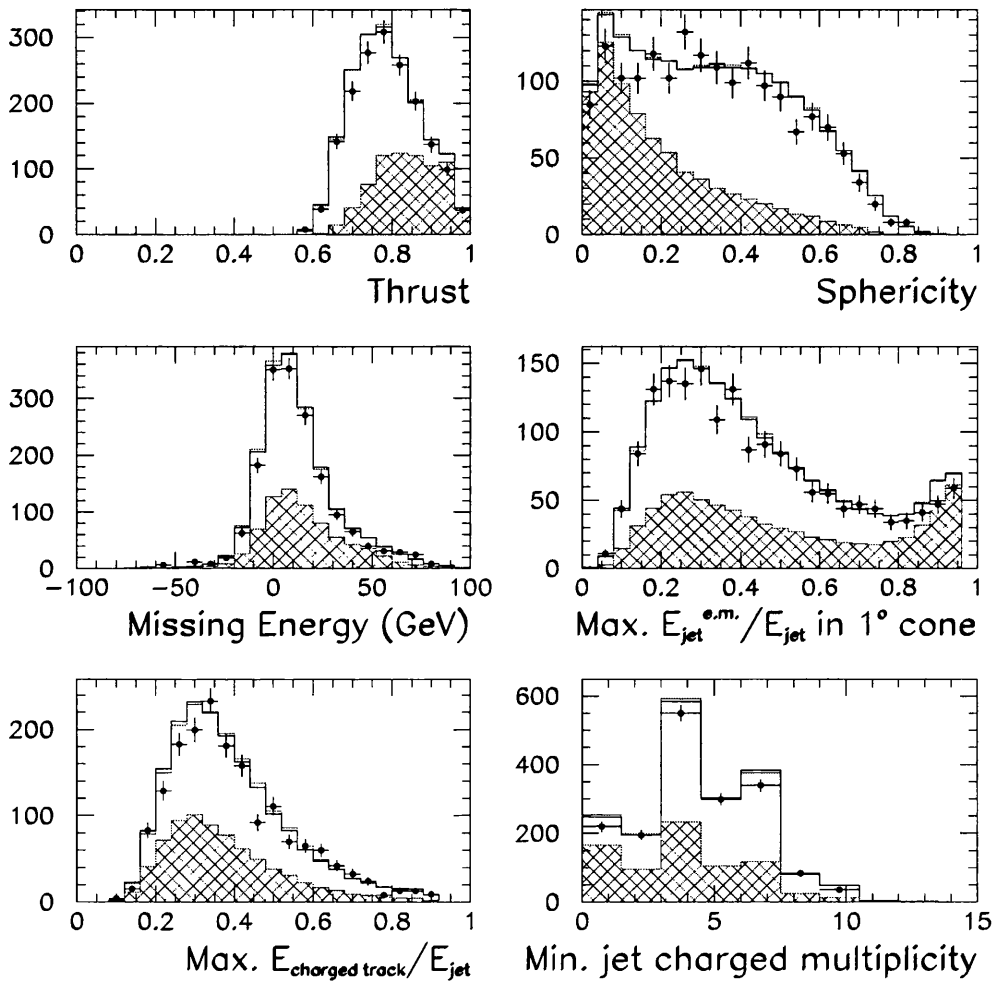


Figure 5.17: The agreement of data and MC which has been fragmented using JETSET (dashed histogram) and HERWIG (solid histogram) in NN14 variables 1-6 (normalised to the observed number of events). The filled histogram represents the non- W^+W^- background contribution and the data at $\sqrt{s} = 189$ GeV is shown by the points.

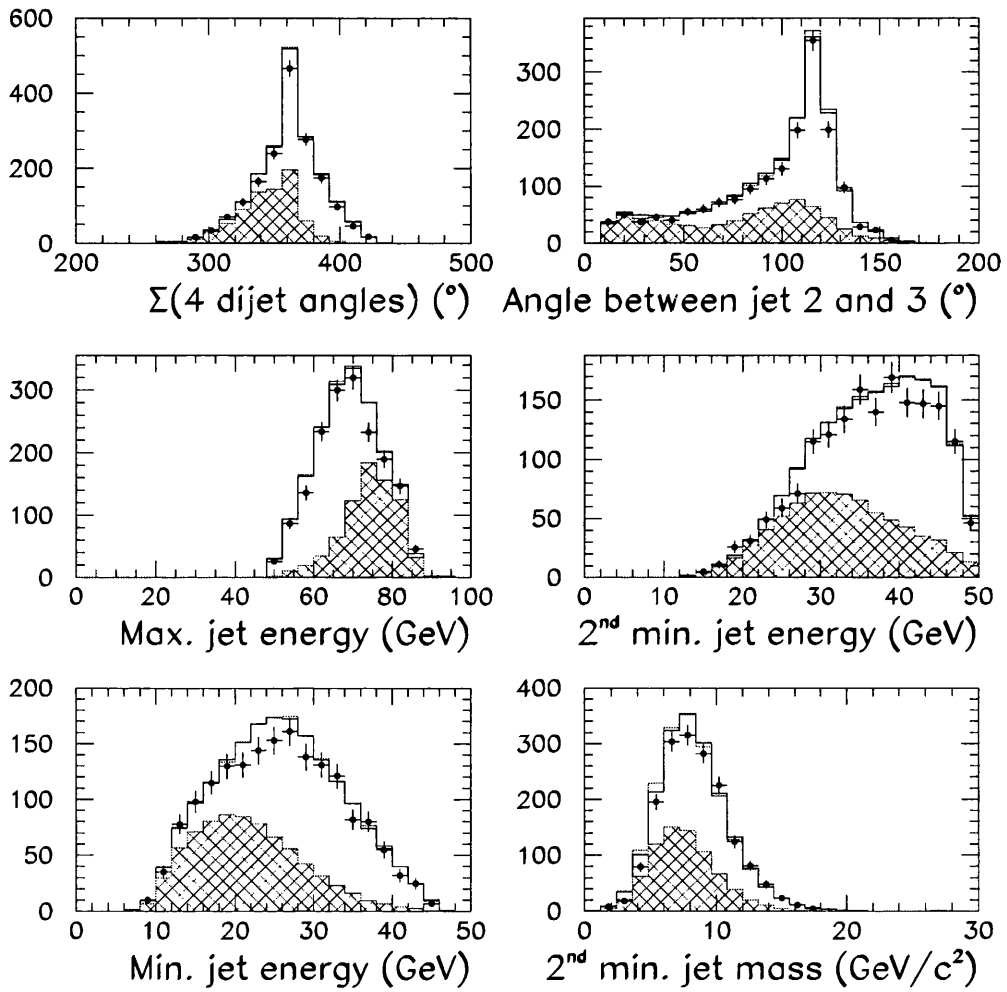


Figure 5.18: The agreement of data and MC which has been fragmented using JETSET (dashed histogram) and HERWIG (solid histogram) in NN14 variables 7-12 (normalised to the observed number of events). The filled histogram represents the non- W^+W^- background contribution and the data at $\sqrt{s} = 189 \text{ GeV}$ is shown by the points.

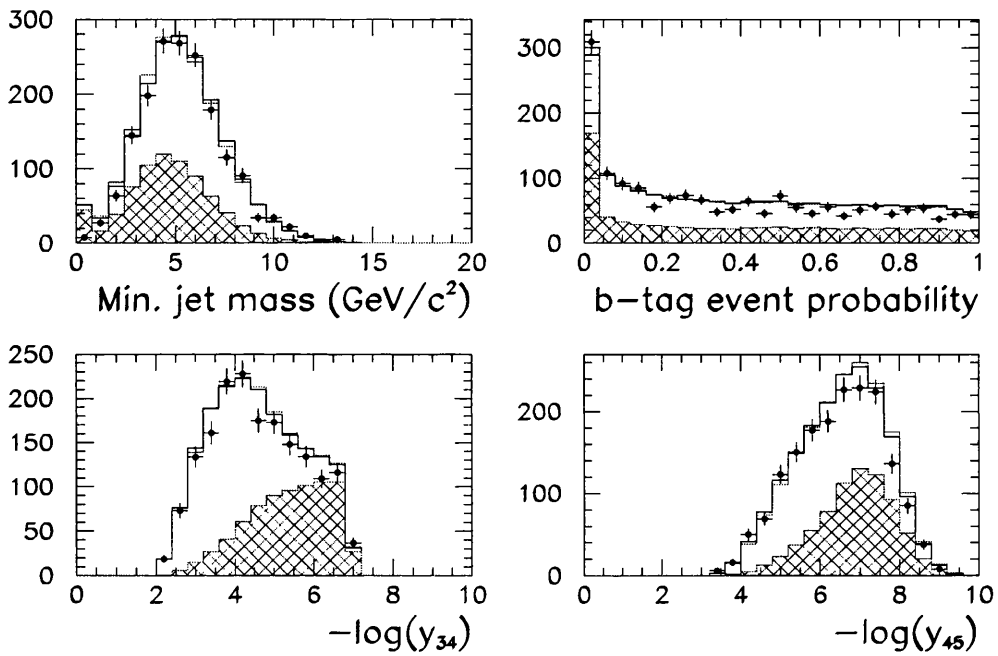


Figure 5.19: The agreement of data and MC which has been fragmented using JETSET (dashed histogram) and HERWIG (solid histogram) in NN14 variables 13 and 14 (normalised to the observed number of events). The filled histogram represents the non- W^+W^- background contribution and the data at $\sqrt{s} = 189$ GeV is shown by the points. The bottom two plots show the jetfinding variables y_{34} and y_{45} .

Since these variables depend strongly on the jet masses (see Equation 4.1), it is expected that they reflect the same behaviour as the JETSET - HERWIG discrepancies in variables 12 and 13. A possible reduction of this effect could be from the fact that the jet masses are scaled with the jet energies.

In addition, the correlations between the NN14 variables have been studied using the two models. The HERWIG correlation between the NN14 variables has been subtracted from the corresponding JETSET correlation to give the results shown in Figures 5.20 and 5.21. The main point to note is that the differences in the correlations between JETSET and HERWIG are ~ 10 times smaller than the data - MC discrepancies in Figures 4.10 and 4.11, and therefore both models can be treated as equivalent as far as the correlations in the data are concerned. Despite the small differences, this study provides further evidence that minimum jet masses are relatively badly matched between the two fragmentation models. Another variable that is sensitive to fragmentation is the jet charged multiplicity (variable 6), which also has badly matched correlations.

Observing that within the limited statistics both JETSET and HERWIG describe the data equally well, a comparison of the W mass measurement using each model is a valid approach to assign a physically meaningful systematic error to the W mass. Fitting sub-samples built from JETSET and HERWIG MC, to the original (JETSET) reference used for the W mass measurement provides a $\Delta M = M_{JETSET} - M_{HERWIG}$ with a high precision. Equivalently, sub-samples built from the original (JETSET) reference have been fitted to references built from both JETSET and HERWIG. This is not an ideal approach since in this case it means the reference is smaller, but is more a cross check of the method. Figure 5.22 shows the sample-by-sample fitted mass differences using these methods. The resulting systematic shifts are -16 ± 12 MeV/ c^2 when using the first method, and $+29 \pm 15$ MeV/ c^2 with the second. The larger spread in the mass difference when using the second method is largely due to the reduced size of the reference sample. The two mass shifts are compatible and their signs consistent with the fact that the method is reversed. The data has also been fitted to the two reference samples, and the difference is: $M_W^{JETSET} - M_W^{HERWIG} = +11$ MeV/ c^2 , again consistent with the shifts seen in MC studies. The final systematic error on the W mass due to fragmentation is taken to be $\Delta m_{frag} = 16$ MeV/ c^2 , as this method is considered the more robust and precise.

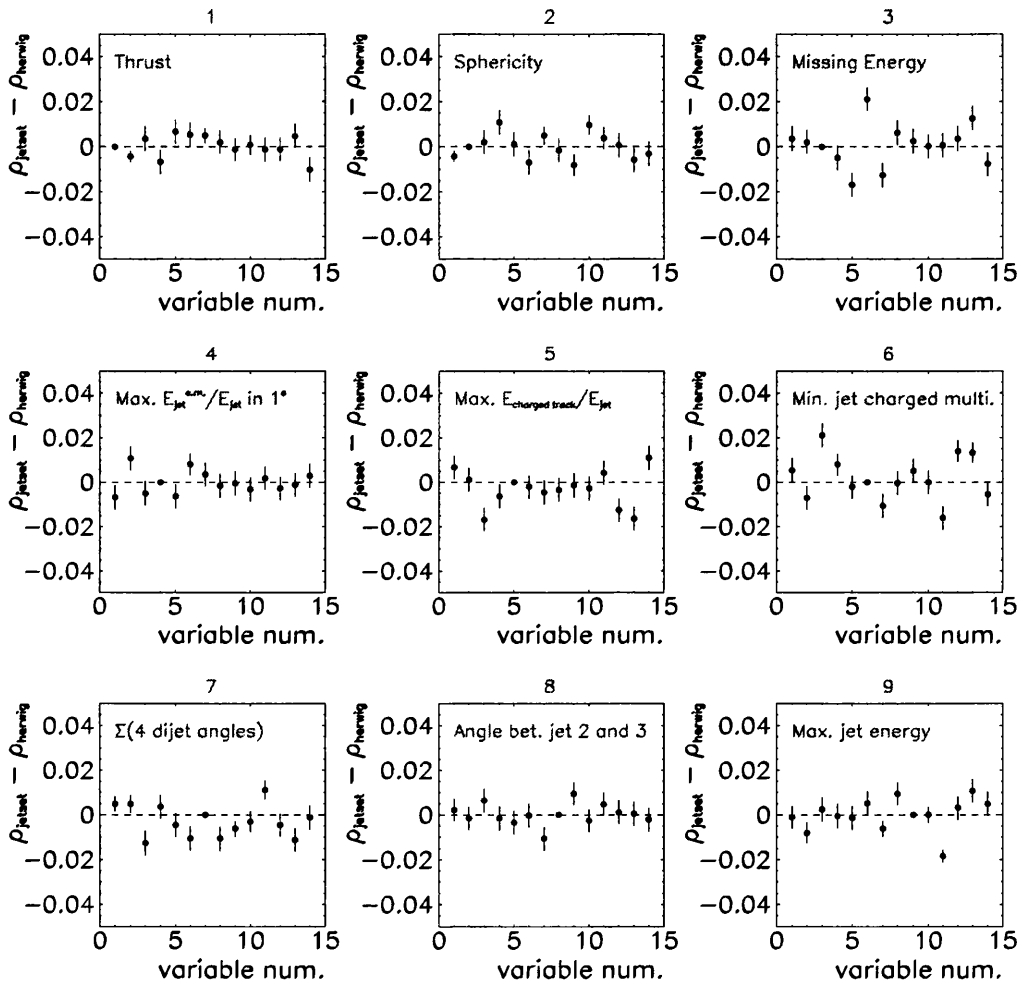


Figure 5.20: The JETSET-HERWIG difference in correlation coefficient between neural network variables 1 - 9. Each variable is shown with its correlations with all other variables, hence the difference in ρ is zero for correlations with itself.

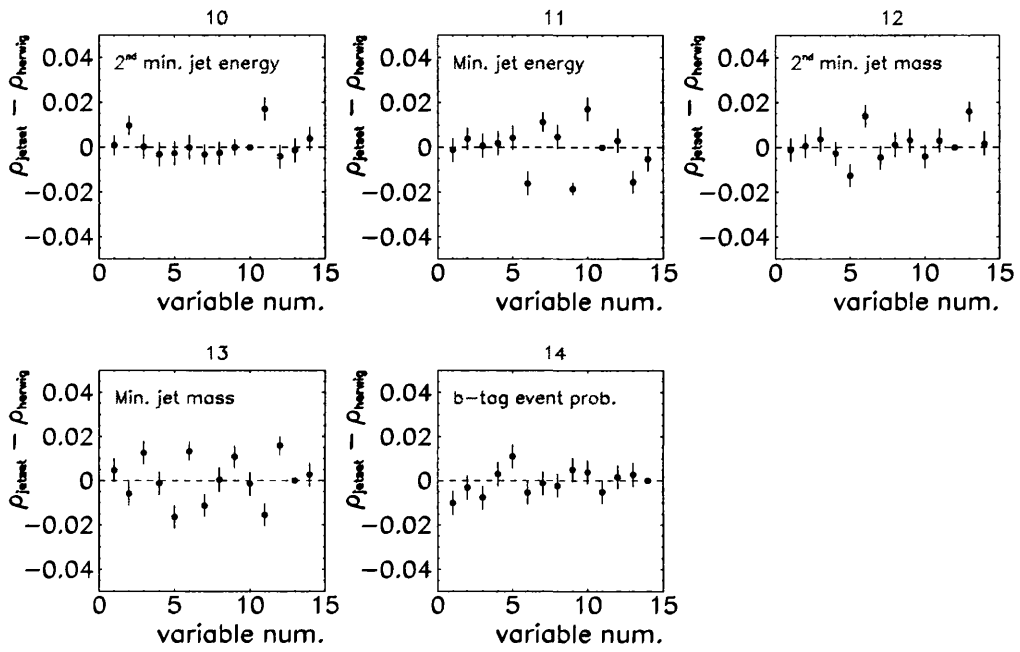


Figure 5.21: The JETSET-HERWIG difference in correlation coefficient between neural network variables 10 - 14. Each variable is shown with its correlations with all other variables, hence the difference in ρ is zero for correlations with itself.

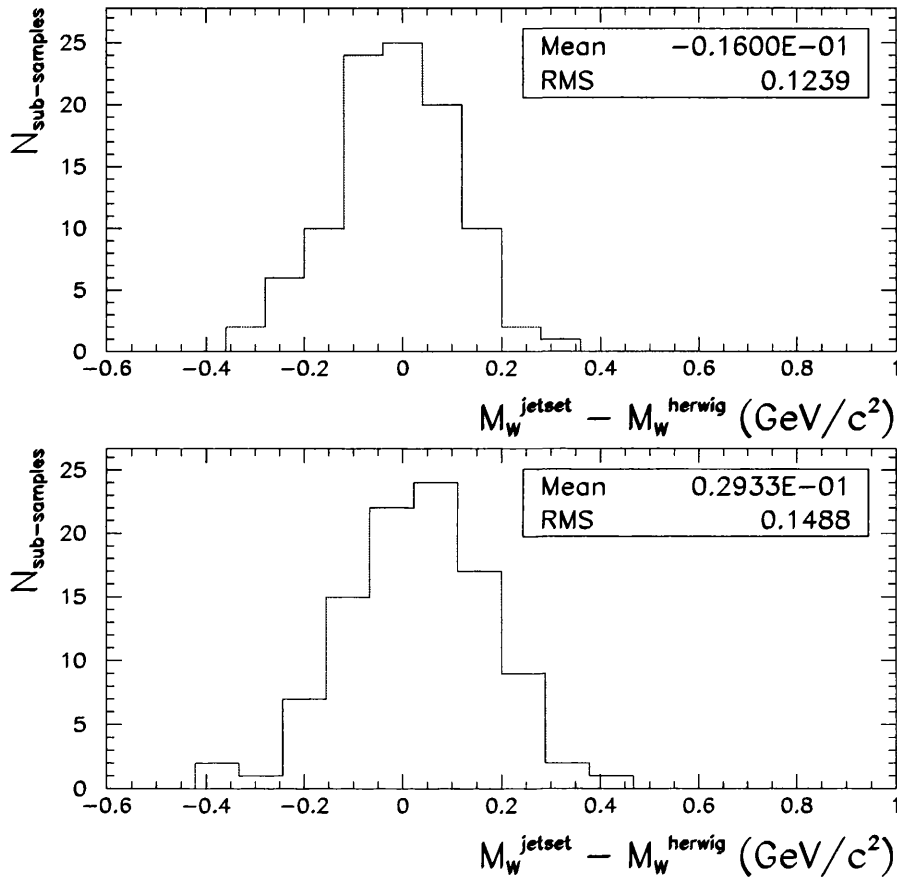


Figure 5.22: The difference in the fitted W mass between sub-samples built from JETSET and HERWIG (top). The bottom plot shows the reverse side of the study, where the same sub-samples have been fitted to a JETSET and HERWIG reference. In both cases, 100 sub-samples of the same size as the data have been fitted.

5.6.3 Summary of systematics

Below, other systematic effects of importance to the W mass measurement are described and how their magnitudes are estimated. Table 5.3 summarises the preliminary systematics for the ALEPH W mass measurement at $\sqrt{s} = 189$ GeV [79].

- **Calorimeter Calibrations** The uncertainty in the energy calibration of the electromagnetic and hadronic calorimeters has been estimated as $\pm 0.9\%$ and $\pm 2\%$, respectively [92]. The energy flow objects (see Section 3.6.3) formed with the data are varied by these amounts and the corresponding mass shifts added in quadrature to give the systematic error. Due to the fact that the effect is determined from the data it is subject to statistical fluctuation.
- **Jet Corrections** The corrections applied to the jets before the kinematic fit to account for detector losses are parameterised by the function shown in Figure 4.16. This correction function is varied by $\pm 1\sigma$ and applied to the jet energies of the data. The systematic uncertainty on the W mass measurement due to the jet corrections is taken to be the largest mass shift from zero when fitting the data with these modified jet energies [92].
- **Initial State Radiation** The MC used in the analysis (KORALW [61]) calculates QED initial state radiation up to second order in α . The effect of missing terms from this approximation is estimated by weighting each event in a specific KORALW sample with the ratio of first to second order squared matrix elements. The weighted events are then fitted in the same way as the data and compared to that from *unweighted* events. The systematic error on the W mass from ISR is taken to be this mass difference.
- **Background Contamination** The hadronic channel has a high non- W^+W^- background ($\sim 15\%$), thus it is important that it is correctly simulated in MC. The size of the data sample is not large enough to allow a detailed data/MC study, and a method using Z peak data has been applied [93]. High statistics Z data are compared to $q\bar{q}$ MC to determine discrepancies in the background shape and normalisation. These are then applied as correction factors to the

background *p.d.f.* in the W mass analysis to estimate the systematic uncertainty on the W mass.

- **LEP Beam Energy** The error on the beam energy translates directly onto an error on the W mass (as illustrated in Equation 3.1). The beam energy measurement itself is an enormously sophisticated process, taking into account subtleties such as the phase of the Moon and the water level in Lake Geneva. The error on the 1998 beam energy measurement at $\sqrt{s} = 189$ GeV [47] is dominated by the uncertainty in extrapolating RDP measurements at low energies to physics energies, which is described in detail in 3.2.2.

- **Colour Reconnection** The colour reconnection (CR) effect, described in Section 2.5.1, has been studied using variants of the parton evolution schemes in JETSET, ARIADNE [94] and HERWIG. Assessing the effects of these models is difficult because the strengths of the interconnection effects between quarks in the parton shower are completely model-dependent and based largely on probabilities or criteria which are not fully understood. The systematic error is taken to be the difference between the fitted masses of the reconnected and unreconnected MC sample. It is found that none of these models produces a significant effect on the the W mass when applied as recommended by the authors, and the mass shifts are statistically dominated. The systematic error assigned to the ALEPH W mass measurement at $\sqrt{s} = 183$ GeV (which is assigned also to the measurement described in this thesis) was estimated using the JETSET MC.

A single W^+W^- sample was generated which was then hadronised into one sample with no CR and three others labelled I, II and II', as defined in Section 2.5.1. The mass shift was taken to be the one from model I, using a reasonable reconnection probability of $\mathcal{P}_{reco} > 0.3$ in Equation 2.35. This cut removes 60% of the MC sample and was found to have a $+25 \pm 21$ MeV/ c^2 effect on the W mass [85].

- **Bose Einstein Effect** Two methods have been applied to determine possible bias from the Bose Einstein (BE) correlations between the W decay

products [85]. The first is based on the weighting technique as described in Section 2.5.2, which assigns a BE weight to each event that depends on the proximity of like-sign particle pairs in the final state. Comparing mass fits from this and a sample with no BE correlations, a shift of $-40 \pm 25 \text{ MeV}/c^2$ is observed. The second approach uses events generated with a fragmentation model which describes BE correlations as shifts in like-sign boson momenta, whilst ensuring energy and momentum conservation. The BE effect was estimated by comparing two samples; one which restricts to correlations between particles from the same W and the other which allows correlations between different W 's. The mass shift between the two is $-50 \pm 25 \text{ MeV}/c^2$, which is taken to be the systematic error on the W mass.

Source	Error (MeV/c^2)
Correlated errors	
Fragmentation	16*
Detector calibration	30
Jet corrections	8
Initial State Radiation	10†
LEP energy	17
Uncorrelated errors	
Reference MC Statistics	10*
Background contamination	10†
Colour reconnection	25†
Bose-Einstein effects	50†
Total	70

Table 5.3: Summary of the correlated and uncorrelated systematic errors on M_W . The *'s indicate systematic errors which have been calculated as part of the work in this thesis, while the other are from the official ALEPH result in [79]. The †'s indicate systematic errors which were evaluated for the W mass analysis at $\sqrt{s} = 183 \text{ GeV}$ [70].

Correlated systematics are those which also affect the other W decay channels in which the mass was also measured. Of the systematics particular to the hadronic analysis, the largest is that from colour reconnection and Bose Einstein effects. This results in the W mass measurement in the hadronic channel being considerably deweighted in the final ALEPH W mass result.

5.7 Chapter Summary

The application of a 2 dimensional fit to the data invariant mass distribution has been optimised to make a measurement of the W mass in the $W^+W^- \rightarrow q\bar{q}q\bar{q}$ channel. Although the improvement over a 1-D method is minimal, this is the correct approach because it naturally incorporates the full event-by-event correlation between the di-jet masses. The systematic implications of applying a Monte Carlo reweighting technique in 2-D have been understood, and led to the development of an optimal binning algorithm. Using this, the statistical error on the W mass has been checked by studying the magnitude and linearity of the expected error. The measurement has been shown to be stable against changes in the event selection, the bin size and the mass window. These studies have been complemented with a measurement of the systematic error on the W mass due to the finite statistics in the MC reference sample. A detailed study has been performed on the systematic effects on the W mass due to fragmentation and a summary of all other systematic considerations given.

The W mass measured from the $W^+W^- \rightarrow q\bar{q}q\bar{q}$ channel at $\sqrt{s} = 189$ GeV is found to be:

$$M_W = 80.556 \pm 0.110(\text{stat.}) \pm 0.039(\text{syst.}) \pm 0.056(\text{F.S.I.}) \pm 0.017(\text{LEP}) \text{ GeV}/c^2,$$

which includes the additional $27 \text{ MeV}/c^2$ to compensate for the fixed W width used in the Monte Carlo (as discussed in Section 2.3.2). The official ALEPH result which was presented at the winter (and summer) conferences this year [79] is:

$$M_W = 80.561 \pm 0.116(\text{stat.}) \pm 0.050(\text{syst.}) \pm 0.056(\text{F.S.I.}) \pm 0.017(\text{LEP}) \text{ GeV}/c^2,$$

which differs from the result in this thesis due to a different pairing algorithm with a slightly lower efficiency. The larger systematic error on this measurement is due to the fragmentation systematic error, which was calculated to be $35 \text{ MeV}/c^2$.

The issues discussed in this chapter concerning the binning of the *p.d.f.* have motivated the investigation of unbinned fitting methods⁶. One such technique, using the Kolmogorov Smirnov test, is the subject of the next chapter.

⁶See for example competitive results using a method which fits an analytical function to the invariant mass distribution [95].

Chapter 6

Kolmogorov Smirnov Test

Section 5.3.1 explained the effect of binning the probability distribution function on the measurement of M_W . This was shown to be due to the finite statistics in the MC reference sample, which is enhanced when fitting in two dimensions and due to the fact that the *effective* number of events in the reference is reduced the further it is reweighted. To limit this effect it is desirable to use large bins, particularly in the tails, but this is performed at the expense of the statistical precision on the W mass. To eliminate possible bias from binning, an *unbinned* fitting technique has been applied using a two dimensional Kolmogorov-Smirnov (KS) test.

6.1 KS Test Principle

The standard method for parameter estimation is that of maximum likelihood, which has the advantage that it will always find a best fitting model. The problem is that the best fitting model may not in fact fit very well. The Kolmogorov Smirnov (KS) test is an ‘absolute’ statistical test, in the sense that it provides a numerical measure of the goodness of fit when comparing two distributions. The one-dimensional KS test is used widely but in > 1 dimension it is less well understood. This chapter describes the 2-D KS test in detail and investigates its merits for parameter estimation, namely the W mass measurement.

6.1.1 One Dimensional KS Test

The results of fitting two distributions using maximum likelihood or least squares are independent of the order in which the data are found experimentally. A fitting method which takes this into account therefore uses more information from the data. One such general test of fit is the Kolmogorov-Smirnov (KS) test, which is a simple test applicable to *unbinned* distributions of a single variable. Given n independent observations on the variable x an *ordered* sample is formed by arranging the observations in ascending order of magnitude, x_1, x_2, \dots, x_n . The cumulative distribution function for this sample is then defined by

$$S(x) = \begin{cases} 0 & x < x_1 \\ \frac{i}{n} & x_i \leq x < x_{i+1} \\ 1 & x \geq x_n, \end{cases}$$

which implicitly contains the correct normalisation. The KS test statistic D is defined as the largest absolute difference between the cumulative distribution functions of the two samples, illustrated in Figure 6.1.

$$D = \max\{|S(x) - P(x)|\}.$$

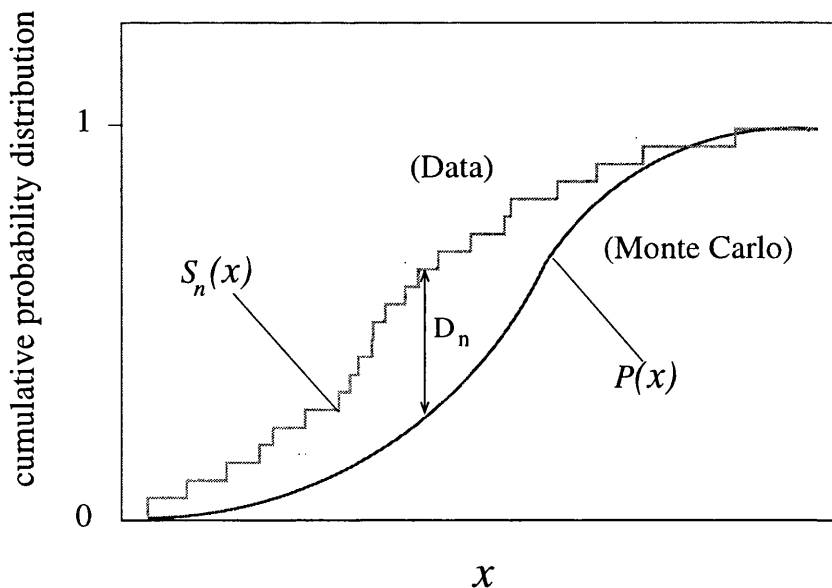


Figure 6.1: Testing the compatibility of two unbinned distributions using the Kolmogorov-Smirnov test statistic: $D = \max |S(x) - P(x)|$. $P(x)$ can either be a smooth theoretical curve or, as in this case, a large but finite data set (MC). Each step has height $\frac{1}{n}$ by construction.

The value of D is not however an absolute measure of the compatibility of the distributions $S(x)$ and $P(x)$, it has to be translated to a meaningful probability. The goal of a statistical test is to make a statement about how well the observed data stand in agreement with prediction, i.e. a *hypothesis*. More explicitly, it is a measure of the disproof of the ‘null hypothesis’, H_o (this is the case where the two samples under consideration are drawn from the same distribution, or theory). The 1D KS test can be shown [96] to be ‘asymptotically free’, meaning that for large N the result is independent of the nature of the parent population and theory. More explicitly, the distribution of D in the case of the null hypothesis is completely distribution-free, provided no parameter in $P(x)$ has been derived from the data distribution $S(x)$, thus giving the significance of any observed non-zero value of D . This comes from the simple nature of the test statistic D , which makes it invariant under any transformation of the variable x that preserves its order.

The significance level of an observed value, D_{obs} , (as a measure of the extent of disproof of the null hypothesis) is given approximately [97] by the formula:

$$\text{Probability}(D > D_{obs}) = Q_{KS}([\sqrt{N} + 0.12 + 0.11/\sqrt{N}]D), \quad (6.1)$$

where N is the effective number of data points in the two samples, $N = \frac{N_1 N_2}{N_1 + N_2}$. The function Q_{KS} is given by

$$Q_{KS}(\lambda) = 2 \sum_{j=1}^{\infty} (-1)^{j-1} e^{-2j^2 \lambda^2}, \quad (6.2)$$

which is the asymptotic distribution of D , approximately valid for $N \geq 80$.

6.1.2 KS Test in Two Dimensions

To apply the KS test to the two dimensional (m_1, m_2) plane for M_W we require a measure of the maximum cumulative difference between the two (m_1, m_2) planes. However, cumulative probability distributions are not well-defined in more than one dimension. A good alternative has been shown to be the integrated probability in each of four quadrants around a given point [98]. The two dimensional KS statistic then becomes the maximum difference between the observed and predicted normalised cumulative distributions, ranging over all data and MC points *and* their

quadrants (i.e. when *all* orderings of the data are considered). This construction thus provides information on the shapes of the two distributions. An illustration of the 2-D algorithm is given in Figure 6.2.

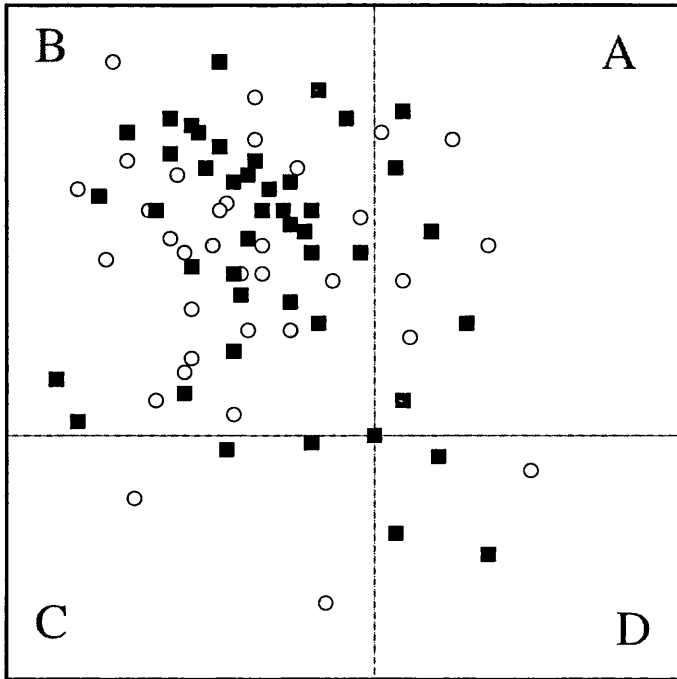


Figure 6.2: Two-dimensional distributions of 35 circles and 45 squares. The 2-D KS statistic D is the average of two ‘distance’ measures, $d1$ and $d2$. $d1$ is the maximum absolute difference between the number of circles and squares in each quadrant (A,B,C,D), ranging over all squares. $d2$ is the same but when ranging over all circles. Equation 6.3 then gives the probability that the circles and squares came from the same distribution.

The 2-D KS test is not as natural as its one dimensional parent because it is not rigorously true that the distribution of D in the null hypothesis is independent of the underlying two dimensional distribution. However, extensive Monte Carlo integrations have shown [99] that it is very nearly independent, provided the two samples have the same coefficient of correlation r . The distribution of D has consequently been parameterised in terms of r and N , and gives approximate significance levels for the 2-D KS test (c.f. Equation 6.1 for the 1-D test):

$$\text{Probability}(D > D_{\text{obs}}) = Q_{KS} \left(\frac{\sqrt{N}}{1 + \sqrt{1 - r^2}(0.25 - 0.75/\sqrt{N})} D \right), \quad (6.3)$$

where $r^2 = \frac{1}{2}(r_1^2 + r_2^2)$. A potentially serious limitation of this test arises from the extensive CPU time required, as it makes of the order N^2 operations for each fit. A

somewhat simpler generalisation of the one dimensional K-S has been proposed [99] which is faster by a factor of N yet maintains the same power as the ‘full’ (i.e. as described in the caption to Figure 6.2) 2D KS test. Instead of considering all N^2 points of the plane, only those N points where experimental data is found are considered (D is then taken to be d_1 as described in the caption for Figure 6.2). This is the algorithm used for the results presented here, and the effect of using this somewhat simpler construction will be discussed in Section 6.2.3.

6.2 Applying the KS test to Measure M_W

One of the most important things to decide before using a statistical test is exactly *what* you want it to tell you. The following sections address two distinctly different questions regarding the interpretation of the results to correctly measure M_W . Firstly (and trivially), we may ask the question ‘do the two distributions (i.e. data and MC) contain the information we require?’, and secondly, ‘what is the best estimator from these distributions and its uncertainty?’ [100].

The reconstruction procedure to build the two dimensional invariant mass distributions in data and MC used to extract M_W is the same as described in Chapter 4. The main point to note in some of the following plots is the ‘mass window’ selection cut, which removes events which have both masses (m_1, m_2) in the region $[60, 74]$ GeV/ c^2 . Figure 4.19 shows the 2-D distributions used to extract M_W at $\sqrt{s} = 189$ GeV along with their correlation coefficients.

6.2.1 The compatibility of data and Monte Carlo

The power of the KS test is that it can provide an ‘absolute’ measure of the compatibility of the two distributions under test, by transforming a simple statistic D into a probability. However, since this quantity is a measure of the disproof of the null hypothesis, we need to first find the distribution of D in the null hypothesis. This is the case where both $S(x)$ and $P(x)$ have been derived from Monte Carlo and is shown in Figure 6.3. The fraction of the synthetic D values that exceed D_{obs} , the value found in the data, is the significance of the test (~ 0.64). In other words, if we were to repeat the experiment many times, you would expect to find a worse

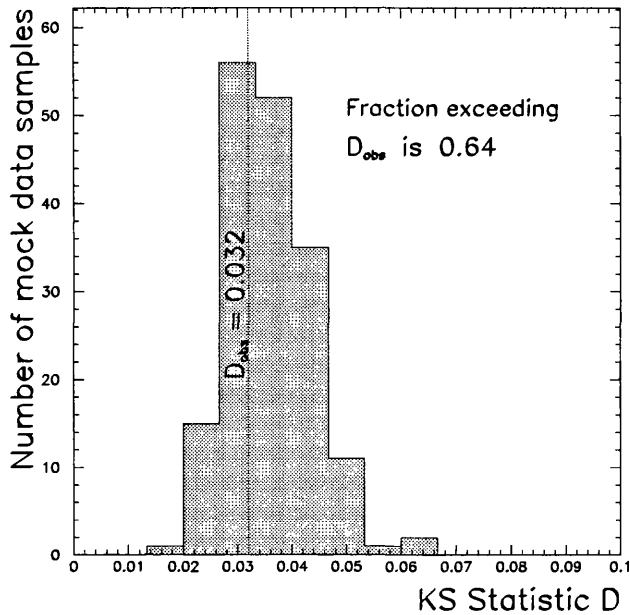


Figure 6.3: The distribution of D when fitting many Monte Carlo sub-samples of the same size as the real data set to the reference MC. D_{obs} (vertical line) is the value obtained when comparing the real data set with the MC.

fit to the data about 64% of the time. Using Equation 6.3 the significance level for D_{obs} is 0.48, which says the probability that the data and MC were drawn from the same underlying distribution is about 48%. This is different from the experimentally found value from Figure 6.3, which is due to assumptions in Equation 6.3. If the value of $P(D > D_{obs})$ had been perhaps $< 10\%$, there would be cause for concern in the modelling of the data. Here it is clear that this property of the KS test is most useful in situations where different models are tested, say, as being physical or non-physical, rather than finely adjusting a single parameter in an established theory (i.e. the Standard Model) as is being performed here.

The nature of D also allows the procedure of testing for fit to be reversed to use D to set confidence limits for a distribution as a whole. The critical value, d_α , of the KS statistic is defined as the value of D that has to be obtained in order to reach a certain confidence level (CL) α . This means a confidence band of width $\pm d_\alpha$ can be constructed around the empirical distribution with a probability $(1 - \alpha)$ that the true Monte Carlo distribution will lie *entirely* within this band [101]:

$$P(\{S_{DATA}(M_W) - d_\alpha\} < S_{MC}(M_W) < \{S_{DATA}(M_W) + d_\alpha\}) = 1 - \alpha .$$

For example, the critical value for the above case at $CL = 0.95$ is $d_{0.05} = 0.025$. Thus if the null hypothesis is tested at a significance level 95% then it should be rejected if $D_{obs} > 0.025$.

6.2.2 Estimating M_W

The KS test statistic D is minimised to find the best agreement between the data and reweighted MC distributions, thus to extract the best W mass estimator. By comparison with a χ^2 or log-likelihood method, which for large N gives a parabolic convergence curve (c.f. Figure 5.11), D is constructed by taking maximum absolute values of probabilities in quadrants on the (m_1, m_2) plane which are defined by the positions of the data and thus subject to fluctuations. This results in a very different convergence behaviour which is not necessarily smooth as a function of W mass (see Figure 6.4). When looking in detail at the quadrant probabilities which contribute to the final distribution of D as a function of M_W , it is seen that only a small number of data points drive the overall shape. In other words, a certain data point will produce the maximum value of D over a particular mass parameter range as the MC is reweighted. This produces a continuous D curve composed of series of different gradients which changes where the data point producing the maximum D (and therefore the definition of the quadrants) change. This is seen in Figure 6.4, with the corresponding data points driving the convergence listed in Table 6.1.

In the limit of low data statistics there are fewer data points which can define the quadrants maximising D ('points of sensitivity') and so a more simple structure. With larger data statistics there are more points of sensitivity but they are not necessarily close in mass which means the quadrant size varies more and different gradients are seen to make up the convergence curve. When large data sets are fitted there are many points of sensitivity to 'choose from' but they are closer in mass and so although the convergence curve is composed of different gradients, they are similar and so the curve is smoother overall (the gradients are less 'visible'). With the data statistics at $\sqrt{s} = 189$ GeV (1097 selected hadronic events), the fluctuations are clearly seen in the structure of the convergence of D . Table 6.1 contains the mass information corresponding to $D(M_W)$ as shown in Figure 6.4, and also the specific quadrants which contribute to the KS statistic. The variance in gradient over these

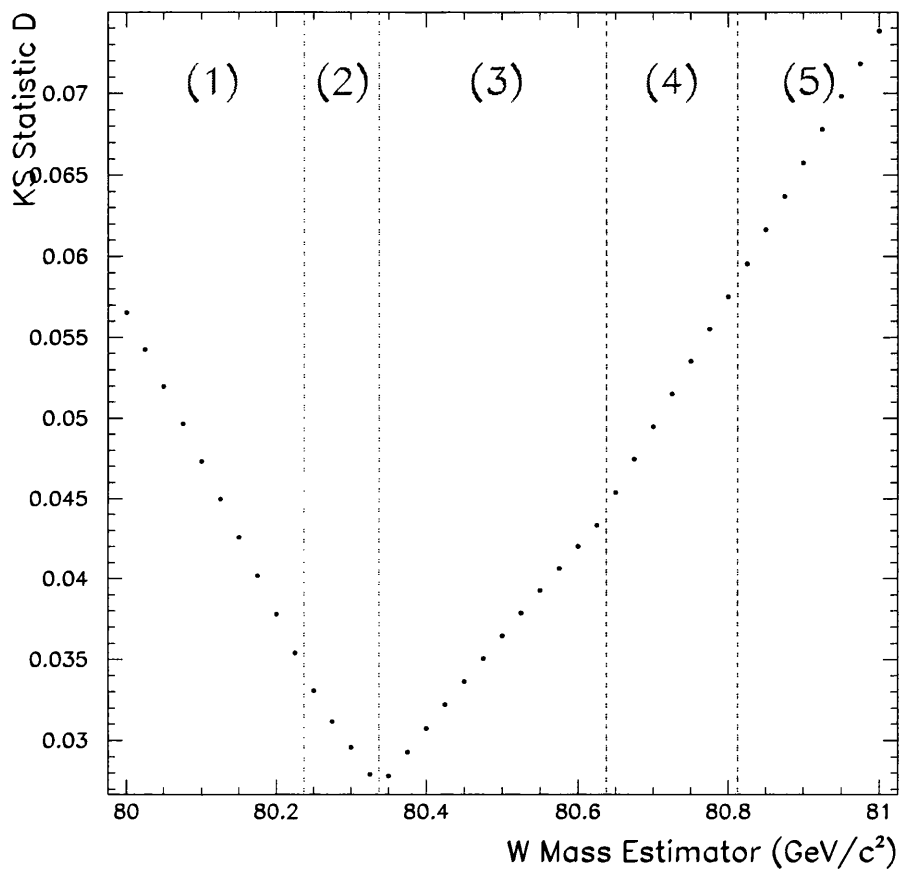


Figure 6.4: The behaviour of the KS test statistic D when fitting a synthetic data sample of the same size as the real data to a large MC sample that has been reweighted to correspond to 40 equidistant values of the M_W parameter. The vertical dotted lines mark regions where the same data mass coordinate has produced the maximum value of D . This is described in Table 6.1.

regions could be used to estimate the systematic uncertainty coming from the finite statistics of the reference sample.

Region	(m_1, m_2) Mass Coordinate (GeV/c^2)	Quadrant producing D
(1)	(80.969, 82.091)	A
(2)	(81.942, 83.768)	A
(3)	(79.583, 77.468)	C
(4)	(75.388, 80.135)	C
(5)	(74.324, 80.214)	C

Table 6.1: Data mass coordinates which define the quadrants producing maximal values of D over a certain mass range. It is clear that the closer the mass coordinates are at the point where they change, the less sharp is the change in gradient. Also, the quadrants most sensitive to the mass parameter are generally A and C, which makes sense when considering the change in the position of the peak as the MC is reweighted to from low to high W masses.

This behaviour is inherent to the KS test, because its sensitivity to deviations from the MC cumulative probability distribution $P(x)$ is not independent of x [97]. It is easiest to illustrate this with the 1D case, where the variance of the quantity $|S(x) - P(x)|$ (which is maximised to give D) is proportional to $P(x)[1 - P(x)]$, which is largest around the median value $P = 0.5$. This means that while the KS test is good at finding changes in the median value, it is not as good at finding *spreads*, which may affect the tails of the distribution while leaving the median unchanged¹. Figure 6.5 shows the sensitivity of the KS statistic to the W mass parameter.

Using a simple minimisation procedure the KS test statistic is found to converge rapidly to a value of $M_W = 80.423 \text{ GeV}/c^2$ when fitting the data at $\sqrt{s} = 189 \text{ GeV}$ to the Monte Carlo reference sample. However, it is not immediately obvious how to obtain the uncertainty on this value. In the limit of large N the methods of least squares or maximum likelihood allow Gaussian statistics to be used to estimate the standard error from each data sample fit (as described in Section 5.4). This approach is not directly² applicable to the 2D KS test for a single fit due to behaviour of $D(M_W)$.

¹Several variants on the KS test have been proposed which use a *weighted* statistic to get round this [102].

²The KS statistic may be transformed into a probability density which can then be used to build a likelihood function from which to extract M_W , but this requires a large amount of MC simulation [103].

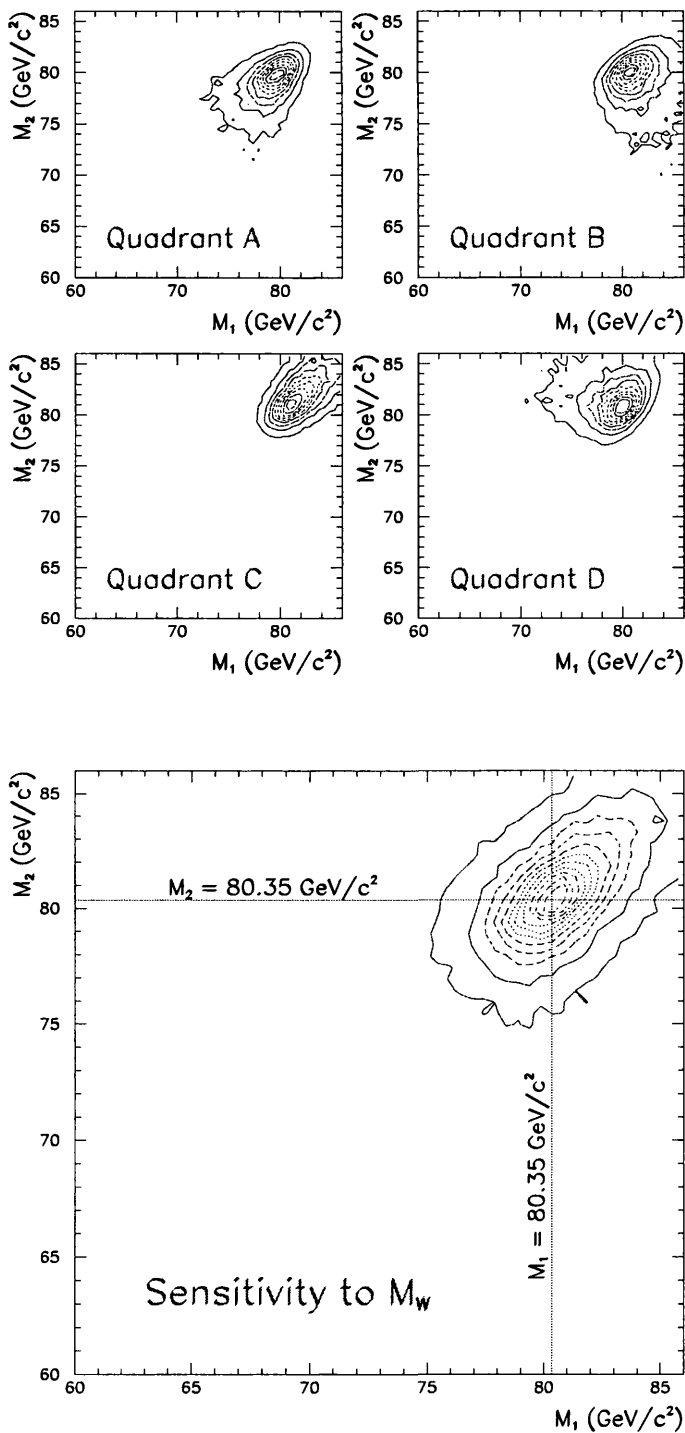


Figure 6.5: The sensitivity of the 2D KS test in each quadrant (top plots), and the sensitivity of the final statistic D to M_W . The contours show the difference in the components which make up D when reweighting over an M_W interval of 50 MeV/c². As expected the most sensitive region is around the reference mass value of $M_W = 80.35$ GeV/c².

A robust estimate of the statistical precision is obtained by considering the expected error. This is the RMS of the distribution of *fitted* masses when simulating many experiments using Monte Carlo sub-samples and is shown in Figure 6.6. The mean value is $80.39 \text{ GeV}/c^2$, which is two sigma higher than the the reference mass value $M_W = 80.35 \text{ GeV}/c^2$, and the expected statistical error the W mass is $0.160 \text{ GeV}/c^2$ (compare with the expected error from the maximum likelihood method, Figure 5.8). Using this MC approach the error on the data mass can be calculated from first principles. By determining the smallest region which contains 68% of the total number of events at different values of the *true* W mass parameter, a confidence belt can be set up around the *fitted* parameter which describes the mass region that you expect to contain M_W with a confidence level 68%. This is shown in Figure 6.7, which should be compared to the likelihood equivalent in Figure 5.12. The upper and lower confidence limits scale approximately linearly with the mass parameter which is expected since we are not near any physical boundaries.

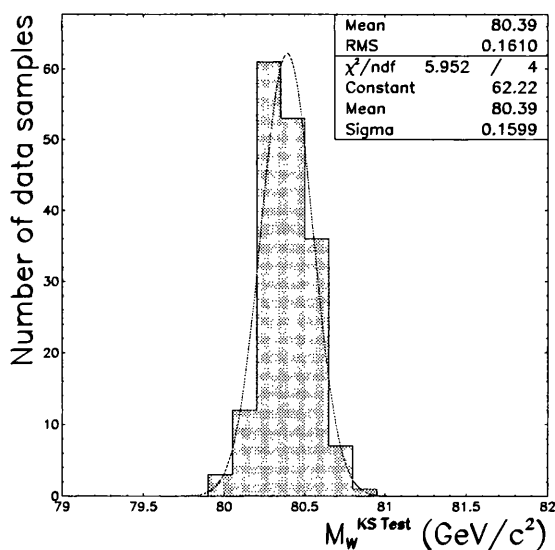


Figure 6.6: Distribution of masses from fitting 200 MC sub-samples to the entire reference MC sample. The RMS of this distribution is the statistical error on M_W .

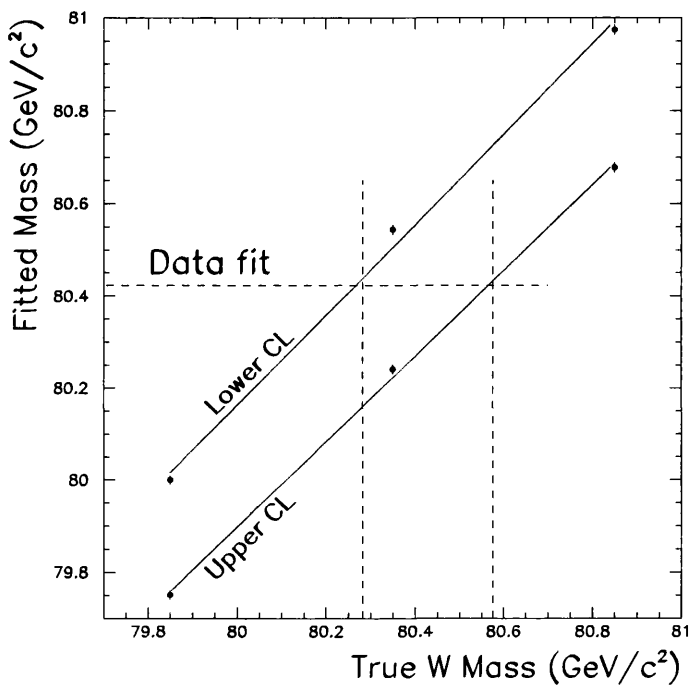


Figure 6.7: Calculating the statistical error from first principles. The smallest mass interval containing 68% of the total number of fit results defines $CL = 80.239$ and $CU = 80.554$ GeV/c^2 and thus an error of ~ 0.157 GeV/c^2 on the measured W mass parameter.

6.2.3 Stability Checks

To check any bias in the mass as a result of using the ‘fast’ 2D KS algorithm, 300 MC samples were fitted using both the ‘full’ and ‘fast’ algorithms. Figure 6.8 shows the difference in the fitted mass values and it is seen that the mean difference is consistent with zero.

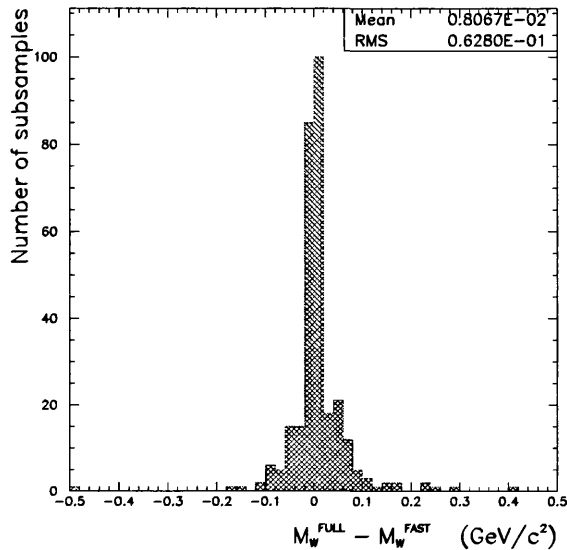


Figure 6.8: Difference in fitted masses when comparing the ‘full’ and ‘fast’ two dimensional KS algorithms.

To check if the 2D KS test is sufficiently ‘distribution free’, the correlation between D and M_W has been plotted, see Figure 6.9. The linearity of the fitting method has been checked through studying the response of the analysis to the M_W parameter and is shown in Figure 6.10.

6.2.4 Comparison with Likelihood Method

A likelihood method has been applied to the same synthetic data samples as used to calculate the expected error from the KS fit to compare the result. Figure 6.11 shows the difference in fitted mass when using the two methods and the correlation between them. The mean difference in fitted masses is negligible, although the RMS is relatively large, and the correlation between fitted masses is high, as expected. Using the likelihood to estimate the data mass value gives (Section 5.4.3) a W mass

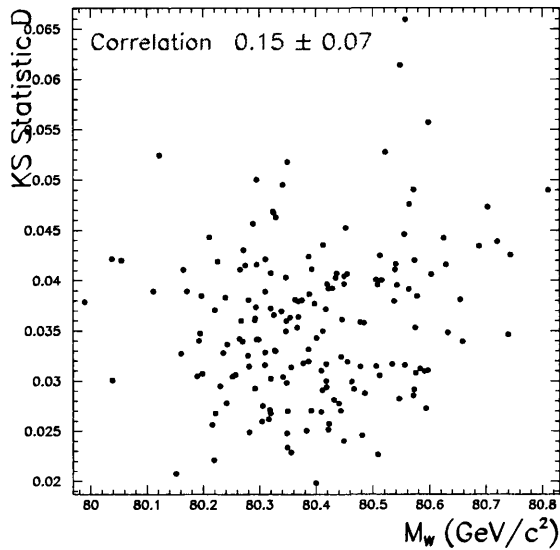


Figure 6.9: The dependence of D on the W mass parameter. The correlation between them is small which shows that the 2D KS test is approximately distribution free, partly owing to the observation that the (m_1, m_2) correlations are the same in data and MC.

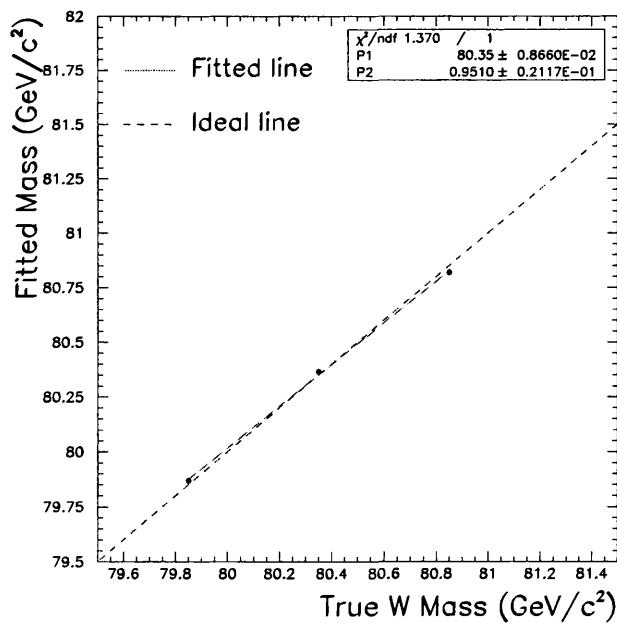


Figure 6.10: Response to M_W : The resulting calibration curve has a gradient $> 1\sigma$ from unity and an offset consistent with $80.35 \text{ GeV}/c^2$.

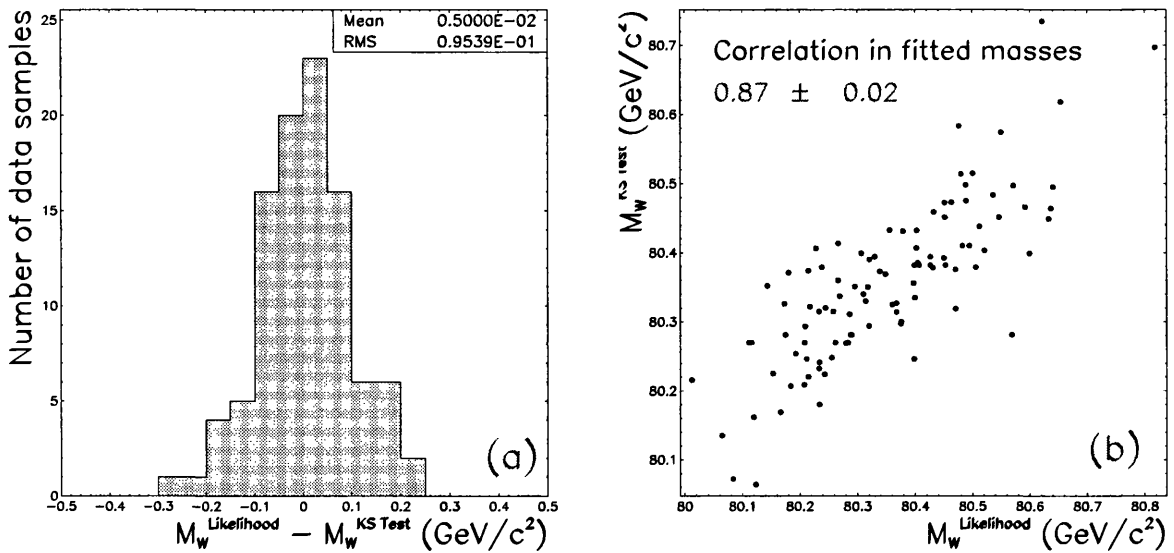


Figure 6.11: The result of fitting identical samples with likelihood and KS. (a) shows the difference between fitted masses and (b) the correlation between them.

estimate $M_W = 80.539 \pm 0.110 \text{ GeV}/c^2$, with KS probability 0.55 using the distribution of D found experimentally (Figure 6.3) and 0.39 using Equation 6.3. The difference in the fitted mass value between the KS likelihood extraction methods is large considering the high correlation between them, and the probability of obtaining this mass value is $\sim 10\%$ less likely than the estimate from the KS test.

6.3 Chapter Summary

In an attempt to minimise the effects of binning by making use of the information from each data event, a fitting technique using a two dimensional Kolmogorov-Smirnov test has been applied. The particular choice of a certain statistical test to measure the compatibility of two distributions affects the outcome of the test, and there is no standard or optimal definition of how to go about it. An ‘appropriate’ statistic should be used for the particular distributions under comparison, depending on their properties (i.e. their size, asymmetry, shape etc.). Using the 2D KS test the best W mass estimator in the hadronic channel at $\sqrt{s} = 189$ GeV is found to be

$$M_W = 80.423 \pm 0.160(\text{expected stat.}) \text{ GeV}/c^2,$$

and the probability of obtaining a worse fit than this is approximately 0.64. A likelihood fit for the same data gives a mass of $M_W = 80.539 \pm 0.110 \text{ GeV}/c^2$ which has ~ 0.1 less probability than the KS test W mass estimator (calculated by finding the KS significance of the likelihood mass estimator). It is widely known that for small samples the KS test is particularly efficient at comparing two distributions as it does not throw away any information contained in the data. However, its use for parameter estimation are less well known, as although it is very sensitive to the median of a distribution it is less responsive to the tails, which for the case of the extraction of the W mass which contain distorted Breit Wigners is clearly important.

While the Kolmogorov Smirnov test has some attractive features, for example being able to provide an absolute measure of the compatibility of two 2 dimensional distributions, it is not as efficient for parameter estimation as the method of maximum likelihood. Perhaps if the test had been applied to previous years’ data, where data statistics were much lower, the results would have been competitive with the likelihood method. However, it is an excellent cross check of the analysis currently used in ALEPH for the hadronic mass measurement and favours the current world average W mass measurement of $M_W = 80.394 \pm 0.042 \text{ GeV}/c^2$ (see Section 7.4).

Chapter 7

Combination of W Mass Results

7.1 ALEPH W Mass Measurement

The ALEPH measurements of the W mass from direct reconstruction in the $W^+W^- \rightarrow q\bar{q}q\bar{q}$ channel at previous LEP centre of mass energies are shown in Table 7.1, along with the measurement described in this thesis ¹.

LEP Energy (GeV)	M_W (GeV/ c^2)	$\pm\sigma_{stat.}$	$\pm\sigma_{syst.}$	$\pm\sigma_{FSI}$	$\pm\sigma_{LEP}$
172 (final)	81.300	0.470	0.080	0.064	0.030
183 (final)	80.461	0.177	0.045	0.056	0.021
189 (preliminary)	80.561	0.116	0.050	0.056	0.017

Table 7.1: Summary of ALEPH W mass measurements from direct reconstruction in the $W^+W^- \rightarrow q\bar{q}q\bar{q}$ channel made at previous LEP centre of mass energies.

The combined measurement, presented at the international summer conferences: ‘HEP99’, Tampere, Finland [79], is:

$$M_W^{4q} = 80.561 \pm 0.095(stat.) \pm 0.050(syst.) \pm 0.056(F.S.I.) \pm 0.017(LEP) \text{ GeV}/c^2,$$

where the systematic errors from FSI and the LEP beam energy are quoted separately for the purpose of combining this result with other decay channels. ALEPH measurements from direct reconstruction in the $W^+W^- \rightarrow q\bar{q}\ell\nu$ channel at $\sqrt{s} = 172 - 189$ GeV, including a new measurement using the $W^+W^- \rightarrow \ell\nu\ell\nu$ channel at $\sqrt{s} = 183$ GeV [10], combine to give

¹The ALEPH result is the same as was presented at the 1999 Winter (and Summer) Conferences and is slightly different to the measurement described in this thesis due to improvements made since then, as discussed in Section 5.7.

$$M_W^{non-4q} = 80.343 \pm 0.089(stat.) \pm 0.038(syst.) \pm 0.017(LEP) \text{ GeV}/c^2.$$

The measurements of M_W^{4q} and M_W^{non-4q} at each LEP centre of mass energy are combined, taking into account all correlations between different channels and different years. The resulting M_W^{4f} average, together with the measurement derived from the W^+W^- cross section at $\sqrt{s} = 161 \text{ GeV}$ [104], combine to give the current (preliminary) ALEPH W mass measurement:

$$M_W^{Alep} = 80.411 \pm 0.064(stat.) \pm 0.037(syst.) \pm 0.022(FSI) \pm 0.018(LEP) \text{ GeV}/c^2.$$

The large systematic from FSI deweights the hadronic channel measurement considerably, reducing the FSI uncertainty to $22 \text{ MeV}/c^2$ on the combined 4- f mass measurement. The mass measurement from the W cross section has only a small weight compared to the measurements from direct reconstruction.

7.2 LEP W Mass Combination

Excluding the measurement using the $W^+W^- \rightarrow \ell\nu\ell\nu$ channel, the other LEP experiments have made parallel measurements of the W mass. For the hadronic channel, OPAL [105] and L3 [106] also use the technique of Monte Carlo reweighting to extract the W mass, but fit each mass separately (1-D reweighting). To pair the jets, both experiments make a cut on a likelihood function built from the difference in the di-jet masses and the χ^2 probability coming from a 5C kinematic fit². The DELPHI Collaboration uses a more sophisticated analysis which allows five-jet as well as 4-jet to be included [107]. For each event all di-jet combinations are incorporated (a 5-jet event has 10 possible di-jet configurations) by performing a 4C kinematic fit for each combination and summing the corresponding two dimensional ideograms for each event. A likelihood is then built from the convolution of this with analytical expressions for the signal and background contributions, which means the method has to be calibrated. Table 7.2 summarises the 4 LEP experiments' preliminary measurements of the W mass in the hadronic channel at $\sqrt{s} = 189 \text{ GeV}$ [108]. The mass measurement in the $W^+W^- \rightarrow q\bar{q}\ell\nu$ channel is performed in a similar

²A 5C fit imposes energy and momentum conservation plus the additional constraint that the di-jet masses are equal, which produces one mass per event rather than two coming from 4C + rescaling.

Experiment	M_W (GeV/ c^2)	$\pm\sigma_{stat.}$	$\pm\sigma_{syst.}$	$\pm\sigma_{FSI}$	$\pm\sigma_{LEP}$
ALEPH	80.561	0.116	0.050	0.056	0.017
DELPHI	80.467	0.110	0.037	0.054	0.017
L3	80.610	0.126	0.072	0.092	0.017
OPAL	80.315	0.112	0.076	0.053	0.016

Table 7.2: Summary of LEP preliminary W mass measurements from direct reconstruction in the $W^+W^- \rightarrow q\bar{q}q\bar{q}$ channel at $\sqrt{s} = 189$ GeV for each experiment.

way for all four LEP experiments, although DELPHI allow for the possibility of more than two jets. A 2C kinematic fit is performed and the corresponding invariant mass distributions are fitted using 1-D MC reweighting. The combination of these measurements with those from the hadronic channel at $\sqrt{s} = 172 - 189$ GeV for all four LEP experiments, along with the threshold measurements, gives the following preliminary LEP W mass average [109]:

$$M_W^{LEP} = 80.350 \pm 0.056(stat. + syst.) \pm 0.025(LEP) \text{ GeV}/c^2.$$

Since effects from FSI are particular to the hadronic channel, it is interesting to look at the difference between the M_W^{4q} and M_W^{non-4q} measurements. Figure 7.1 shows this difference for each of the LEP experiments, where the quoted errors do *not* include the FSI systematic. The difference between the LEP hadronic and semi-leptonic W mass from direct reconstruction is

$$\langle M_W^{4q} - M_W^{non-4q} \rangle_{LEP} = 0.152 \pm 0.074(stat. + syst.) \pm 0.058(FSI) \text{ GeV}/c^2,$$

which with the present statistical precision is compatible with zero. With LEP data taken in 1999 and 2000, the precision on this difference will be high enough to determine its significance, which could indicate a bias in the hadronic mass measurement due to FSI. More importantly however, it is crucial to fully understand the FSI effects themselves, to ensure that the FSI systematic error is physically meaningful.

7.3 Tevatron Collider W mass Results

The Tevatron collider (Fermilab, USA) collides beams of protons and anti-protons, producing a centre of mass energy $\sqrt{s} = 1.8$ TeV. W bosons are produced predominantly by $q\bar{q}$ annihilation and are detected by their leptonic decays into electrons

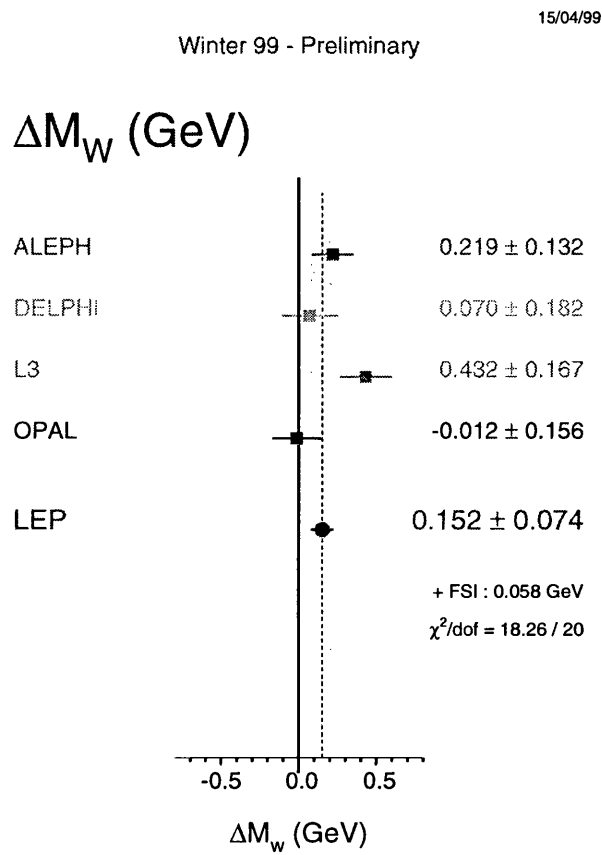


Figure 7.1: The difference $M_W^{4q} - M_W^{\text{non-}4q}$ for each LEP experiment, using mass measurements at $\sqrt{s} = 172 - 189$ GeV from direct reconstruction of the hadronic and semi-leptonic channels.

and muons with their corresponding neutrinos. The lepton momentum distribution and the transverse momentum of the neutrino, which is inferred by the large missing momentum of the event, are measured. The W mass is determined by direct reconstruction of the transverse mass distribution of the event. There is a large QCD background to discriminate against and the error on the W mass measurement is dominated by systematic uncertainties in the calorimeter energy scales and the modelling of the remnants of the proton decay (the event recoil). Preliminary results from the two experiments D0 and CDF are shown in Table 1.1, along with the W mass measurement made at UA2, which combine to give a preliminary hadron collider W mass average of [8]:

$$M_W^{pp} = 80.448 \pm 0.062 \text{ GeV}/c^2 .$$

The Tevatron collider is currently being upgraded to allow a higher data luminosity to be collected in future runs, and an error of $\sim 40 \text{ MeV}/c^2$ per experiment has been predicted [110].

7.4 Standard Model Constraints

The LEP W mass measurement is combined with measurements from $p\bar{p}$ colliders to form the preliminary world average direct W mass measurement [109]:

$$M_W^{direct} = 80.394 \pm 0.042 \text{ GeV}/c^2 ,$$

which is shown on the diagram in Figure 7.2. The indirect determination of the W mass is the result of a global electroweak fit through Equation 1.1, which has as input the precisely known Z mass measured at LEP1 and SLD; the value of $\sin^2 \theta_W$ measured at the neutrino-nucleon experiments CCFR [111] and NuTeV [112] and the measurement of the top quark mass from CDF and D0 . The value is

$$M_W^{indirect} = 80.381 \pm 0.026 \text{ GeV}/c^2 ,$$

shown in Figure 7.2. The direct and indirect measurements are in good agreement, which is shown in Figure 7.3 for various Standard Model predictions of the Higgs mass and currently favour a light SM Higgs. The consistency of the direct and

indirect measurements confirms that the SM is correct at the one-loop level. The direct W mass measurements, combined with all other experimentally determined SM parameters produces a χ^2 which sets the upper limit on m_H to $245 \text{ GeV}/c^2$ (95% CL), while the lower limit determined from direct Higgs searches is $m_H = 95.2 \text{ GeV}/c^2$ [109]. The preliminary SM prediction of the Higgs mass obtained is [4] $m_H = 81_{-42}^{+77} \text{ GeV}/c^2$ without the W mass measurement, and $m_H = 77_{-39}^{+69}$ with the direct W mass measurement, giving a reduction in statistical uncertainty of $\sim 10\%$ on the Higgs mass.

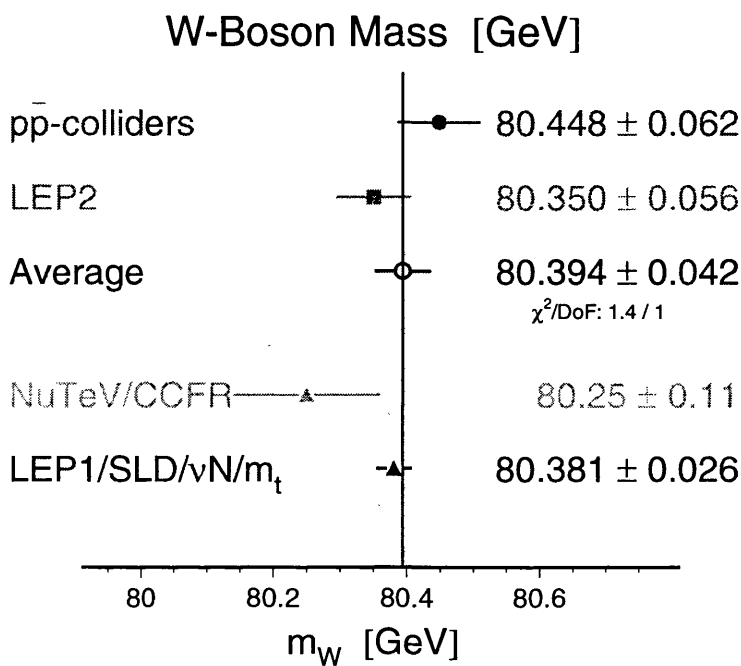


Figure 7.2: The LEP and hadron collider results combine to give the current preliminary world average W mass measurement from direct reconstruction. Also shown are the indirect measurements of the W mass, which are in agreement.

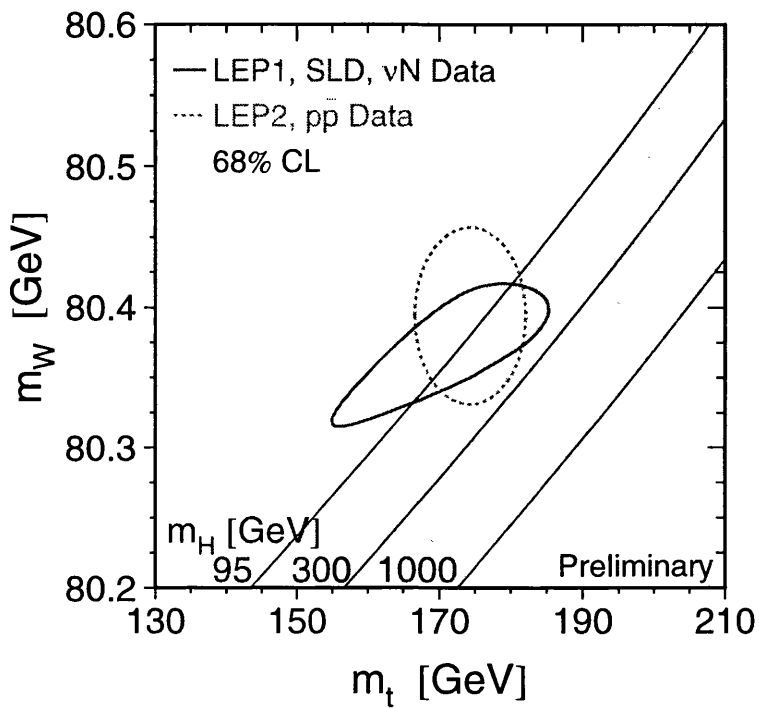


Figure 7.3: The regions defined by the direct and indirect measurements of M_W and the top quark mass, compared with the Standard Model prediction for different values of the Higgs mass (from $m_H = 95 - 1000 \text{ GeV}/c^2$).

Chapter 8

Summary and Conclusions

The direct measurement of the mass of the W boson is of fundamental physical importance since its value is predicted within the framework of our current understanding of the fundamental constituents of the universe, the Standard Model. A measurement of the W mass has been made in the $W^+W^- \rightarrow q\bar{q}q\bar{q}$ channel from data collected by the ALEPH detector during 1998 at $\sqrt{s} = 189$ GeV. The method of direct reconstruction of the invariant mass distribution of the W^+W^- decay products has been adopted, which is based on several analysis stages.

Due to a relatively high non- W^+W^- background, the most efficient way to select hadronic events is found to be a neural network (NN). Detailed studies of the variables used as input to the NN, namely their correlations and agreement between data and MC, have optimised this method in terms of efficiency and least mass bias. The selection efficiency using a 14 variable NN at $\sqrt{s} = 189$ GeV is 80% and the purity of the selected sample is 85%. The way in which the final state particles are clustered into jets has been optimised by studying the effect of different clustering algorithms on the measured W mass. The DURHAM-PE algorithm is found to produce the least mass bias and highest mass resolution, when studied at $\sqrt{s} = 172$ GeV, and has therefore been used in the analyses at subsequent centre of mass energies. A kinematical fit is used to impose energy and momentum conservation on each event, which leads to an improved invariant mass resolution. The resolution is improved further by rescaling the 4C masses by the corresponding jet energies, due to the use of additional information from the W^+ and W^- velocities. A jet pairing

procedure has then been applied to associate two di-jets to two W 's. The most efficient way to perform this is to categorise each combination by their CC03 matrix element weight and then use information from the di-jet angles and a mass window to select the correct di-jet pair. This event selection and reconstruction procedure has been performed for data and MC and used to build two dimensional invariant mass distributions in each.

The probability density function for the data sample to have a given invariant mass value is calculated by comparing the data to large reference MC sample which has been reweighted to correspond to many different values of the W mass. The reweighting is performed using the ratio of two matrix elements, calculated for the lowest order CC03 Feynman diagram contribution to $e^+e^- \rightarrow W^+W^-$ production and the identical treatment of data and MC leads to an unbiased W mass estimator. The W mass is taken to be the one which maximises a log-likelihood function built from these *p.d.f.*'s, and its value and error have been shown to be unbiased and in agreement with MC expectations. The application of the reweighting technique in two dimensions naturally includes the full event-by-event correlation between the di-jet masses in the *p.d.f.* The two dimensional binning of the *p.d.f.* has been the subject of detailed study, since the finite statistics in the reference MC sample has been shown to affect the measured W mass. Based on considerations of the linearity of the mass extraction method, the binning has been optimised and found to be stable with a minimum number of events per bin of 200. In addition the stability of the mass estimator and its error have been checked against variations in the NN selection cut and mass window.

The influence of binning on the measured W mass motivated a new technique for the mass measurement. The same reweighting method is used, but instead of maximising a likelihood function a two dimensional Kolmogorov Smirnov (KS) test has been applied. This produces an absolute measure of the goodness of fit between *unbinned* data and reweighted MC distributions. The uses of the 2-D KS test for parameter estimation are little known, and a complete study of the statistical behaviour of the test showed that the method is not as efficient as that of maximum likelihood. The W mass measured using this technique was found to be

$$M_W = 80.423 \pm 0.160(\text{stat.}) \text{ GeV}/c^2 ,$$

in agreement with that from maximum likelihood, and is considered an important cross check of the W mass analysis employed by ALEPH .

Systematic uncertainties on the W mass measurement have been discussed, with a detailed description of the systematic error due to fragmentation and the finite reference sample statistics. The W mass from the $W^+W^- \rightarrow q\bar{q}q\bar{q}$ channel is measured to be

$$M_W = 80.556 \pm 0.110(\text{stat.}) \pm 0.039(\text{syst.}) \pm 0.056(\text{F.S.I.}) \pm 0.017(\text{LEP}) \text{ GeV}/c^2 ,$$

which has slightly higher precision than the current ALEPH result due to an improved pairing algorithm and better estimate of the systematic error due to fragmentation.

The official ALEPH result from the hadronic channel has been combined with ALEPH measurements from the other W^+W^- decay channels at all previous LEP2 centre of mass energies, which in turn have been combined with the other LEP experiments to give the current preliminary LEP W mass average,

$$M_W = 80.350 \pm 0.056 \text{ GeV}/c^2 .$$

This, combined with the results from hadron colliders gives the current world average W mass value from direct reconstruction. This value is in good agreement with the indirect W mass measurement, confirming that the SM is correct at the one-loop level and, combined with direct measurements of the top quark mass, favours a light SM Higgs.

With the high data luminosity collected by the LEP experiments so far this year (approximately 3000 W^+W^- pairs per experiment at $\sqrt{s} = 192 - 202$ GeV) the statistical error will decrease considerably and by the end of 2000 the foreseen statistical precision on the LEP W mass is $\sim 25 - 30$ MeV/ c^2 . This will take the accuracy to the same level as the indirect measurement, thereby testing the SM to its limit. The most important issues between now and then are therefore the understanding of the systematic errors on the measurement, in particular those due to colour reconnection and Bose Einstein correlations in the hadronic channel. With a view towards this goal, the four LEP experiments are beginning to collaborate [113] to produce the world's most precise measurement of the W mass.

Appendix A

Global event shape variables

The final state from $W^+W^- \rightarrow q\bar{q}q\bar{q}$ events consists of many particles of various energy and momentum which describe a four-jet structure. Global variables allow this information to be condensed into simple measures which provide a global view of the event properties. These are often simply dimensionless numbers, which are powerful tools with which to discriminate signal from background. Two such global variables, *Thrust* and *Sphericity*, are described below.

Thrust

The quantity *Thrust* (T) is defined as the sum of the lengths of the longitudinal momenta of the final state particles relative to the axis \mathbf{n} which maximises this sum:

$$T = \frac{\sum_{i=1}^{n_{final}} |\mathbf{n} \cdot \mathbf{p}_i|}{\sum_{i=1}^{n_{final}} |\mathbf{p}_i|},$$

where n_{final} is the number of final state particles. T is in the range $[\frac{1}{2}, 1]$ with $T \sim 1$ for a di-jet event and $T \sim \frac{1}{2}$ for an isotropic event. A related quantity is *Oblateness*, which is defined as the difference between the major and minor axes of the plane perpendicular to the thrust axis.

Sphericity

The sphericity tensor ($S^{\alpha\beta}$) is defined as

$$S^{\alpha\beta} = \frac{\sum_{i=1}^{n_{final}} p_i^\alpha p_i^\beta}{\sum_{i=1}^{n_{final}} |\mathbf{p}_i|^2},$$

where $\alpha, \beta = 1, 2, 3$ correspond to the x, y, z components of the momentum, respectively. The *sphericity* S is defined as

$$S = \frac{3}{2}(\lambda_2 + \lambda_3),$$

where $\lambda_{\alpha,\beta}$ are the eigenvalues obtained from diagonalising the sphericity tensor. S is therefore in the range $[0,1]$, where $S \sim 0$ corresponds to a di-jet event and $S \sim 1$ an isotropic event. A related quantity is *Aplanarity*, which is defined as $A = \frac{3}{2}\lambda_3$.

Appendix B

4C Fit + Rescaling

Consider di-jet invariant masses m_{12} and m_{34} built from a 4 jet event which has undergone a 4C kinematic fit. With a view to obtaining some observable from which to estimate the W mass, define the corresponding *rescaled* masses in terms of the LEP beam energy, E_b , as follows:

$$m_{12}^R = E_b \frac{m_{12}}{E_{12}} \quad m_{34}^R = E_b \frac{m_{34}}{E_{34}}, \quad (\text{B.1})$$

where the di-jet energies,

$$E_{12} = E_1 + E_2, \quad E_{34} = E_3 + E_4, \quad (\text{B.2})$$

and assume in the beginning that there are no experimental errors in the invariant mass reconstruction so that $m_{12} = m_{12}^{true}$, $E_{12} = E_{12}^{true}$ and $\vec{p}_{12} = \vec{p}_{12}^{true}$.

Consider two-body kinematics, then

$$E_{12} + E_{34} = 2E_b \quad (\text{B.3})$$

and since $\vec{p}_{12} = -\vec{p}_{34}$, it follows that $\vec{p}_{12}^2 = \vec{p}_{34}^2$, thus

$$m_{12}^2 - m_{34}^2 = (E_{12} + E_{34})(E_{12} - E_{34}). \quad (\text{B.4})$$

Using B.3 and B.4,

$$E_{12} = E_b + \frac{m_{12}^2 - m_{34}^2}{4E_b}. \quad (\text{B.5})$$

and substituting B.5 into B.1 gives an expression for the rescaled mass:

$$m_{12}^R = m_{12} \left(1 - \frac{m_{12}^2 - m_{34}^2}{4E_b E_{12}} \right), \quad (\text{B.6})$$

thus even without considering experimental errors the rescaled mass is a function both m_{12} and m_{34} .

Now introduce experimental error by considering the case where one particle has been assigned to jet 1 when it should belong to jet 4:

$$E_1 = E_1^{true} + \delta \quad E_4 = E_4^{true} - \delta \quad (\text{B.7})$$

$$\vec{p}_1 = \vec{p}_1^{true} + \vec{\delta} \quad \vec{p}_4 = \vec{p}_4^{true} - \vec{\delta} \quad (\text{B.8})$$

Again assume all measured E and \vec{p} are the true values, giving

$$m_{12}^2 = (E_{12} + \delta)^2 - (\vec{p}_{12} + \vec{\delta})^2 \quad (\text{B.9})$$

$$= E_{12}^2 + \delta^2 - \vec{p}_{12}^2 - |\vec{\delta}|^2 + 2E_{12}\delta - 2\vec{p}_{12} \cdot \vec{\delta} \quad (\text{B.10})$$

$$\simeq (m_{12}^{true})^2 + 2\delta E_{12}, \quad (\text{B.11})$$

since $\vec{p}_{12} \ll E_{12}$ close to threshold. Following a similar argument for the di-jet energy, assuming $\delta^2 \sim 0$,

$$E_{12}^2 \simeq (E_{12}^{true})^2 + 2\delta E_{12}^{true} \quad (\text{B.12})$$

and the ratio of the di-jet mass and energy can then be written:

$$\frac{m_{12}^2}{E_{12}^2} \simeq \frac{(m_{12}^{true})^2 \left(1 + 2\delta \frac{E_{12}}{m_{12}^2}\right)}{(E_{12}^{true})^2 \left(1 + 2\delta \frac{E_{12}}{E_{12}^2}\right)}, \quad (\text{B.13})$$

with the approximation $E_{12} \simeq E_{12}^{true}$ to zero order in δ . Rewriting B.13 in terms of a single argument in δ ,

$$\left(\frac{m_{12}}{E_{12}}\right)^2 \simeq \left(\frac{m_{12}^{true}}{E_{12}^{true}}\right)^2 \left(1 + 2\delta E_{12} \frac{E_{12}^2 - m_{12}^2}{E_{12}^2 m_{12}^2}\right), \quad (\text{B.14})$$

and so the ratio is approximately given by

$$\left(\frac{m_{12}}{E_{12}}\right) \simeq \left(\frac{m_{12}}{E_{12}}\right)^{true} \left(1 + \frac{\delta}{E_{12}} \cdot \frac{p_{12}^2}{m_{12}^2}\right). \quad (\text{B.15})$$

Writing this in terms of the boost of the W in the lab frame, $\beta_W = p/E$ and $\gamma = E/m = (1 - \beta_W^2)^{-\frac{1}{2}}$, B.15 becomes:

$$\left(\frac{m_{12}}{E_{12}}\right) \simeq \left(\frac{m_{12}}{E_{12}}\right)^{true} \left(1 + \frac{\delta}{E_{12}} \cdot (\gamma\beta_W)^2\right), \quad (\text{B.16})$$

so the relative error on $\frac{m_{12}}{E_{12}}$ is suppressed by the factor $(\gamma\beta_W)^2$. Near threshold this is approximately $\propto \beta_W^2$, while at $\sqrt{s} = 189$ GeV it is $\sim \beta_W$.

Substituting B.16 into B.1, the rescaled mass when experimental errors are introduced becomes:

$$m_{12}^R \simeq m_{12}^{true} \left(1 - \frac{(m_{12}^{true})^2 - (m_{34}^{true})^2}{4E_b E_{12}^{true}} \right) \left(1 + \frac{\delta}{E_{12}} \cdot (\gamma\beta_W)^2 \right) \quad (\text{B.17})$$

$$\simeq (m_{12}^R)^{true} \left(1 + \frac{\delta}{E_{12}} \cdot (\gamma\beta_W)^2 \right). \quad (\text{B.18})$$

To compare the effect of the experimental error on the 4C masses, rewrite B.9 as

$$m_{12} \simeq m_{12}^{true} \left(1 + \frac{\delta}{m_{12}} \gamma \right), \quad (\text{B.19})$$

so there is a reduction in experimental errors of $1/\gamma\beta_W^2 \sim 3$ when using the rescaled masses.

In summary, the rescaled masses m_{12}^R and m_{34}^R are not in themselves better estimators of m_{12}^{true} and m_{34}^{true} . For the case of $m_{12} = m_{34}$ (on-shell W's), rescaling significantly improves the di-jet mass resolution because the effects of measuring the wrong W are reduced. However, for the case of the Breit Wigner decay of W's it is not the case that $m_{12} = m_{34}$, but rescaling still adds more information through the W^+ and W^- velocities which results in a reduction in experimental errors.

References

- [1] The UA1 Collaboration, Phys. Lett. **B122** (1983) 103.
 - [2] The UA2 Collaboration, Phys. Lett. **B122** (1983) 476.
 - [3] The LEP Collaborations ALEPH, DELPHI, L3, OPAL, the LEP Electroweak Working Group and the SLD Heavy Flavour and Electroweak Groups, "A Combination of Preliminary Electroweak Measurements and Constraints on the Standard Model", Prepared from Contributions of the LEP and SLD experiments to the 1998 Summer conferences. CERN-EP/99-15.
 - [4] The LEP Collaborations ALEPH, DELPHI, L3, OPAL, the LEP Electroweak Working Group and the SLD Heavy Flavour and Electroweak Groups, "A Combination of Preliminary Electroweak Measurements and Constraints on the Standard Model", Prepared from Contributions of the LEP and SLD experiments to the 1999 Summer conferences. Publication in Progress.
 - [5] The CDF Collaboration, Phys. Rev. **D52** (1995) 4784.
 - [6] The D0 Collaboration, Phys. Rev. **D58** (1998) 092003.
 - [7] The UA2 Collaboration, Phys. Lett. **B276** (1992) 354.
 - [8] M. Lancaster, "New W mass Results from CDF/D0", Talk at Moriond, March 19th 1999.
 - [9] The CDF Collaboration, Phys. Rev. Lett. **75** (1995) 11.
 - [10] The ALEPH Collaboration, "Measurement of the W mass from $W \rightarrow \ell\nu$ decays at 183 GeV", ALEPH 99-015, CONF 99-010.
 - [11] Z. Kunst and W.J. Stirling, "Determination of the mass of the W boson" In Physics at LEP2, G. Altarelli, T. Sjöstrand and F. Zwirner (editors), CERN 96-01 (1996), vol. 1, 162.
-

-
- [12] A. Butterworth (SL Division), Presentation to LEPC, November 9th 1999.
- [13] F. Halzen and A. D. Martin, "Quarks and Leptons", New York: Wiley, 1984.
- [14] J. P. Elliot and P. G. Dawber, "Symmetry in Physics", The MacMillan Press Ltd., 1979.
- [15] D. Griffiths, "Introduction to Elementary Particles", John Wiley and Sons, Inc., Canada 1987.
- [16] I. J. R. Aitchison and A. J. G. Hey, "Gauge Theories in Particle Physics", Adam Hilger, 2nd Edition 1989.
- [17] T. Ferbel, "Techniques and Concepts of High Energy Physics", NATO Science series, Series C: Mathematical and Physical Sciences- Vol. 534.
- [18] P. Renton, "Electroweak Interactions", Cambridge University Press 1990.
- [19] R. P. Feynman, "QED: The Strange Theory of Light and Matter", Princeton University Press 1985.
- [20] G. 't Hooft, Nucl. Phys. **B33** (1971), 173.
- [21] E. Fermi, Z. Phys. **88** (1934) 161.
- [22] Wu *et. al.*, Phys. Rev. **105** (1957) 1413.
- [23] S. L. Glashow, Nucl. Phys. **22** (1961) 579.
- [24] S. Weinberg, Phys. Rev. Lett. **19** (1967) 1264.
- [25] A. Salam, in: "Elementary Particle Theory", ed. N. Svartholm, Stockholm (1968), p 367.
- [26] P. W. Higgs, Phys. Rev. Lett. **13** (1964) 508; Phys. Rev. Lett. **12** (1964) 132.
- [27] V. A. Khoze and W. J. Stirling, Phys. Lett. **B356** (1995) 373.
- [28] W. Beenakker and F. A. Berends, "WW cross-sections and distributions", In Physics at LEP2, G. Altarelli, T. Sjöstrand and F. Zwirner (editors), CERN 96-01 (1996), vol. 1, pp. 79.
- [29] W. Beenakker and A. Denner, Int. J. Mod. Phys. **A9** (1994) 4837.
- [30] A. Denner, Fortschr. Phys. **41** (1993) 307.
-

-
- [31] C. Caso *et. al.* (Particle Data Group), Eur. Phys. J. **C3** 1 (1998) and 1999 partial update for edition 2000 (<http://www-pdg.lbl.gov/>).
- [32] T. Muta, R. Najima and S. Wakaizumi, "Effects of the W-Boson Width in $e^+e^- \rightarrow W^+W^-$ Reactions" Mod. Phys. Lett. **A**, Vol. 1, No.3 (1996) 203-210.
- [33] D. Bardin, A. Leike, T. Riemann and M. Sachwitz, "Energy Dependent Width effects in e^+e^- annihilation near the Z pole", Phys. Lett. **B206** (1998) 539.
- [34] B. Andersson, G. Gustafson, G. Ingleman and T. Sjöstrand, Phys. Rep. **97** (1983) 31.
- [35] T. Sjöstrand, Comp. Phys. Commun. **82** (1994) 74.
- [36] G. Marchesini, Comp. Phys. Commun. **67** (1992) 465.
- [37] T. Sjöstrand and V. A. Khoze, "On Colour Rearrangement in hadronic W^+W^- events", Z. Phys. **C62** (1994) 281.
- [38] L. Lönnblad and T. Sjöstrand, "Bose-Einstein effects and W mass determinations", Phys. Lett. **B351** (1995) 293.
- [39] G. Goldhaber, S. Goldhaber, W. Lee and A. Pais, "Influence of Bose-Einstein Statistics on the Antiproton-Proton Annihilation Process", Phys. Rev. **120** (1960) 300.
- [40] L. Lönnblad and T. Sjöstrand, Eur. Phys. J. **C2** (1998) 165.
- [41] D. Buskulic *et. al.* (The ALEPH Collaboration), "Performance of the ALEPH detector at LEP", Nucl. Inst and Meth. **A360** (1995) 481.
- [42] The DELPHI Collaboration, Nucl. Inst. and Meth. **A303** (1991) 233.
- [43] The OPAL Collaboration, Nucl. Inst. and Meth. **A305** (1991) 275.
- [44] The L3 Collaboration, Nucl. Inst. and Meth. **A289** (1990) 33.
- [45] S. Myers and E. Picasso, "The design, construction and commissioning of the CERN Large Electron Positron collider", Contemp. Phys. **31** (1990) 387.
- [46] LEP Energy Working Group, "Calibration of center-of-mass energies at LEP1 for precise measurements of Z properties", CERN-EP/98-040, CERN-SL/98-012.
-

-
- [47] The LEP Energy Working Group, "Evaluation of the LEP centre-of-mass energy for data taken in 1998", LEP Energy Working Group 99-01.
- [48] The LEP Spectrometer Working Group "The LEP Spectrometer Project", Report in Progress, 1999.
- [49] The ALEPH Collaboration, "The ALEPH handbook 1995 Vol. 1", European Organisation for Nuclear Research, CERN, Geneva 1995.
- [50] The ALEPH Collaboration, "The ALEPH handbook 1995 Vol. 2", European Organisation for Nuclear Research, CERN, Geneva 1995.
- [51] D. Creaanza *et al.* (The ALEPH Collaboration), "Construction and Performance of the new ALEPH Vertex Detector", In Proceedings of the 5th International Conference on Advanced Technology and Particle Physics, Como, Italy, 7-11 October 1996.
- [52] G. J. Barber *et al.* (The ALEPH Collaboration), "Performance of the three dimensional readout of the ALEPH Inner Tracking Detector", Nucl. Inst and Meth. **A279** (1989) 212.
- [53] W. B. Atwood *et al.* (ALEPH Collaboration), "Performance of the ALEPH Time Projection Chamber", Nucl. Inst and Meth. **A306** (1991) 446.
- [54] M. Schmelling, B. Wolf, "Laser Calibration of the ALEPH -TPC" ALEPH 91-150, TPCGEN 91-004.
- [55] R. Fernow, "Introduction to Experimental Physics", Cambridge University Press. pp 270.
- [56] J. Knobloch, "JULIA Users and Programmers guide", ALEPH 90-11 (1990).
- [57] H. Albrecht, E. Blucher and J. Boucrot, "ALPHA ALEPH Physics Analysis Package", ALEPH 97-058 (1997).
- [58] <http://alephwww.cern.ch/ALEPHGENERAL/kin/>.
- [59] <http://wwwinfo.cern.ch/asd/geant/index.html>.
- [60] <http://alephwww.cern.ch/LIGHT/galeph.html>.
- [61] M. Skrzypek, S. Jadach, W. Placzek and Z. Was, "Monte Carlo program KORALW 1.02 for W-pair production at LEP2/NLC energies with Yennie-Frautschi-Suura exponentiation", Comp. Phys. Commun. **94** (1996) 216.
-

-
- [62] T. Sjöstrand, "PYTHIA 5.7 and JETSET 7.4 Physics and Manual", CERN-TH.7112/93.
- [63] E. Accomando *et. al.*, "Event Generators for LEP2 Physics" In "Physics at LEP2", G. Altarelli, T. Sjöstrand and F. Zwirner (editors), CERN 96-01 (1996), vol. 1, 59.
- [64] S. Jadach, B.F.L. Ward, Z. Was, "The Monte Carlo program KORALZ version 4.0 for the lepton or quark pair production at LEP/SLC energies", Comp. Phys. Commun. **79** (1994) 503, (CERN-TH-7075 preprint, 1993).
- [65] A. S. Thompson *et. al.* "A measurement of the hadronic WW cross section at 161 GeV by a weighting method", ALEPH 96-118, PHYSIC 96-109.
- [66] F. Machefert, "A selection algorithm for fully hadronic WW decay using density probability distributions", ALEPH 97-090, PHYSIC 97-080.
- [67] C. Guicheney, J. Jousset, F. Podlyski and J. M. Rossignol, "WW Cross Section Measurement at 172 GeV using a Neural Network", ALEPH 97-053, PHYSIC 97-047.
- [68] The ALEPH Collaboration, "Measurement of the W mass by direct reconstruction in e^+e^- collisions at 172 GeV", Phys. Lett. **B 422** (1998) 384.
- [69] M. Chalmers, "Measuring the W mass using 2 Dimensional Monte Carlo Reweighting", Second Year Report, University of Glasgow 1998.
- [70] The ALEPH Collaboration, "Measurement of the W mass in e^+e^- collisions at 183 GeV", Phys. Lett. **B 453** (1999) 121.
- [71] <http://www-wisconsin.cern.ch/jins/ww4q.html>.
- [72] G. Cowan, "Statistical Data Analysis", Oxford University Press 1998.
- [73] A. Trabelsi, "Mesure de la masse du boson W^\pm dans l'expérience ALEPH du LEP", Ph.D. Thesis Université de la Méditerranée, Marseille (1997).
- [74] J. M. Scarr and I. ten Have, "PTCLUS: Jet Finding Algorithm for High Energy Hadronic Final States", ALEPH 89-150, PHYSIC 89-60.
- [75] T. Sjöstrand *et. al.*, Comp. Phys. Comm. **28** (1983) 227.
-

-
- [76] R. J. Cavanaugh, "An ALPHA Tool for Constrained Kinematic Fits to W^+W^- events: QFITWW", ALEPH 96-129 PHYSIC 96-118.
- [77] F. Machefert, "Mesure de la masse du boson W par la methode de reconstruction directe dans l'experience ALEPH au LEP", Ph.D. Thesis (1998) pp. 98.
- [78] A. Blondel, Private Communication, June 1999.
- [79] The ALEPH Collaboration, "Measurement of the W Mass in e^+e^- Collisions from 161 to 189 GeV", ALEPH 99-017 / CONF 99-012 (1999).
- [80] A. Moutoussi, Presentation to the ALEPH WW Group, CERN, June 1999.
- [81] The ALEPH Collaboration, "Measurement of the W Mass and Width in e^+e^- Collisions at 189 GeV", to be published.
- [82] S. Goodsir, "A W Mass measurement with the ALEPH Detector", Ph.D. Thesis, Imperial College of Science, Technology and Medicine (1999).
- [83] A. Juste, "A Measurement of the W mass in e^+e^- annihilation", Ph.D. Thesis, Universitat Autònoma de Barcelona, May 19th 1998.
- [84] G. Boix, S. Bravo, E. Grauges, A. Juste, M. Martinez, G. Merino, Ll. M. Mir, I. Riu and F. Teubert, "W mass measurement in the four jet channel using a MC reweighting technique", ALEPH 97-067, PHYSIC 97-060.
- [85] I. Rui, "Measurement of the W mass from the $W^+W^- \rightarrow q\bar{q}q\bar{q}$ channel with the ALEPH Detector", Ph.D. thesis Universitat Autònoma de Barcelona (1998).
- [86] L. Amendola, "Non-Gaussian Likelihood Function", FERMILAB-Pub-94/263-A.
- [87] D. Bardin, J. Biebel, D. Lehner, A. Leike, A. Olchevski and T. Riemann, "GENTLE/4fan v2.0, a program for the semi-analytic calculation of predictions for the process $e^+e^- \rightarrow 4f$ ", Comput. Phys. Commun. **104** (1997) 161.
- [88] F. James, "MINUIT: Function Minimisation and Error Analysis", CERN Program Library Long Writeup D506 (1994).
- [89] The ALEPH Collaboration, "Measurement of the W mass by direct reconstruction in e^+e^- collisions at 181-184 GeV", ALEPH 98-020, CONF 98-010.
- [90] R. Clift, Presentation to ALEPH WW group, Barcelona 1998.
-

-
- [91] The ALEPH Collaboration, "Studies of Quantum Chromodynamics with the ALEPH detector, CERN-PPE/96-186, Phys. Rep. **294** (1998) 1.
- [92] <http://alephwww.cern.ch/ligabue/syst/syst.html>.
- [93] I. Rui, "W Mass Background Systematic Study using Z peak data" ALEPH 97-060 PHYSIC 97-053.
- [94] L. Lönnblad, Comp. Phys. Commun. **71** (1992) 15.
- [95] P. Ghez, "Determination of M_W (4q) using a NN-based fitting technique", ALEPH 99/096, PHYSICS 99/042 1999.
- [96] M. Kendall and A. Stuart, "The Advanced Theory of Statistics", Charles Griffin and Co. (1967) vol.2, 452.
- [97] W. H. Press *et. al.*, "Numerical Recipes in Fortran", (1992) Second Edition, 617.
- [98] J. A. Peacock, "Two-dimensional goodness-of-fit tests in astronomy", Mon. Not. R. Astr. Soc. **202** (1983), 615.
- [99] G. Fasano and A. Francechini, "A multidimensional version of the Kolmogorov-Smirnov test", Mon. Not. R. Astr. Soc. **225** (1987), 155.
- [100] F. James (PDG), Private communication, March 1999.
- [101] A. Frodesen and O. Skjeggstad, "Probability and Statistics in Particle Physics", (1979) pp. 424-427.
- [102] T. Anderson and D. Darling, "Annals of Mathematical Statistics", (1952) vol.23, pp. 193-212.
- [103] W. Eadie, D. Dryard, F. James, M. Roos and B. Sadoulet, "Statistical Methods in Experimental Physics", (1971), pp. 269-271.
- [104] The ALEPH Collaboration, "Measurement of the W mass in e^+e^- Collisions at Production Threshold", Phys. Lett. **B** (1997).
- [105] The OPAL Collaboration, "Measurement of the W mass and width in e^+e^- collisions at 183 GeV", Phys. Lett. **B453** (1999) 138.
- [106] The L3 Collaboration, "Measurement of mass and width of the W boson at LEP", Phys. Lett. **B454** (1999) 386.
-

- [107] The DELPHI Collaboration, "Measurement of the mass of the W boson using direct reconstruction at $\sqrt{s} = 183$ GeV ", Phys. Lett. **B462** (1999) 410.
- [108] The LEP WW Working Group, "LEP WW cross-section and W mass (up to 189 GeV for '99 summer conferences)", LEPEWWG/WW/99-02 1999.
- [109] J. Mnich, "Tests of the Standard Model", International Europhysics Conference on High Energy Physics, Tampere, Finland, 20th July 1999.
- [110] R. Madaras, "W boson physics at the Fermilab Tevatron collider", In Proceedings of the XVIII International Conference on Physics in Collision, June 1998, Frascati, Italy HEP-EX/9808021.
- [111] K. McFarland *et. al.*, CCFR Collaboration, Eur. Phys. J. **C1** (1998) 509.
- [112] G. Zellar, "A Measurement of $\sin^2\theta_W$ in νN Scattering from NuTeV" Proceedings of the Division of Particles and Fields Conference, UCLA, January 6th 1999.
- [113] <http://www.cern.ch/LEPEWWG/crete99/>.

